Electrocatalytic Activity of Ni Hydroxides with Zn or Co in the Ni Matrix

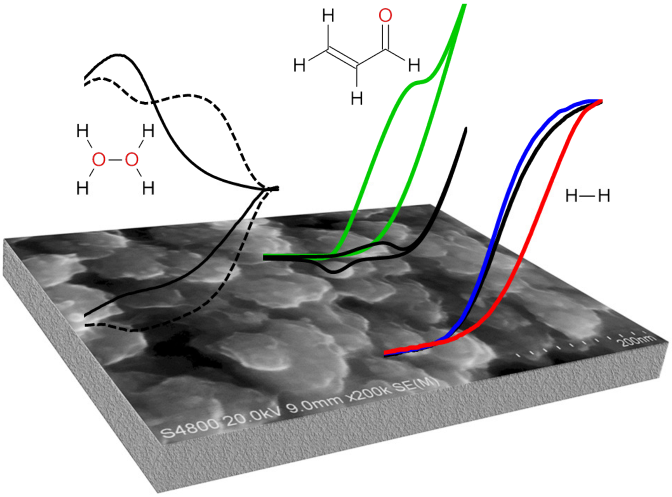

Gert Göransson

Ph.D. thesis
Department of Chemistry and Molecular Biology
University of Gothenburg

UNIVERSITY OF GOTHENBURG

Faculty of Science

THESIS FOR THE DEGREE OF DOCTOR OF PHILOSOPHY IN CHEMISTRY

Electrocatalytic properties of Ni hydroxides with Zn or Co in the Ni matrix

Gert Göransson

UNIVERSITY OF GOTHENBURG

Department of Chemistry and Molecular Biology
University of Gothenburg
Gothenburg, Sweden
2014

Electrocatalytic properties of Ni hydroxides with Zn or Co in the Ni matrix

Department of Chemistry and Molecular Biology

University of Gothenburg

412 95 Göteborg

ISBN 978-91-628-8897-8

E-publications: http://hdl.handle.net/2077/34697

Printed by Chalmers Reproservice

Cover Illustration:

SEM image of pulse plated NiZn (J. Heyrovsky Institute of Physical Chemistry, 2008) with cyclic voltammetry curves and product molecules from oxygen reduction, propenol oxidation and proton reduction, the essential reactions treated in this thesis.

Abstract

The majority of the work in this thesis has been made with the improvement of the systems for electrochemical co-generation of chemicals and electricity in mind. This is an appealing but challenging way of producing chemicals with energy as a bi-product, and is commonly referred to as “green chemistry”. In this study electrocatalytic reactions have been investigated on electrodes for which Ni is the main active species with minor addition of Zn and Co in the Ni matrix. Three important reactions have been investigated; the oxygen reduction reaction (ORR) and propenol oxidation in alkaline solution, and the proton reduction reaction (PRR) at pH 2.8. The main focus has been on the improvement of Ni based catalysts for O_2 reduction to H_2O_2 in alkaline solution. Ni has the advantage to forms a very stable oxide/hydroxide under alkaline conditions and Zn and Co are under certain conditions known to promote a $2e^-$ reduction of O_2.

A novel type of Ni-rich NiZn alloys were produced by pulse plating under anomalous deposition of Ni and Zn in a sulphate electrolyte at pH 2.8. The alloys were seen to grow in isolated 3D clusters with substantial height before the surface became completely covered. EDX measurements showed a Ni-rich alloy of Ni_xZn_{1-x} where x is between 0.14 and 0.21 depending on plating conditions. The long range order of these alloys was not possible to determine and the short range order was therefore investigated by XAFS. The result showed that the alloy was organised as a multiphase system consisting of *hcp*- and *ccp*-like structural moieties with non-homogeneous distribution of Zn, rather than the expected solid solution. The correlation of the catalytic activity between structure and proton reduction for the NiZn alloy was not unambiguous, but the reaction rate was however clearly enhanced compared to solid Ni.

The catalytic activity towards oxygen reduction in alkaline environment was studied on pulse plated Ni and NiZn. Alloying Ni with Zn clearly favoured the reaction path towards H_2O_2 and also lowered the overpotential for the reaction, even though the limiting currents indicated recessed electrode behaviour.

Direct electrochemical oxidation of propen and propenol on the pulse plated Ni and NiZn electrode was investigated in alkaline solution by CV and DEMS. The direct oxidation of propen has been reported in the literature but could not be repeated. The oxidation of propenol overlapped with oxidation of the substrate and oxygen evolution in a complex manner, with propenal as the main product. It was shown that water oxidation starts when half of the $Ni(OH)_2$ sites were oxidised to NiOOH which indicates a bi-nuclear water oxidation mechanism. A $Ni(OH)_2$/NiOOH mediated reaction mechanism was proposed in analogy with previous studies for other alcohols and amines.

To investigate the importance of the underlying Ni metal NiO was synthesised and made to an electrode by mixing it with carbon paste (CP). $Ni_{0.75}Co_{0.25}O$ and CoO were also synthesised for comparison with NiO in the reactivity towards the ORR. 67 wt% NiO in CP increased the rate constant by 25 times compared to pure CP and showed the highest overall efficiency for ORR, for which the reduction to H_2O_2 prevails.

Keywords: Redox mediated electron transfer, electrodeposition, pulse plating, Ni-rich alloy, NiZn, NiO, CoO, carbon paste electrodes, cyclic voltammetry, RRDE, DEMS, XAFS

List of publications

This thesis is based on the work presented in the following paper. The papers will be referred to as Paper I-IV in the thesis.

Paper I:	Characterisation of pulse plated Ni and NiZn alloys Gert Göransson, Annika Johansson, Fredrik Falkenberg and Elisabet Ahlberg *Submitted paper*
Paper II:	Local structure of pulse plated Ni rich Ni-Zn alloys and its effect on the electrocatalytic activity in the hydrogen evolution reaction G. Göransson, M. Peter, J. Franc, V. Petrykin, E. Ahlberg and P. Krtil *J. Electrochem. Soc. 159(9) (2012) D555*
Paper III:	Oxidation of propenol on nanostructured Ni and NiZn electrodes in alkaline solution Gert Göransson, Jakub S. Jirkovský, Petr Krtil and Elisabet Ahlberg *Submitted paper*
Paper IV:	Oxygen reduction in alkaline solution using mixed carbon paste/ $Ni_xCo_{1-x}O$ electrodes Gert Göransson and Elisabet Ahlberg *Submitted paper*

Contribution list

Paper I:	Performed and analysed the electrochemical measurements together with A. Johansson. Lead author with support from co-authors.
Paper II:	Performed all electrochemical experiments. Took part in the XAFS experiments. Contributed to data evaluation and writing.
Paper III:	Performed all electrochemical measurements and took part in the DEMS measurement. Major contributor to data analysis and writing.
Paper IV:	Performed and analysed the electrochemical measurements. Lead author with support from co-author.

Table of Contents

List of abbreviations

A	area	cm
C	concentration	molcm^{-3}
D	diffusion coefficient	cm^{2}s^{-1}
E^o	standard potential	V
$E^{o'}$	formal potential	V
E_p	peak potential	V
k^0	standard heterogeneous rate constant (at E^o)	cms^{-1}
i	current	A
i_d	disc current	A
i_F	Faradic current	A
i_{pa}	anodic peak current	A
i_{pc}	cathodic peak current	A
i_{pp}	pulse plating current	A
i_k	kinetically controlled current	A
i_r	ring current	A
i_l	limiting current (by diffusion)	A
i_c	cathodic current	A
i_a	anodic current	A
i_m	average pulse current	A
j	current density	Acm^{-2}
j_0	exchange current density	Acm^{-2}
j_{ppl}	limiting pulse current density	Acm^{-2}
N	collection efficiency	none
M	molar mass	gmol^{-1}
m	mass-transfer coefficient	cms^{-1}
Q	charge	C
r	radius	cm
t_{on}	time for pulse current on	s
t_{off}	time for pulse current off	s
Γ	surface excess of species	molcm^{-2}
α	transfer coefficient	none
ν	kinematic viscosity	cm^{2}s^{-1}
ω	angular frequency of rotation	rads^{-1}
δ	diffusion layer thickness	cm
γ	duty cycle	none
τ	transition time	s
ρ	density	gcm^{-3}
F	Faradays constant	Cmol^{-1}
R	molar gas constant	Jmol^{-1}K^{-1}

AFM	Atomic force microscopy
CA	Chronoamperometry
ccp	cubic close packing
CE	Counter Electrode
CP	Carbon Paste
CV	Cyclic Voltammetry
DC	Direct Current
DEMS	Differential Electrochemical Mass Spectrometry
DSA	Dimensional Stable Anodes
EDX	Energy-Dispersive X-Ray Spectroscopy
EQCM	Electrochemical Quartz Crystal Microbalance
fcc	face centered cubic
GC	Glassy Carbon
hcp	hexagonal close packing
HER	Hydrogen Evolution Reaction
IRET	Irreversible Electron Transfer Reaction
K-L	Koutecký-Levich
OCP	Open Circuit Potential
OER	Oxygen Evolution Reaction
ORR	Oxygen Reduction Reaction
PEMFC	Proton Exchange Membrane Fuel Cell
PRR	Proton Reduction Reaction
PRP	Pulse Reverse Plating
QRET	Quasi-Reversible Electron Transfer
RE	Reference Electrode
RET	Reversible Electron Transfer
RDE	Rotating Disc Electrode
RRDE	Rotating Ring Disc Electrode
SCE	Saturated Calomel Electrode
SEM	Scanning Electron Microscopy
SHE	Standard Hydrogen Electrode
SOFC	Solid Oxide Fuel Cell
UPD	Under Potential Deposition
WE	Working Electrode
XAFS	x-ray Absorption Fine Structure

1 Introduction

The importance of catalysis in chemistry cannot be overestimated and much of our effort as scientists in chemistry deals with the control of the energy barrier for chemical reactions. Energy barriers can be lowered so that the rate of a reaction increases, but also a controlled increase of an energy barrier can in some instances be preferable for instance in a second electron transfer step in which a reaction can be terminated at an intermediate state to give a desired product. A delicate way of lowering the energy barrier for a reaction is by the use of a specific catalyst, which can be defined as an atom, ion or molecule in solution or at a surface (a heterogeneous system). In the latter case the atom, the molecule or the ion participates in a reaction but it is not consumed. By the use of catalysts, energy consuming chemical conversion procedures with high temperature and high pressure can be avoided.

In this study heterogeneous electrocatalytic reactions have been investigated and this brief introduction to the subject will subsequently be restricted to that type of catalysis. Heterogeneous electrocatalysis involves the surface of the electrode metal, its oxide or eventually an adsorbed specie, which can conduct electrons from the bulk of the electrode to an incoming specie. This specie has to interact to some extent with the electrode surface in order for an electron to pass. For a reaction to be electrocatalytic the interaction must result in some form of chemical bond and it is the strength of this bond that largely determines the catalytic property of the reaction. When a reactant has formed a bond to the surface atoms it can continue to react either chemically or electrochemically in one or several steps before it is released (desorbed) from the surface. If a strong bond is formed in the primary adsorption step this step will initially be fast, but a strong bond will most likely not be broken in the reformation or desorption step. If the electrode surface is not cleared fast enough the reaction rate of the incoming reactant will decrease. This implies that it should exist some kind of ideal bond strength specific for each reaction. The suggestion that an ideal catalyst is governed by the ideal bond with the reactant was presented long time ago by Sabatier and its implications are preferably shown as "volcano plots". These plots have been constructed for several important electrocatalytic reactions of which the first ones were based on the exchange current of the reaction versus the measured binding energies (M-H) of a number of metals [1].Today the corresponding volcano plots of more complex electrodes are also investigated by computational methods since the traditional materials have proven insufficient for many important applications [2].

The development of electrocatalytic material is important in many aspects and has often positive effects on the environment in a direct manner such as cleaning of toxic waste or indirectly by lowering the energy consumption of large industrial processes. One of the greatest discussions of our time deals with the question if (or rather to what extent), how and when a change of the global energy system is necessary and how such a change would look like. The concept "hydrogen economy" was launched many years ago as an alternative to the ruling concept "fossil economy" and a lot of effort have been undertaken to solve the fundamental issues of having hydrogen gas (H_2) as the main energy carrier. The prime reactions in such systems are the oxidation of hydrogen (in fuel cells) and the connected reduction of oxygen (e.g. in fuel cells and metal-air batteries). In addition, there is also the intricate question of production of H_2, which in a hydrogen economy must be based on water, and in addition electrochemical splitting of water by e.g. solar cells. It is worth mentioning that good electrocatalytic properties on both the anode side and the cathode side are crucial for the whole concept.

As a side-track, and closely related to the processes involved in the hydrogen economy, is the increasing interest for hydrogen peroxide. Hydrogen peroxide is generated by the reduction of oxygen “half way” compared to the process in a conventional fuel cell and is, above all, one of the most environmentally friendly chemical oxidant known.

Electrochemical co-generation of chemicals and electricity is an appealing but challenging way of producing chemicals and this can benefit from the strong efforts made from the improvements of catalyst materials and membranes for the fuel cells [3]. This type of chemical production would indeed be classified as “green chemistry” as the net energy consumption would be lower than in a conventional chemical plant. Even though the research field for co-generation processes in fuel cells increases it is still small and a large breakthrough for this technique must unfortunately be considered to be quite far in the future.

2.1 Aim of the Thesis

The aim of this thesis is to investigate the electrocatalytic activity of oxidised non-precious metals for a few important reactions. The main focus is on the important electrochemical oxygen reduction reaction leading to hydrogen peroxide. Nickel was in that respect chosen as the base metal, since it is a promising candidate for a two electron reduction of O_2 to H_2O_2 with a reasonable high activity to a low cost. Nickel was then combined with low amounts of zinc in a pulse plated NiZn alloy as Zn promotes the reduction to H_2O_2 but is unstable in both acidic and alkaline solutions. Nickel was in addition combined with Co in a $Ni_xCo_{1-x}O$ solid solution to investigate the influence of Co(II) in a matrix with Ni(II) since Co(II) in macrocyclic complexes mainly promotes H_2O_2. Mechanistic proposals involving the redox couple $Ni(OH)_2/NiOOH$ are given for propenol oxidation to propenal as well as for the involvement in oxygen reduction to hydrogen peroxide by using quinones on carbon paste electrodes.

2 | Literature Survey

The main topic of this thesis is focussed on the oxygen reduction reaction preferably to hydrogen peroxide and the oxidation of propen and propenol. Nickel in some form is involved in all papers in this thesis and is one of the most interesting catalysts for all the reactions studied in here as well as for many other very important reactions in our society. Nickel has therefore been analysed in a rather comprehensive detail in this literature survey with respect to oxygen reduction, splitting of water and oxidation of propen and propenol.

2.1 The complex matter of Nickel

2.1.1 History and use of Nickel

The use of nickel goes back more than 2000 years and it was found in China where it was used in alloys, however not in its pure form. Much later in Europe, German miners mistakenly gave the name "Kupfernickel" (from copper - kupfer and the devil in German mythology - Nickel) to the reddish NiAs ore since they believed it was a Cu2S ore from which they could not extract any copper - therefore the ore was believed to be a construction by the devil. It was, however, not until 1751 that A. F. Cronstedt first managed to isolate the metal in the Los-mine in Hälsingland (Sweden) and subsequently gave it the name Nickel [4].

Nickel is the seventh most abundant transition metal in the earth's crust (99 ppm) and the major ores of commercial interest are laterites (oxide/silicate) and sulphides [4]. Today the three largest producers of Nickel are Russia, Canada and New Caledonia. Nickel is used in over 300,000 products from everyday consumer products to highly advanced aerospace components. Eighty four percent of all the 1400 tons of nickel produced annually (new and primary) ends up in some kind of alloy being the minor or the major part. Approximately 9% is used in plating processes and 6% is used in other applications such as coins, electronics and batteries [5]. Nickel based catalysts are also widely used in the chemical industry, from the oil refining industry [6-7] to the food industry and the nickel based catalyst is today the most cost efficient catalyst for methane reforming to produce hydrogen and syngas [5, 8-9]. A major part of its desired catalytic performance is gained by its ability to store large quantities of hydrogen. Nickel plays, in addition, an important role also in the stationary solid oxide fuel cell (SOFC) technology, e.g. in the Ni-YSZ (yttria-stabilized zirconia) composite used as the anode material [5, 10-11]. For the general public, nickel is probably mostly associated with the NiCd and NiMH batteries and the research on the use of nickel around these applications has been extensive for many decades. However, during the last decade many of the NiMH applications have been replaced by lithium batteries and of course the interest in Nickel in this field has then decreased although some of the lithium batteries do still contain nickel. New fields for nickel based materials have been established and one of these fields is solar energy, where nickel oxide is a promising cathode material for dye-sensitive solar cells [12].

As a catalyst nickel has been suggested, applied, abandoned and re-discovered for a wide range of reactions during the last century and in this thesis nickel will again be investigated for its catalytic ability to enhance particular reactions first studied half a century ago but now in a slightly different perspective.

2.1.2 Properties of oxidised Nickel

The majority of the research presented in this thesis is done on oxidised nickel either as bulk NiO or as nickel metal oxidised in an alkaline environment. A quite detailed background of the complex nickel oxide system is given and although some of this material is at the periphery of the focus of this thesis a more complete description is useful for the understanding and discussion of the results. It also serves as the basis for a discussion of future perspectives.

Nickel oxide (NiO) has a face centred cubic (*fcc*) rock salt structure with *p*-type semiconducting properties. The hydrated oxides are generally described as layers of NiO_x with various combinations of water and counter ions in between these layers, which conforms to a more hexagonal cubic (*hcp*) structure. The nickel hydroxide ($Ni(OH)_2$) is naturally formed in an alkaline environment and can be further oxidised to nickel oxyhydroxide (NiOOH). The available standard potentials for the reactions involved are given below.

All standard potentials in this thesis are quoted from the CRC handbook [13] if not otherwise stated. Standard potentials are measured or calculated at 25° C, 1 atm and 1 molar/molal concentration of the species involved in the reaction. The pH in standard conditions are pH 0 when protons are involved, and pH 14 for hydroxide ions and if the standard conditions are changed to a 0.1 M KOH solution the reaction will contribute 0.769 V negative (counted from pH 0) or 0.0591 positive (counted from pH 14) to the E^o value (Nernst Eqn. $E = E^o - 0.0591 \cdot \Delta pH$). The most frequently used reference electrode in this thesis is Ag/AgCl (KCl sat'd), which will measure the potential of a reaction as 0.197 V more negative than the standard hydrogen electrode (SHE) and potentials versus Ag/AgCl (KCl sat'd) will be given in parenthesis.

$$Ni^{2+} + 2e^- \leftrightarrows Ni \qquad E^o = -0.257 \text{ V vs. SHE } (-0.454 \text{ V}) \qquad (2.1)$$

$$\beta\text{-}Ni(OH)_2 + 2e^- \leftrightarrows Ni \qquad E^o = -0.72 \text{ V vs. SHE [14] } (-0.92 \text{ V}) \qquad (2.2)$$

$$\beta\text{-}Ni(OH)_2 + OH^- \leftrightarrows \beta\text{-}NiOOH + e^- + H_2O \qquad E^o = 0.48 \text{ V vs. SHE [14] } (0.28 \text{ V}) \qquad (2.3)$$

A detailed description of the $Ni(OH)_2$/NiOOH redox couple was proposed in a scheme using the square model by Bode et al. already in 1966 [15]. Even though a large amount of information has since then been presented to complete this model, the complexity of the structures interacting with an electrolyte has left some phases incompletely resolved. In an attempt to gather as much of the available information as possible in Bodes original scheme of a square model, an extended scheme is presented in Figure 2.1 where the information have been gathered from a number of papers [16-23]

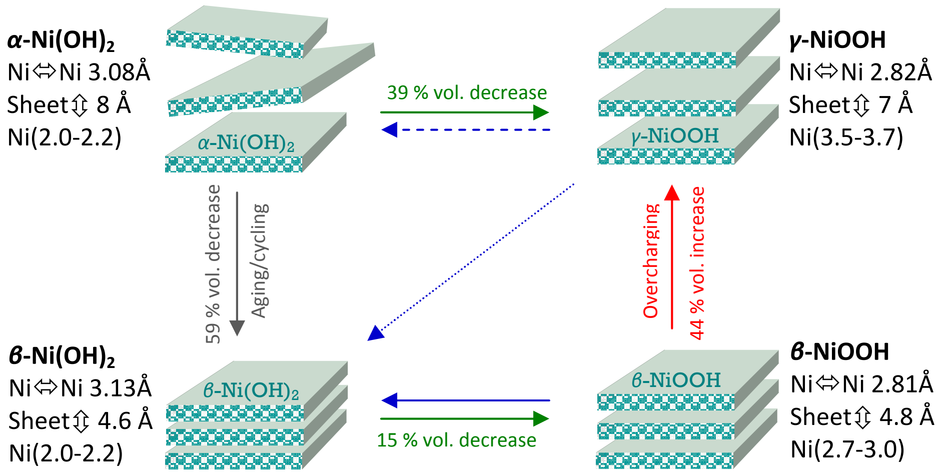

Fig. 2.1 Schematic figure of the redox cycle of nickel hydroxide. Data of bond distance within⇔ the sheets and between⇳ two "NiO_2" sheets. The valance state of the Ni is shown in parentheses.

To present the different phases in Figure 2.1 it is suitable to start with the naturally or chemically precipitated α-$Ni(OH)_2$ [15, 24] in which the oxide layers often are described to have a tilted turbostratic structure with a very large volume. It is important to point out that the structure details of the α- and γ-phases depends on the OH^- concentration and the properties of the cations in the solution, since these are intercalated between the sheets [20]. Aging or making potential sweeps in alkaline solution transforms the α-$Ni(OH)_2$ to β-$Ni(OH)_2$ with a volume decrease of 59% due to the radical decrease in the interspaces between the sheets. However, if the thermodynamically unstable α-$Ni(OH)_2$ phase is immediately positively charged it will be transformed to γ-NiOOH. Upon reverse charging the γ-phase may be reversed back to α-$Ni(OH)_2$ or more likely, directly to β-$Ni(OH)_2$ [19]. After some time or after potential cycling in alkaline solution the system stabilises in the β-position and the γ-NiOOH phase can only be regained by overcharging of the system.

2.1.3 Cyclic Voltammetry on Nickel Electrodes

Cyclic voltammetry (CV) can reveal a lot of information about the formation of oxides and hydroxides on nickel electrodes in alkaline solution and this will be discussed in relation to Figure 2.2 and the currently available literature.

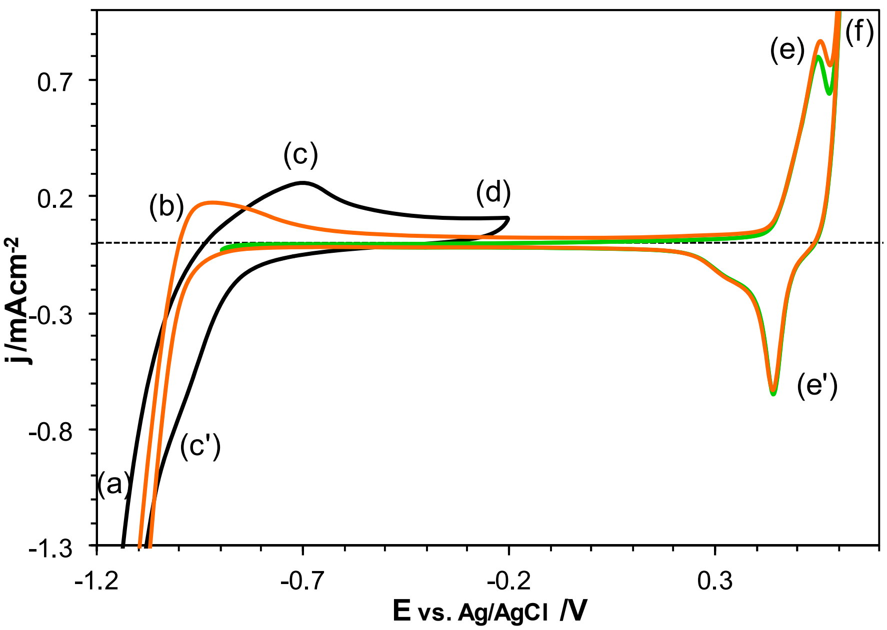

Fig. 2.2 Cyclic voltammetry on a polished solid nickel electrode in 0.1 M KOH, 100 mVs^{-1}, 1200 rpm. 2:nd sweeps are shown; ▬ -1.3(60 s) →-0.2→-1.3 V, ▬ -0.2 →-0.9→0.62→-0.2 V, ▬ -0.2 →-1.3→0.62→-0.2 V.

Hall et al. [25] recently concluded, by studying the surface characterisation results of their own and others [26-28], that air oxidised nickel has a bi-layer composition with α-Ni(OH)$_2$ at the oxide/solution interface and non-stoichiometric NiO$_x$ at the oxide/metal interface [25, 27]. If the nickel electrode is immersed in an alkaline solution the bi-layer composition remains intact but is thickened [27]. If a newly polished electrode is inserted into a 0.1 M KOH electrolyte and a potential sweep is made from the open circuit potential in the negative direction, a small peak will appear prior to the hydrogen evolution (notation (c') in Fig. 2.2). Peak (c') is believed to be the reduction of the α-Ni(OH)$_2$ or NiO$_x$ [29-30]. Peak (c') is seen more clearly if the potential is held at highly reducing potentials for some time before the full sweep is made (black curve, Fig 2.2) [25]. The β-Ni(OH)$_2$ phase is, however, not reduced at (c') and α-Ni(OH)$_2$ will quite rapidly transform into the more stable β-phase, peak (c') is therefore only seen at the very initial state of a CV measurement. However, the reduction of α-Ni(OH)$_2$ is not considered to continue to completion but rather leave some oxidised species at the metal surface.

At further negative potentials water reduction with extensive hydrogen gas (H$_2$) formation will occur (a) and hydrogen adsorption takes place as well, which can penetrate into the nickel metal as absorbed hydrides [25, 27, 30]. If the direction of the potential sweep in the H$_2$ evolution region is shifted in the positive direction an anodic peak (c) and possibly a pre-peak (b) will be obtained shortly after the cease of the H$_2$ evolution, followed by an anodic plateau (d). Peak (c) and a part of the plateau corresponds to the oxidation of Ni to α-Ni(OH)$_2$ or NiO$_x$ and at the end of this plateau β-Ni(OH)$_2$ starts to form and is also converted from α-Ni(OH)$_2$. The current plateau at (d) decreases with potential cycling, which may be explained by the thickening of the compact NiO layer that, in contrast to Ni(OH)$_2$, acts as a counter ion barrier towards the charged Ni surface and lowers the double layer charging [27]. However, the whole picture is further complicated by the charge increase in this region during the time the electrode is exposed to potentials for H$_2$ evolution (Fig. 2.2 ▬), and the lack of a reasonable sweep rate dependence (*i* vs. v or $v^{1/2}$, Section 3.1.2) of both the peak and the plateau [25]. Hall et al. [25] argue that both the sweep rate dependence and the results from electrochemical quartz micro balance (EQCM) indicate that a large part of the underlying plateau (d) is more likely to be due to the oxidation of absorbed hydrides and its diffusion through the metal as well as oxidation of adsorbed hydrogen. Others argue that the hydrides and hydrogens are released anodically as seen in the first oxidation peak (b) [27, 30] and that the plateau is a mixed effect of thickening of the oxide and double layer charging.

When the potential is made more positive a fairly steep oxidation peak arises (e), which is the oxidation of α/β-$Ni(OH)_2$ to γ/β-NiOOH and shortly after this, oxidation of water (Eqn. 2.5) will occur (f). During the O_2 evolution, the sweep in Figure 2.2 is switched in negative direction and when the potential is no longer positive enough, the O_2 evolution will cease and the reduction of γ/β-NiOOH to $(\alpha)/\beta$-$Ni(OH)_2$ starts and creates a cathodic peak (e').

The actual charge of the nickel ion in the different redox states is a well debated subject that would easily make a chapter by its own. Although the “hard” evidence pointing at the existence of nickel in valance state (IV) in an oxide matrix is sparse, there are rather few studies and limited data that support that direction. The Ni(IV) specie is believed to participate in the oxygen evolution reaction (OER) in the γ-phase and a few XAFS studies points in this direction even though the data appears to be difficult to interpret for this specific situation [21-23].

2.1.4 Nickel-Zinc alloys

As mentioned in Section 2.1.1, nickel actually started to serve human needs as an alloy and today the most common nickel alloys are of course steel of different qualities. In the case of plating the majority of products are ZnNi alloys with rather low Ni content (12-15%) which are used for corrosion protection or for replacing the zinc-iron and chromium coatings [31]. There are numerous scientific papers and patents published concerning zinc rich ZnNi alloys but very few published papers concerned with the corresponding nickel rich NiZn alloys.

The phase diagram for the NiZn system has previously been constructed by many authors where the results from thermodynamic calculations are in reasonable agreement with experimental data [32-33]. Most of the data for the NiZn phase diagram were obtained several decades ago and a few corrections have been suggested in more recent calculations [34]. In the phase diagram seen in Figure 2.3 some of the suggested corrections through the years are included. The main components of the NiZn system is the liquid phase (L), the intermetallic phases β, β_1, γ, and δ as well as the terminal solid solutions of *fcc* Ni and *hpc* Zn. The solubility of Ni in Zn at 20° C is very low while the solubility of Zn in Ni amounts to about 13-26 % depending on the chosen reference. At room temperature the β_1 phase is stable with a solubility range from 45.5 to 51.8% Zn. The suggested corrections by Xiong et al. [34] are particularly interesting for alloys synthesised in this work because it changes the expected phase from a solid solution to some intermetallic-like phase. The correction suggested by Xiong is shown with a dashed red line and is approximated to a straight line in Figure 2.3.

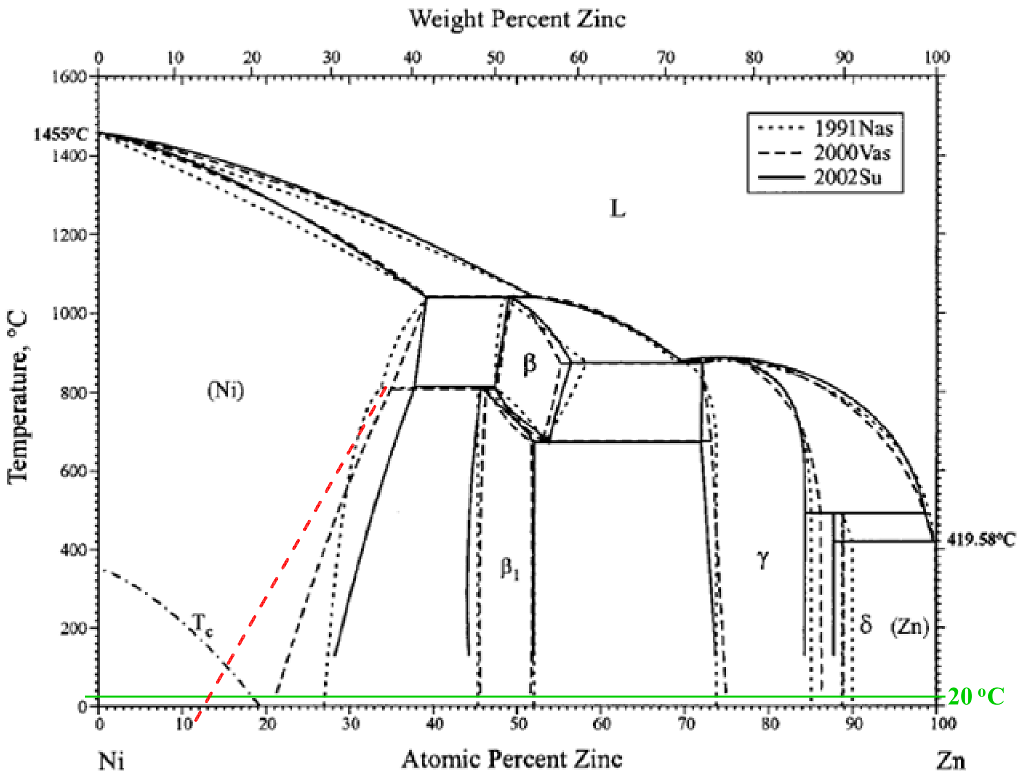

Fig. 2.3 Phase diagram of the NiZn system [32] with an additional suggested correction - - - [34] in the region of $Ni_{80}Zn_{20}$ which is of interest in this thesis. Reprinted by permission [32].

The thermodynamic reduction potential for nickel (Eqn. 2.1) and zinc differ by about 1 V.

$$Zn^{2+} + 2e^{-} \leftrightarrows Zn \qquad E^{o} = -0.762 \text{ V vs. SHE } (-0.959 \text{ V}) \tag{2.4}$$

Both Ni [35-37] and Zn [38-39] show underpotential deposition (UPD) on platinum and when the two are combined the current density is so high that anomalous co-deposition can occur [40-42]. Strictly, UPD refers to deposition of a metal at a more positive potential than the equilibrium potential predicted by Nernst equation. In practice, the phenomenon of UPD can be explained briefly by stating that when the work function of the substrate is higher than for the metal to be deposited, the reduction potential will, in most cases, be reduced [43]. The trend is most often such that the larger the difference is in work function between the substrate and the ad-atom, the larger the magnitude of the UPD is [43-44]. The UPD will, however, decrease or cease once a monolayer of the ad-atom has been plated on the substrate since the work function of the adsorbed layer then approach the on-state of the ad-atoms [43]. Anomalous co-deposition occurs mainly between metals in the d-group, when two ionic species in a plating solution deposit in a composition with a larger ratio for the less noble metal ion over the nobler one compared to the ratio of the species in solution. At low current densities any two metal ions co-deposit normally i.e. the more noble metal deposits preferentially (as their reduction potential, E^{o}, is less negative), but if the current density is increased to a value high enough, there may be a transition to a state where the less noble metal deposits preferentially - the transition current density. The value of the transition current density and the impact of it vary substantially with the metal ion ratio and its concentration, with the bath temperature as well as with pH and agitation of the solution [45].

The NiZn system is known to deposit anomalously but the mechanism behind the deposition is still not fully understood and hence will not be further discussed in this thesis [40-42].

2.2 Oxidation and reduction reactions studied

2.2.1 Oxygen Reduction Reaction

The oxygen reduction reaction (ORR) is possibly the most studied “oxygen reaction” in electrochemistry and numerous publications have been produced since the “discovery” of oxygen in 1773. Scheele and Priestley are usually credited for this discovery since they were the first to study the properties of separated oxygen, even though Leonardo da Vinci recognized it as a constitute of the air, which supported combustion 300 years earlier [4]. The indefatigable and increasing interest for chemistry involving oxygen is due to the fact that it is involved in key reactions on several levels for the development of a more environmental friendly and sustainable society. Oxygen is today considered to be the only available fuel on the cathodic side in fuel cells for common use. Unfortunately the ORR is quite slow, which also makes it to the limiting reaction in most fuel cell systems and may be responsible for up to 2/3 of the energy loss in a PEMFC [2, 46]. The metal air battery research is a second field of renewed interest in this topic and in this application as well the slow kinetics of the ORR is considered to be the main limiting factor [47]. The complexity of the ORR is further increased by the two possible reduction products, water and hydrogen peroxides (H_2O_2). In a fuel cell it is crucial to withdraw the maximum energy of each O_2 molecule, which means a $4e^-$ reduction to water and not a $2e^-$ reduction to H_2O_2. Hydrogen peroxide on the other hand is a valuable chemical for many applications (Section 2.3) but can also be detrimental in a fuel cell.

The possible reactions involved in the ORR and the thermodynamic standard potentials for the direct $4e^-$ oxygen reduction and the consecutive $2e^-$ reduction in acidic (pH 0) and alkaline (pH 14) solution are given in Eqn. 2.5-12 [13] (potentials vs. Ag/AgCl (KCl sat’d) are given in parenthesis).

$$O_2 + 4H^+ + 4e^- \leftrightarrows 2H_2O \qquad E^o = 1.229\ \text{V vs. SHE},\ (1.032\ \text{V}) \qquad (2.5)$$

$$O_2 + 2H_2O + 4e^- \leftrightarrows 4OH^- \qquad E^o = 0.401\ \text{V vs. SHE},\ (0.204\ \text{V}) \qquad (2.6)$$

The ORR for the first of the two consecutive $2e^-$ reductions in acidic media is written

$$O_2 + 2H^+ + 2e^- \leftrightarrows H_2O_2 \qquad E^o = 0.695\ \text{V vs. SHE}\ (0.498\ \text{V}) \qquad (2.7)$$

followed by a second $2e^-$ reduction

$$H_2O_2 + 2H^+ + 2e^- \leftrightarrows 2H_2O \qquad E^o = 1.776\ \text{V vs. SHE}\ (1.579\ \text{V}) \qquad (2.8)$$

or by disproportionation

$$2H_2O_2 \rightarrow 2H_2O + O_2 \qquad (2.9)$$

The corresponding $2e^-$ reactions in alkaline solution is

$O_2 + H_2O + 2e^- \leftrightarrows HO_2^- + OH^-$ $\quad$ $E^o = -0.076$ V vs. SHE (-0.273 V) $\quad$ (2.10)

followed by a second $2e^-$ reduction

$HO_2^- + H_2O + 2e^- \leftrightarrows 3OH^-$ $\quad$ $E^o = 0.878$ V vs. SHE (0.681 V) $\quad$ (2.11)

or by disproportionation

$2HO_2^- \rightarrow 2OH^- + O_2$ $\quad$ (2.12)

The potential dependence with pH for the reactions above is governed by the Nernst equation and preferably visualised in a Pourbaix diagram, where the lines are the thermodynamic equilibrium. A change in the potential or pH will favour the species marked above or under the line.

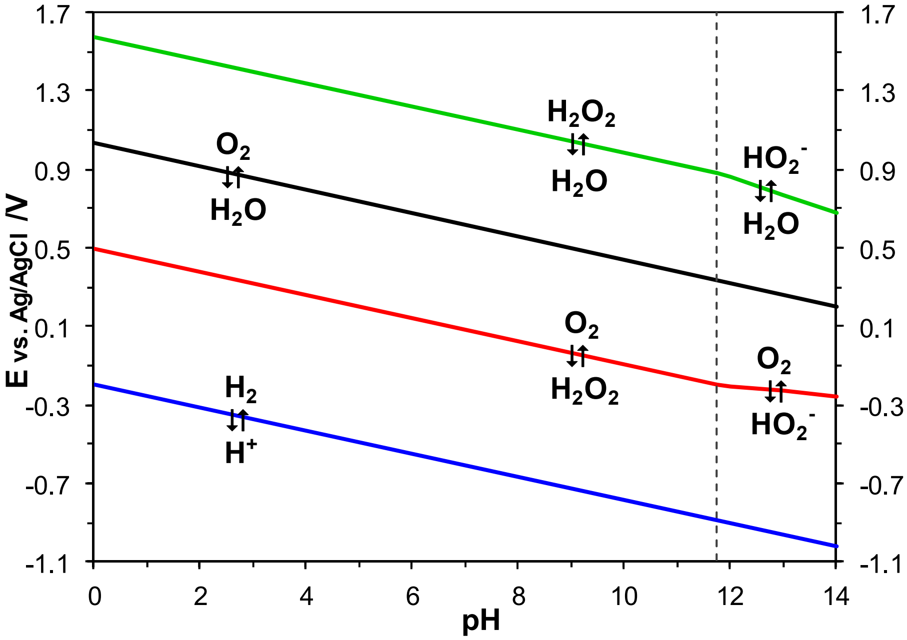

Fig. 2.4 Pourbaix diagram for the ORR, Eqn. ▬ (2.14), ▬ (2.7), ▬ (2.5) and ▬ (2.8). The dashed line marks the pKa for H_2O_2 from which the potential-pH relation changes.

Numerous studies have been done to determine intermediates species that take part in a suggested reduction path. In the most ambitious attempt to include all possible reaction paths in the ORR more than 20 rate constants have been deduced [48]. It is, however, not possible to experimentally discriminate between all these rate constants and from a practical point of view a far less complicated reaction scheme is preferable (Fig. 2.5).

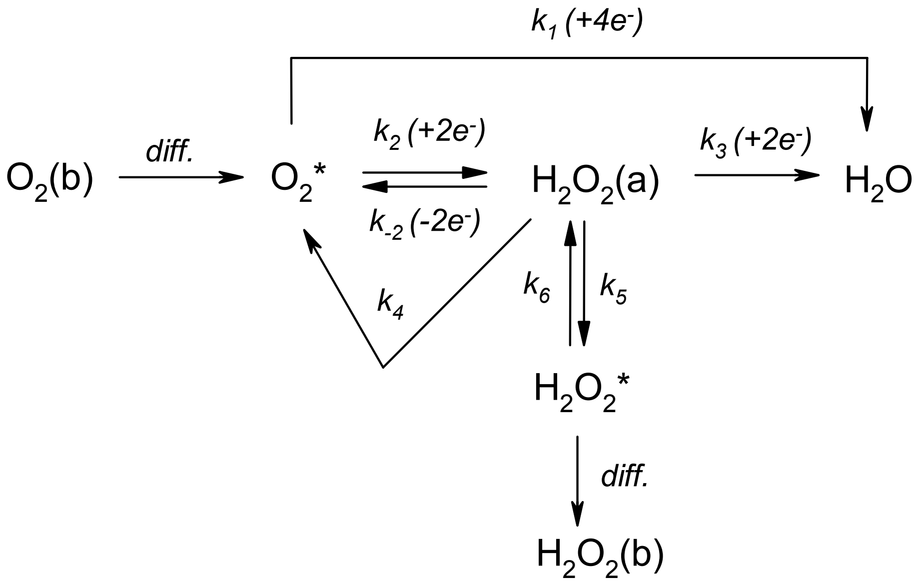

Fig. 2.5 Reaction scheme for oxygen reduction in neutral solution suggested by Wroblowa et al. [49]. Denotations of species: b = bulk, * = vicinity of the disc electrode, a = adsorbed.

It may also be emphasised that the overpotential needed for the oxygen reduction to proceed varies substantially with electrode material and electrode environment. The reduction path may also be potential dependent.

For the ORR there are some previously known and well documented systems that suite as examples of almost pure $4e^-$ and $2e^-$ reduction paths using platinum (Pt) and carbon (C) electrodes, respectively. The oxygen reduction path on gold electrodes on the other hand has the peculiar property of being affected by the surface coverage of OH^-. A high coverage of OH^- makes the $4e^-$ reduction prevail and without the hydroxide cover there exist mainly the $2e^-$ reduction, this makes the ORR pH and potential dependent [50]. Such type of electrode properties are simulated for a rotating ring disc electrode (RRDE) experiment (Section 3.1.3) and are shown in Figure 2.6. In the simulation the reaction paths denoted k_2, k_3 and k_5 (Figure 2.5) are given and N is set to 0.5. At the first plateau for the disc current (a) and the response on the ring (a') a $2e^-$ reduction takes place, but as the potential changes, the properties of the electrode towards O_2 reduction changes and the full $4e^-$ reduction takes over (b) and there will be no H_2O_2 to be detected on the ring (b'). In the case of platinum the currents will follow the red dashed lines (---) with a high activity for O_2 reduction but with almost no detection of H_2O_2 and the carbon will follow the black dashed lines (---) and have a low activity for O_2 reduction and gives very little reduction to water.

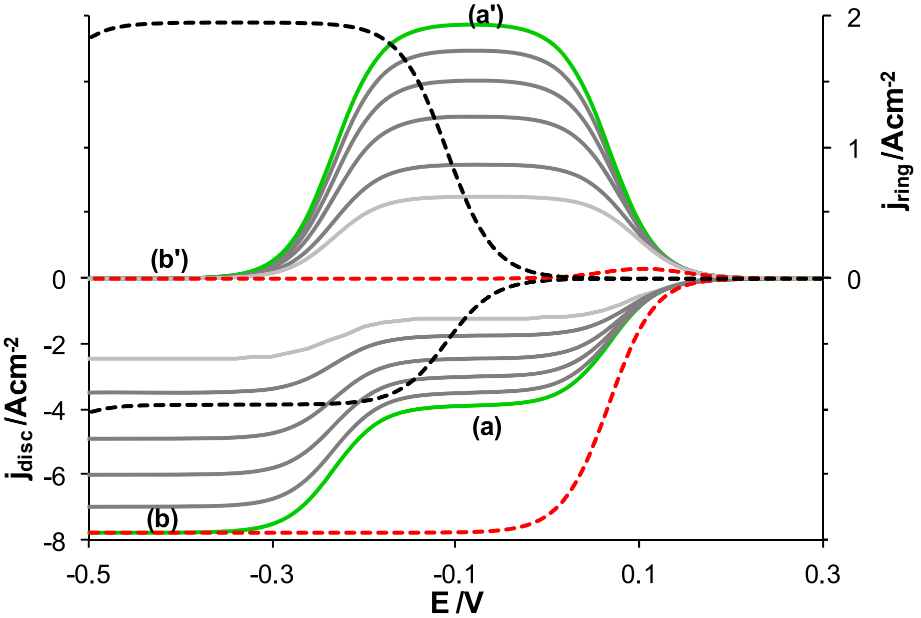

Fig. 2.6 RRDE simulation of the ORR on ━Au(×6), ---Pt and ---GC discs. The ORR proceeds through the reaction paths denoted k_2, k_3 and k_5 in Fig. 2.5.

Both platinum and carbon are very stable for prolonged use in both acid and alkaline media and are e.g. (still) the main anode and cathode material in low temperature (PEM) fuel cells. The role of carbon is to act as a conducting high surface area substrate on which Pt nanoparticles can be distributed to maximize the effect to volume ratio of the cell. Platinum anodes and cathodes are however not the ultimate catalysts for several reasons. One of the reasons is the limited reserves of platinum on the earth and this fact will complicate its role as a real alternative in the complete replacement of the fossil fuel engines. For this basic reason it is obvious that other more accessible electrode materials need to be developed, possibly also in a more elaborate energy system.

This thesis will however focus on the 2e$^-$ reduction of oxygen to H_2O_2. For this reaction carbon electrodes may seem ideal with its primary 2e$^-$ pathway and high stability in virtually any media. However, the overpotential on GC is quite high and the efficiency will therefore be very low. The primary task will be to investigate catalysts that will lower the overpotential for ORRs with a dominant 2e$^-$ reduction pathway.

2.2.2 Oxygen and Hydrogen evolution reactions

The oxygen evolution reaction (OER) occurs when the potential of an electrode is set positive enough for the water in the electrolyte to split into O_2 and protons (reverse of Eqn. 2.5-6). The hydrogen evolution reaction (HER) on the other hand occurs when the potential is set negative enough to split water into H_2 and hydroxide ions (Eqn. 2.13). In the case of an acidic electrolyte proton reduction (PRR) (Eqn. 2.14) to H_2 will occur prior to the water splitting. The onset potentials for the oxygen and hydrogen evolution also sets the analytical limits for an electrochemical experiment in aqueous media, since the anodic and cathodic currents will increase infinitely (at OER and HER) and will hide any other current contribution.. The thermodynamic equilibrium potentials in pure water (Eqn. 2.5 and 2.13) provide a potential window of 1.2 V. However, in a practical experimental setup substantial deviation from the thermodynamic values (overpotential) will be seen due to the properties of the electrode material and its environment. The source of hydrogen for the hydrogen evolution changes from protons in acid solution (Eqn. 2.14) to water in alkaline solution (Eqn. 2.13) and the equilibrium potential decreases linearly with pH (Fig. 2.4). The corresponding behaviour can be seen for the OER where the oxygen source changes from water (Eqn. 2.5) to hydroxide ions (Eqn. 2.6).

$2H_2O + 2e^- \leftrightarrows H_2 + 2OH^-$ $E^o = -0.8277$ V vs. SHE (-1.024 V) (2.13)

If an excess of protons are present in the electrolyte the HER will be facilitated in what is called the proton reduction reaction (PRR) (Eqn. 2.14).

$2H^+ + 2e^- \leftrightarrows H_2$ $E^o = 0.000$ V vs. SHE (-0.197 V) (2.14)

In a rotating disc experiment in an acidic aqueous electrolyte, reaction (2.14) can be seen as a plateau from where its concentration can be determined since the electrode at this potential will not reduce water. A further increase of the potential will generate H_2 evolution from reaction (2.13) which will increase “infinitely” as long as there is water available to the electrode.

The OER can be a wanted or an unwanted reaction depending on the application of the system and substantial efforts have been made to both suppress and to facilitate this reaction. The oxygen evolution can be an obstacle if it appears simultaneously as another reaction and may hinder or slow down the reaction of interest. This is a previously known problem for the chlorine producing industry where O_2 evolution appears as a competing reaction to the Cl_2 evolution. In the chlorine process the dimensional stable anodes (DSA), which are titanium electrodes covered by ruthenium and iridium oxide catalysts, are used. The DSA electrodes favour both processes but even though the O_2 evolution has a thermodynamic advantage over Cl_2 evolution the OER needs a higher overpotential to proceed in any substantial amount. In the last decades however, the focus on the OER has been more diverse and an increasing interest in lowering the overpotential for the O_2 evolution can be seen in a number of publications [21, 51-55]. A great deal of the increased interest concerns with the anode process in the production of H_2 (for fuel or energy storage) and in metal air batteries which both are critical in the future energy and transport systems. In any application it is critical that the overpotential for the anode reaction (the OER) is kept as low as possible.

The HER is of equally fundamental importance as the ORR and OER as these reactions are all essential parts of the hydrogen economy. Electrochemically produced hydrogen is clean, free of CO which is detrimental for noble metal electrode material and free of CO_2 exhausts to the environment. This is of course only true if the energy to drive the HER is emission free or at least CO_2 neutral. The most appealing energy sources for water splitting is of course from renewable energies, of which solar power is seen as the most likely source in a long term solution, but whatever method used it is crucial for the energy efficiency that the overpotential for the reactions is low [52, 56-59].

2.2.3 Oxidation of organic molecules on nickel electrodes

It has been known since the beginning of the twentieth century that organic species can be oxidised electrochemically and that nickel is an interesting electrode material for such processes. Since then a number of refining processes for organic compounds by the use of nickel electrodes have been developed [5-9]. The organic oxidation reactions on nickel and the understanding of the mechanism that governed the interaction between the $Ni(OH)_2/NiOOH$ (Eqn. 2.3) and an adsorbed organic molecule puzzled the researchers to begin with. The suggested reaction mechanism for the oxidation of simple alcohols and amines on nickel proposed by Fleischmann in 1971 [60-61] was debated at that time [62-63]. The nickel redox couple has however, constantly attracted new interest for electrochemical processing of various organic molecules, both for its commercial potential but also for its intricate interaction with the reactants [64-67].

The research on fuel cells has been going on for more than a century with varying intensity and when fuels like methanol and ethanol became a prioritised topic new electrode materials needed to be developed. Platinum which has been the ruling anode and cathode material in PEMFCs suffers severely from CO and aldehyde poisoning, which are inevitable bi-products when organic fuels are used. Nickel and nickel alloy electrodes are less sensitive for poisoning by those bi-products and have been treated in the literature as possible anodes in methanol [68-71] and ethanol [72] fuel cell applications. Electrochemical co-generation of chemicals and electricity is a research topic of increasing importance and a great challenge for the electrochemical society. In a previous review, Alcaide et al. [3] concluded that the co-generation setups developed so far have not proven to be economically profitable and at present are of academic interest. It appears as the co-generations setups so far have not been optimized to their actual task, i.e. it is more of a fuel cell technology rapidly converted to a co-generation module. This becomes quite clear from Table 2 in the review by Alcaide where most of the anode and cathode material contains platinum or some other noble metal [3].

2.3 Hydrogen Peroxide

2.3.1 H_2O_2, the ultimate chemical reactant

Hydrogen peroxide (H_2O_2) was discovered by Louis Jacques Thénard in 1818 which he first produced by reacting barium peroxide with nitric acid and later by hydrolysis of peroxodisulfates [4]. This technique was used until the middle of the 20th century when it was replaced by the antraquinone process, which essentially is the same process that is in use today. Hydrogen peroxide is in many aspects the ultimate environmentally friendly reactant in any chemical process with only water and oxygen as bi-products. It is known as one of the most powerful oxidisers in acidic solution stronger than chlorine, chlorine dioxide and potassium permanganate and it can be used as an oxidising agent as well as a reducing agent. Its chemical properties are significantly altered with pH i.e. it oxidises a compound in acidic solution and it can reverse this process in a basic solution (e.g. $[Fe(CN)_6]^{4-}/[Fe(CN)_6]^{3-}$ and Mn^{2+}/MnO^{4-}), the change in standard potential with pH can be seen in Figure 2.4 [4]. H_2O_2 are used in a large variety of applications such as waste water treatment, disinfection, etching and purification of electronic materials, metal extraction, chemical refinement etc. [4, 73]. The by far biggest consumer of H_2O_2 (~50%) is however the pulp industry where it has replaced the chlorine step in the bleaching process [74]. New fields of the use of this diverse chemical are constantly developed and virtually any process that can be replaced by use of H_2O_2 is beneficial for the environment.

During the last decade some new ideas about the use of hydrogen peroxide have been proposed. The fuel cell based hydrogen economy is troubled by some fundamental issues that are difficult to circumvent, such as expensive electrode material, expensive membranes that still generate efficiency loss and the inconvenient transport of compressed H_2. A recent suggested solution to some of these problems is the use of H_2O_2 as both cathode and anode fuel [75-76].

Since H_2O_2 can be both oxidised and reduced selectively by some electrode material, such as Au and Ag respectively, no membrane between the electrodes is needed. In a future H_2O_2 economy it should also be possible to generate H_2O_2 by O_2 reduction in aqueous solutions connected to solar panels [76].

2.3.2 H_2O_2 production and future perspectives

Hydrogen peroxide is one of our most important chemicals contributing for about 12-15% of the total global chemical revenues. The annual global production is approximately 3.8 million tons [77] and it is forecast to reach 4.7 million tons by 2017 [78].

Today the producers of H_2O_2 mainly utilise the antraquinone process in which a solution of 2-ethylanthraquinone or 2-amylanthraquinone is hydrolysed to 2-(ethyl/amyl)anthraquinol by H_2 on a palladium or Raney nickel catalyst. The anthraquinone solution is then bubbled with O_2 which reacts with the recently formed alcohol groups on the 2-(ethyl/amyl)anthraquinol to form H_2O_2 and the catalyst is reversed back to its ketone form. The formation of H_2O_2 is followed by several extraction and clean-up processes to generate a useful product [4, 77]. This is a quite complicated process and demands large scale production plants (>40 000 tons/year) to be profitable and to cut costs further, newer plants have capacities of several hundred thousand tons per year. The world's largest plant was built by Solvay and Dow in 2011 with a capacity of over 330 000 tons per year of 100% H_2O_2 of which most of it will be used in the HPPO process to produce propen oxide [79].

Even though H_2O_2 is an environmentally friendly chemical it can still be hazardous to humans during handling in its concentrated form. Since it is a very strong oxidiser it causes burns in contact with skin and a second issue is the risk of explosive decomposition. H_2O_2 does not decompose by itself but very small amount of almost anything (light, metals, trace of alkalis from a glass container or even dust) may generate dangerous decomposition. Stabilisers are then necessary to add to the solution to make transportation and storage safe and economic. Typical stabilisers are stannate(IV) and various phosphates [4, 77].

Due to the character of H_2O_2 as well as a general desire to reduce transportation of chemicals and goods, development of smaller on site production plants would be preferable in many cases. Direct synthesis of hydrogen peroxide from H_2 and O_2 has been of interest for many years and a lot of research has been undertaken in this field. The fundamental issues are connected to thermodynamics, which favours a full reduction of O_2 to H_2O. A successful catalyst for hydrogen peroxide formation should stop the reduction process after two electrons ($2e^-$) have been transferred. Palladium and gold are known since almost a century to support the $2e^-$ reduction and in principle all research on this topic appears to be focused on optimising the ORR on Pd, Au or Pd-Au supported on different oxide substrates [73, 80-81]. An additional problem is the mixing of H_2 and O_2 in the same chamber and to avoid explosions very dilute mixtures (outside the explosion limit 5 - 94 vol% of H_2 in O_2) or H-only permeable membranes have to be used at the cost of efficiency [73]. Quite recent improvement of micro reactors is maybe the most promising development within the small scale production of H_2O_2 [82].

Another well investigated possibility of making H_2O_2 is by electrochemical reduction of O_2 in aqueous solution, where the protons are supplied by the water and the electrons are supported by an electric current (section 2.2.1). The problems with the thermodynamics of this process are the same as mentioned above but the potential can be controlled and set to a value that favours a 2e- reduction to H_2O_2. The fundamental problem with this method is the slow kinetics of the ORR, and the main task for the development of such a method is to find an electrode material that reduces the inherent large overpotential during a dominant peroxide pathway. Carbon electrodes are cheap and carbon is a durable material with a prevailing 2e$^-$ pathway but with a fairly high overpotential. Subsequently numerous surface modifications have been tried with some success to increase the reaction rate [83-86]. In the noble metal category Au and Au-Pd alloys [87] are probably the most interesting materials unfortunately with high costs as the down side. Of the transition metals it is cobalt in different complexes that has shown the most promising results with a high yield of H_2O_2 [88-89]. If a catalyst with good yield, low overpotential and high durability is achieved it will be of great interest since it then can be used in an electrolysing device or in a fuel cell application or even in combined H_2 and H_2O_2 production, depending on the available energy source [76, 85, 90].

3 | Survey of Methods

3.1 Electrochemical Methods

This chapter is written to help a reader with general chemistry background to understand the basic concept of the measurement techniques used in this work. The survey of these methods is meant to be descriptive rather than mathematical and only the equations closely related to, or used in this thesis are shown. For a deeper understanding of the electrochemical part the two books *Electrochemical Metods* [91], *Instrumental Methods in Electrochemistry* [92] and *Modern Electrochemistry* [93] are recommended, which also have been the main guidance in this work.

3.1.1 Electrochemical setup

All electrochemical measurements have been performed in a single compartment three electrode cell (Fig. 3.1(a)). The counter electrode (CE) was of platinum and the reference electrodes (RE) were Ag/AgCl (KCl saturated, with E = 0.197 V vs. SHE) and SCE (Hg/Hg_2Cl_2 KCl saturated, with E = 0.2412 V vs. SHE). The working electrodes (WE) used for controlled hydrodynamic measurements were the rotating disc electrode (RDE) (Fig. 3.1(b1)) or rotating ring disc electrode (RRDE) (Fig. 3.1(b2)) with a disc diameter between 3 and 5 mm casted in epoxy. For structural investigations of NiZn alloys in XAFS Pt foil electrodes of the size 4 × 12 mm were used and for the product analysis in DEMS a fine Pt mesh with the diameter of 8 mm was used (Fig. 3.1(c) and (d)). Type (c) and (d) electrodes had a Pt wire attached as contacts during the electrodeposition.

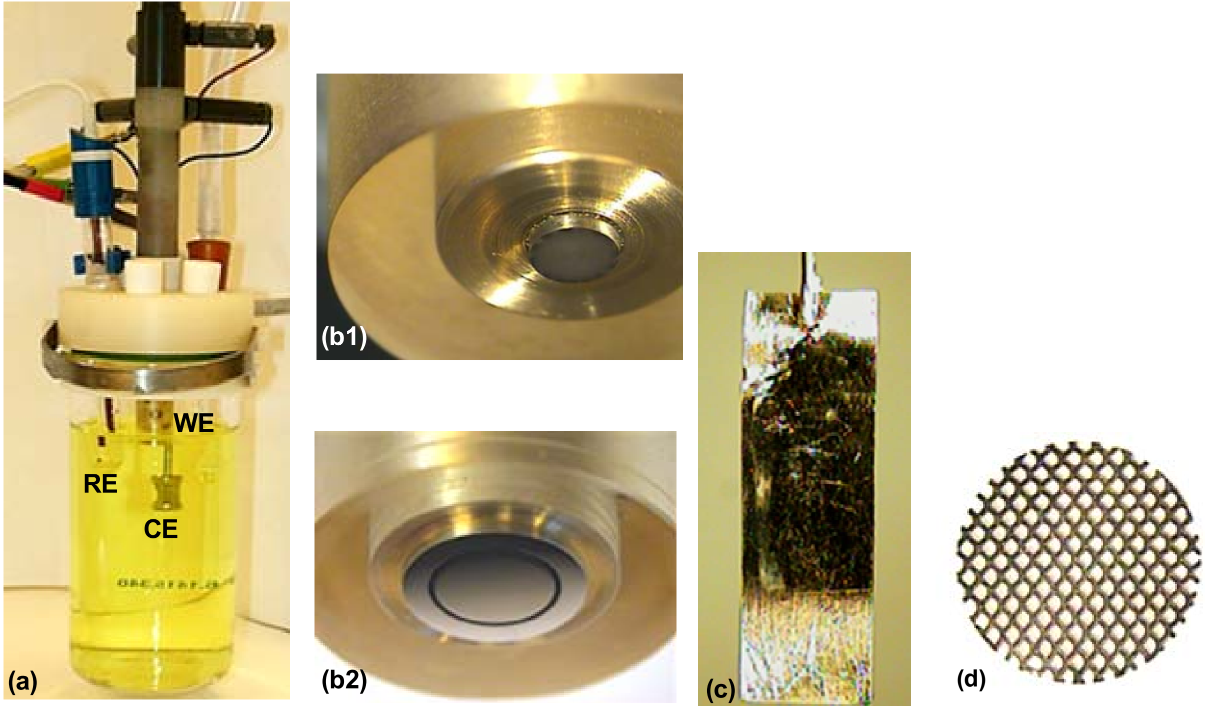

Fig. 3.1 (a) Electrochemical setup for the RRDE experiments. (b1) A RDE (seen from the side in (a)) plated with NiZn. (b2) A RRDE (Ni disc and Pt ring). (c) Pt foil electrode. (d) Pt mesh electrode plated with Zn.

3.1.2 Cyclic Voltammetry

Cyclic voltammetry (CV) is one of the most frequently used methods for qualitative analysis of electrochemical systems [91]. CV is a potential sweep method in which the applied potential changes linearly with time and the current is measured as a function of the changing potential. In practice the current is usually plotted as a function of potential at a certain sweep rate (v) (Fig. 3.2). The term CV implies that the direction of the sweep is changed at some potential value and the same potential region can be re-examined but from another state of equilibrium and the cycling can be repeated numerously. The potential sweep methods offer quick, accurate and reproducible qualitative data and it is most often with this technique an electrochemical investigation begins, since it quickly reveals the potential region of the electrodic activity. From the CV data valuable information of the system can be extracted such as reversibility, coupled reactions, double layer capacitance, separation of surface and solution processes etc.

The reactions studied in this thesis are all inner-sphere reactions (i.e. involve breaking and forming bonds) it is therefore the only type of reactions that are considered in this background section. During the first scan in a CV experiment the sweep is commonly started at open circuit potential (OCP) where no net faradic current flows, the potential is then swept towards the formal potential of the expected reaction ($E^{o\prime}$ in Fig 3.2(a)). When the electrode potential is changed the electronic state of the electrode is changed and when its Fermi level overlaps the energy of the HOMO or LUMO state of the species in contact with the surface, oxidation and reduction respectively, occurs. As soon as the restrictions of the energy levels are fulfilled for some of the surface sites the faradic limited current begins to flow at some value prior to the $E^{o\prime}$ of the reaction. At the $E^{o\prime}$ the Fermi level of the electrode matches the HOMO and LUMO equally and the concentration of O and R at the surface is equal. At potentials well beyond the $E^{o\prime}$ (at the other side of the peak) only one of the electronic states will be available for electron transfer and only product species will be formed.

In the case of reactants in the solution the current profile in a potential sweep can be explained by dividing the current into two parts, the faradic current i_F and the current limited by time i_L in $i=(i_F i_L)/(i_F+i_L)$. The diffusion layer (δ) grows with time as $\delta=\sqrt{\pi D t}$ (Eqn. 3.5-6), $i_L \propto \delta^{-1}$ (as $i_l=nFADC^b\delta^{-1}$) and is then determined by time in $i_L \propto (\sqrt{t})^{-1}$ i.e. the time length of the sweep. During the initial curve rise, the current is limited only by i_F since δ is still small and i_L is large, but as the sweep continues δ increases and the influence of i_L eventually starts to dominate over i_F due to the depletion of reactants near the electrode and the current starts to decrease which forms the peak in a voltammogram. As the sweep continues the current will at some point be more or less completely determined by the rate of the diffusion of reactants from the bulk to the electrode surface. Theoretically the current would go infinitely small but in practice natural convection puts an end to the growth of the diffusion layer and a steady-state current will be obtained. If the sweep rate is increased (within the same potential range) i_F will increase exponentially like before but i_L will only limit the current as a function of time. Since the same potentials now are reached faster the limiting effect of i_L will be smaller, therefore the current for the whole peak will increase (Eqn. 3.1-2). The current in CV is always determined by the concentration gradient at the electrode surface and a faster sweep rate generates a sharper gradient as a consequence of the shorter time of the diffusion layer build up (Fig 3.2(a)▬).

In the case of surface bound reactants the diffusion term is not present (in an ideal system) and the shape of the peak in a CV is governed by how the reacting specie interacts with its neighbour (O or R) on the surface and the peak potential (E_p) can therefore change in relation to $E^{o\prime}$. The curve starts at zero current and ends at zero current when all the surface confined species have reacted (Fig 3.2(a)▬) and the area under the peaks can therefore be related to the coverage (Γ) of the reacting specie ($\Gamma_{reactant} = |Q/(nF)|$). In a reversible system the anodic and cathodic peaks are symmetric with the same E_p and at i_p when half of the surface confined species have been oxidised or reduced ($E^{o\prime}$). In an irreversible system however, the peak is distorted and there is no reverse peak, and for a quasi-reversible reaction the peaks are asymmetrical with a clear difference in E_p.

By making several CVs with different sweep rates or at different concentrations useful information about the system can be obtained. Two basic examples are shown in Figure 3.2(c) where the relation between i_{pa} and i_{pc}, and the peak potential difference, ΔE_p, are important diagnostics in the determination of the reversibility of a reaction.

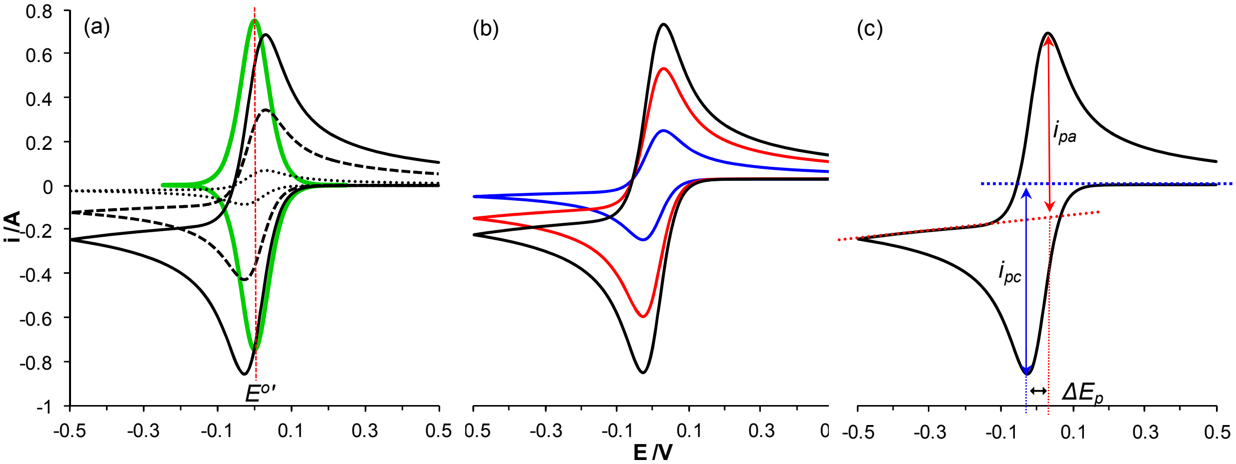

Fig. 3.2 Simulated CV in negative sweep direction, (a) sweep rate dependence of reactant in solution, ▬ 10, ▪▪▪5 and •••1 mVs^{-1} and ▬ strongly adsorbed reactant, --- shows the $E^{o\prime}$ in the CV for both solution and surface confined species. (b) Concentration dependence of reactant in solution, ▬ 10, ▬ 5 and ▬ 1 mM. (c) Basic diagnostics of a CV spectrum.

Detailed analytical descriptions have been formulated to describe the different currents and potentials from electroactive species both in solution and at the surface during a potential sweep experiment. However, only the final expressions and diagnostic criteria that directly concern this thesis will be presented here.

For *species in solution* the peak current can be mathematically described by solving Fick's second law for diffusion with appropriate boundary conditions, however, the change of potential with time makes a numerical solution of this problem necessary. The analytical-numerical expression for the peak current for a reversible electron transfer (RET) reaction with the reaction $O + ne^- \leftrightarrows R$ at the electrode surface in a solution containing only species O is written as

$$i_p = 2.69\times10^5 n^{3/2} A D_O^{1/2} C_O^{b} v^{1/2} \tag{3.1}$$

For an irreversible electron transfer (IRET) Eqn. 3.2 is valid if $n = 1$. If $n > 1$ for the total reaction there must be an irreversible heterogeneous one-electron rate limiting first step and this is the assumption used for calculating i_p for O_2 reduction.

$$i_p = 2.99\times10^5 \alpha^{1/2} A D_O^{1/2} C_O^{b} v^{1/2} \tag{3.2}$$

The Quasi-reversible electron transfer (QRET) reactions cannot be generalised like the RET and IRET since it depends on both the rate constant k and α. There are however, a handful of diagnostic criterions that can be used to separate the different processes based on simple CVs at different sweep rates. The most upfront criteria is the peak separation $\Delta E_p = E_{pa} - E_{pc}$ which for a RET is 59/n mV for any sweep rate, >59/n mV for a QRET and no reverse peak for IRET. This criteria must however, be tested for different sweep rates since a QRET can appear as RET at a certain sweep rate. The peak current dependence on the sweep rate is $i_p \propto v^{1/2}$ for both RET and IRET but not for the QRET even though it does increase with increasing sweep rate.

For *surface bound* electroactive species there is no diffusion boundary problem, i_p depends instead on Γ the coverage of adsorbed specie on the surface before the start of the sweep and the peak current for a RET can then be described as

$$i_p = (n^2F^2/4RT)\, vA\Gamma_O^{\,s} \tag{3.3}$$

and the corresponding expression for a IRET is

$$i_p = (\alpha F^2 vA\Gamma_O^{\,s})/2.718RT \tag{3.4}$$

Both Eqn. 3.3 and 3.4 are valid under the assumption that the adsorbed species follow a Langmuir isotherm which considers the fundamental adsorption step only (s.937 in [93]). The numerical values in Eqn. 3.1-4 are valid for 25 °C. The peak current dependence on the sweep rate is $i_p \propto v$ for both RET and IRET.

For many experimental conditions the electrochemical environment may however be more complicated, since a current can depend on the properties of the electroactive and the supporting species both in solution and bonded to the surface. Many adsorption interactions with a surface will not be explained by a simple Langmuir isotherm. An example of a more complex redox response can be exemplified by the diffusion of H^+ and OH^- within a layer of a metal hydroxide where the change in metal state is a surface process but where the need for ions in this process may become diffusion limited in porous structures.

3.1.3 Rotating Electrodes

The Rotating disc electrodes (RDE) and the rotation ring disc electrodes (RRDE) provide hydrodynamic control of the convective mass transport in a very attractive way. In the hydrodynamic technique considered in this thesis the electrode is rotated in the solution, though in other applications it may well be the solution that is moved relative to the electrode.

Hydrodynamic control is mostly used with potential sweep methods, whose advantages will be treated briefly here. Hydrodynamic control can however, also be used in e.g. chronoamperometry measurements. In Figure 3.3 the difference in current response of two potential sweeps ((a) from a stationary CV and (b) from a CV with electrode rotation) made in 0.1 M KOH and 5 mM hexacyanoferrate can be seen.

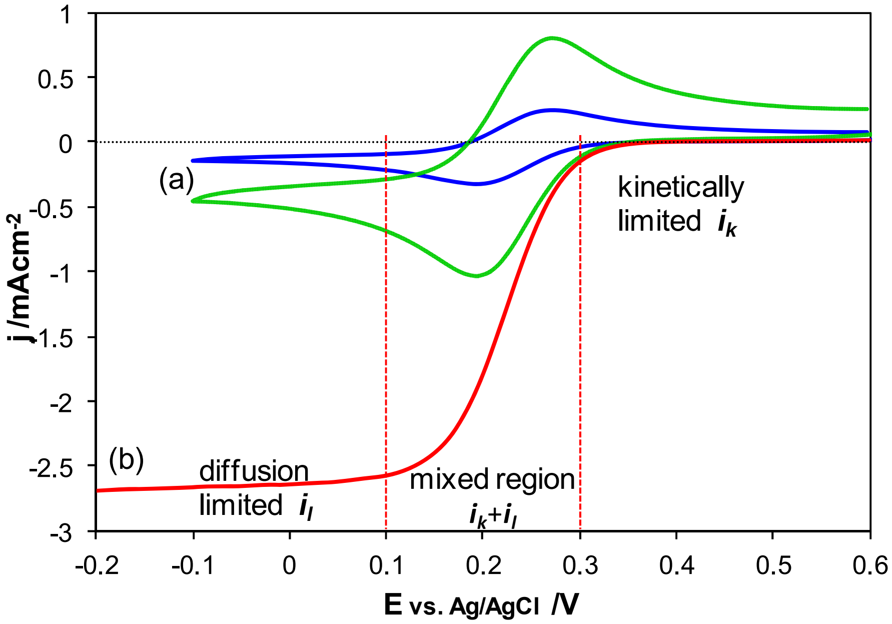

Fig. 3.3 CV on a Pt RDE in 0.1 M KOH with 5 mM hexacyanoferrate. (a) stationary CV at 🟦10 mVs^{-1} , at 🟩100 mVs^{-1} and (b) 🟥CV at 1200 rpm, 10 mVs^{-1}.

When CV is performed using electrode rotation the concentration gradient build up is considerably reduced compared to a stationary electrode and the current increases due to the larger flux of reactants to the electrode surface (Fig. 3.3). The rotation of the electrode generates a moving hydrodynamic region outside a stagnant layer that moves with the electrode. The hydrodynamic layer determines the thickness of the stagnant layer (which also becomes the diffusion layer) and generates a well-defined rotation dependent control of the diffusion limited current. The red curve in Figure 3.3 shows how (at steady state) the current is determined by the diffusion of reactants from the bulk concentration in the moving hydrodynamic layer, through the stagnant layer to the electrode surface (Fig. 3.4).

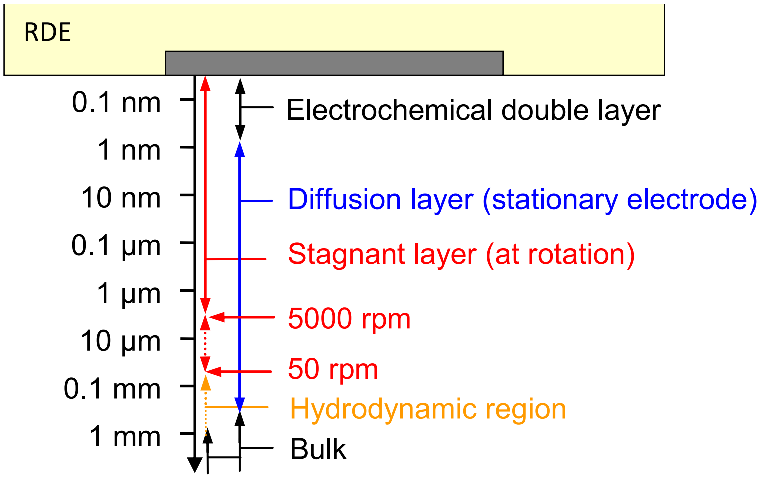

Fig. 3.4 Schematic figure of the different layers build up normal to an electrode surface at RDEs (red) and at stationary electrodes (blue). The thickness of the stagnant layer at 50 and 5000 rpm was calculated using Eqn. 3.7 and $D = 7.1\times10^{-6}$ cm^2s^{-1}.

A diffusion layer (δ) starts to build up as soon as a current or potential is applied to the system and is limited by natural convection at approximately 0.05 cm [93]. The term δ increases with the square root of time ($\sqrt{t}$) and the time variation differs when a constant current (3.5) and a constant potential (3.6) is applied.

$$\delta = \sqrt{\frac{4Dt}{\pi}} \qquad (3.5) \qquad\qquad \delta = \sqrt{\pi D t} \qquad (3.6)$$

The diffusion layer thickness for a rotating disc electrode was previously derived by Levich and is written.

$$\delta_O = \mathrm{D_O}/\mathrm{m_O} = 1.61 D_O^{1/3}\omega^{-1/2}\nu^{1/6} \qquad (3.7)$$

The relation between the limiting current (i_l) and δ_O is given by the mass transfer coefficient, $m_O = i_l/nFAC_O^b$, which is combined with Eqn. 3.7 to give Levich equation (Eqn. 3.14).

The addition of a second working electrode, here constructed as a ring, in close distance to the disc makes it possible to electrochemically detect the product formed at the disc. The detection is however, restricted to products that can be oxidised or reduced at a potential at which the reactants cannot. Figure 3.5 illustrates how an RRDE is hanging down in the electrolyte (in analogy to Fig. 3.1(a) and (b2)) and how the currents and reactants in the solution will flow during rotation.

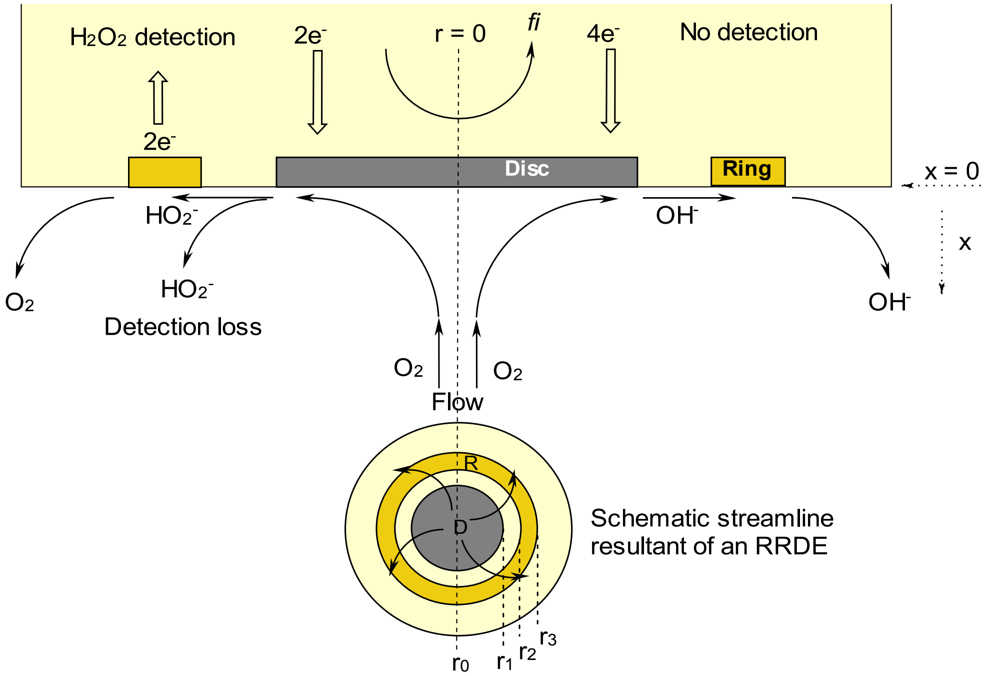

Fig. 3.5 Schematic picture of a RRDE in a cross section from the side (the top part) and from under facing the electrolyte (bottom part) and the flow of the reactants during ORR at RRDE.

The Figure above illustrates how the solution is transported in a radial and azimuthal pattern from the centre of the electrode and outwards creating a flow of liquid normal to the disc. Imagine also a stagnant layer between the radial flow and the electrode surface as described in Figure 3.4. O_2 will then diffuse through the stagnant layer and be reduced to H_2O_2 at the electrode surface. The H_2O_2 will diffuse back into the hydrodynamic region and be transported along the stagnant layer and some of H_2O_2 will diffuse in and out of the stagnant layer until it reaches the ring where it will be oxidised back to O_2. Consequently, much of the products will not come in contact with the ring but instead end up undetected in the bulk and the fraction of detected and produced species will be determined by the electrode geometry. The theoretical values for the collection efficiency (N) can be calculated using the radii (r_1, r_2 and r_3) of the disc and the ring (s.351 in [91]). N can also be determined experimentally by the use of a stable redox couple by a simple relation as given in Eqn. 3.5 which, if the electrode geometry is correct and the product is stable, is independent of rotation.

$$N = i_r/i_d \qquad (3.8)$$

A standard procedure is to use hexacyanoferrate ($Fe(III)(CN)_6^{3-}$), which is reduced in a one electron reduction process at the disc, N is then directly related to the amount of $Fe(II)(CN)_6^{4-}$ that is oxidised at the ring. In a more complex system such as the ORR the disc current comes from either a $2e^-$ (H_2O_2) or a $4e^-$ reduction (H_2O) or usually both but we can only detect H_2O_2 (Eqn. 2.5-12, Fig. 2.5). The disc current and the ring current for the ORR are therefore

$$i_d = i_{H2O} + i_{H2O2} \qquad (3.9) \qquad \text{and} \qquad i_r = i_{H2O2}N^{-1} \qquad (3.10)$$

The number of reduced O_2 molecules that end up as H_2O_2 can also be calculated. The molar fraction of X_{H2O2} can be calculated from the molar flux rate of O_2 and H_2O_2. The molar fraction can be written as

$$n_{O2(4e-)} = i_{H2O}/4F \text{ and } n_{O2(2e-)} = i_{H2O2}/2F \qquad (3.11)$$

and the molar fraction can be calculated from the disc and ring currents [94].

$$X_{H2O2} = n_{O2(2e^-)}/(\,n_{O2(2e^-)} + n_{O2(4e^-)}) = (2i_r/N)/(i_d + i_r/N) \qquad (3.12)$$

Equation 3.12 can also be rearranged to express the number of electrons involved in the reduction per O_2 molecule.

$$n(e^-) = 4 - 2((2i_r/N)/(i_d + i_r/N)) \qquad (3.13)$$

The advantage with the RDE compared with most other convective electrode systems is that both the hydrodynamic and convective-diffusion equations have been rigorously solved for the steady state of this system. The geometries of a RDE offers a well-defined determination of the velocity profile which then can be used in the general Nernst-Planck equation for mass transfer. Excess of supporting electrolyte should always be used, which eliminates the migration term and simplifies the mathematical treatment. The motion of the solution is described by three vectors; normal, radial and azimuthal to the surface (the resulting streamline vectors are shown in Fig. 3.5), which need to be implemented in the Nernst-Planck equation to generate a convective-diffusion equation for the specified convective system. The RDE must however, fulfil certain geometrical rules for the necessary simplification of the convective-diffusion equation that is the basis for the theoretical treatment of these electrode setups. The electrode need to be completely symmetrical about the centre of the disc and the radius of the disc need to be small compared to the whole electrode including the insulating layer.

After some mathematical treatment of the convective-diffusive equation an expression that relates the current to flow-rates, rotations rates (ω), kinematic viscosity (ν) and electrode dimension can be obtained, referred to as the Levich equation.

$$i_{l,c} = 0.62nFAD_O^{2/3}\omega^{1/2}\nu^{-1/6}c_O^{\,b} \qquad (3.14)$$

The Levich equation applies only to the completely mass-transfer-limited conditions, in other words it is valid only at the steady-state limiting current plateau where the concentration of reactants near the electrode surface is zero (region i_l in Fig. 3.3). Since the frequency of rotation (ω) is controlled and its impact on the system is well defined in the convective-diffusion equation all other parameters can readily be obtained from a Levich plot (i_l vs. $\omega^{1/2}$).

For an IRET (e.g. the ORR) where the electrode kinetics are slow a potential window will be available for the analysis of the rate constant between the $E^{o\prime}$ of the reaction and the potential just before the current is completely diffusion controlled (region i_k+i_l in Fig. 3.3). An expression has been formulated to take into account also the kinetic current at low overpotentials, the Koutecký-Levich (K-L) equation.

$$\frac{1}{i}=\frac{1}{i_k}+\frac{1}{i_{l,c}}=\frac{1}{i_k}+\frac{1}{0.62nFAD_O^{2/3}\omega^{1/2}\nu^{-1/6}C_O^b} \tag{3.15}$$

Where i_k is

$$i_k=nFAC^bk^0\,exp\left(-\frac{\alpha nF}{RT}(E-E^{o\prime})\right) \tag{3.16}$$

i_k represents the current flowing in the complete absence of mass-transfer effects i.e. with bulk concentrations (C^b) at the electrode surface at all times (region i_k in Fig. 3.3). This will only be the case at the very initial stage of the reaction and at more negative potentials the contribution from mass transfer will limit the current response. The mass transfer contribution is controlled by rotation but the kinetic limitations are not and the relation between mass transfer and rotation can be used to isolate the kinetically controlled current. In a theoretical approach an infinitely high rotation rate would eliminate the diffusion layer and generate bulk concentration at the electrode surface at all times. During such conditions the current would be controlled by the electrode kinetics only and the rate constant would be accessible. In the K-L plot such conditions are attained by plotting the inverse of the current at a certain potential against the inverse of frequency of rotation (i^{-1} vs. $\omega^{-½}$) and extrapolate them to infinite rotation. When currents from the diffusion limiting plateau are used the extrapolation of the straight line should go through origin if the system fulfils the geometrical conditions given for an RDE and may be used as test of the system. If currents from the mixed region (i_k+i_l in Fig. 3.3) are extrapolated to infinite rotations the intercept will give the kinetic current at a specific potential as C close to the electrode is assumed to be equal to C^b. The lines of a K-L plot should be linear and have the same slope independent of the potential since k^0 should not depend on rotation at any potential. The intercept of i_k^{-1} will vary with potential in accordance with Eqn. 3.16 and by plotting the kinetic current as a function of the potential, the rate constant at the formal potential can be obtained.

3.1.4 Pulse Plating

Various methods are used for electrodeposition in a large spectrum of applications, both in production and in research. Electroplated iron objects used in various constructions are commonly plated by zinc or nickel-zinc for corrosion protection and for such applications dc-plating is used since it is a relatively uncomplicated method. For smaller objects for which highly specified properties are needed pulse plaiting are sometimes used instead. It was the electronic industry that drove the development of this technique already in the 1960th, in their search for new methods that could provide very thin porous free gold surfaces with high adhesion to semiconducting wafers [95]. To control the surface in a *DC* plating there is only one physical parameter to adjust, the current density, and it is often necessary to use different additives to be able to tune the structure and properties of the deposit in a desired way. In pulse plating (*pp*) however, there are three physical parameters to model the properties of the deposit, which can be used to generate new characteristics of a plated surface as well as to reduce the need of additives [96-97]. The three physical variables are the current density during the pulse (i_{pp}), the time the cathodic current is turned on (t_{on}) and the time the current is turned off (t_{off}), or if t_{off} is replaced by an anodic current in pulse reverse plating (PRP, not considered further here). In an overview of the field Landolt and Marlot presented an informative table of the effects of pulse plating onto the deposited structure [96].

Table 3.1. Possible effects of pulse plating on deposite structure [96]

Time interval	Conditions that differ from *DC* plating	Phenomena affected
t_{on}	Double layer charging Overvoltage Concentration profile near electrode Adsorption (ions, additives, hydrogen)	Nucleation rate Growth mechanism (e.g. dendrites) Electrode reaction mechanism Codeposition rate (H, alloy elements) Additive reactions
t_{off}	Double layer discharge Potential relaxation Concentration profile relaxation Desorption (additives, ions, hydrogen)	Surface diffusion Surface recrystallisation Corrosion, displacement reactions, Passivation Hydrogen diffusion

Extensive theories have been developed such as the description of mass transport of depositing metals in a stagnant diffusion layer a hundred years ago [98] to the more pulse plating specific theories and concepts. Cheh [99] introduced the concept of pulse limiting current (j_{ppl}) and simplified the calculations for RDEs [99-100]. Approximate solutions from Cheh showed that for very short pulses the limiting j_{ppl} could be much larger than the steady state limiting current (j_l) due to the steeper concentration gradient created in the initial moment of an applied current. Ibl [101] presented a simple linearised model for the estimation of the pulse limiting current in which the duplex diffusion layer was introduced. This model was later further developed and experimentally confirmed [102]. The different models can be useful tools for the understanding of how the applied current is distributed in the electric interface and how the solution components are organised during a pulse experiment.

The main advantage of pulse plating is that a much higher current density can be used without massive H_2 evolution and a resulting pH change, which influences the deposition. The higher current density can alter the alloy composition and structure as well as it gives a completely different morphology compared to ordinary *DC* plating under the same chemical conditions.

A few commonly used equations in pulse plating papers (also used in this work) will be given and explained in a descriptive way.

The pulse lengths can vary from μs to s and the relation between t_{on} and t_{off} is generally described as a duty cycle (γ).

$$\gamma = \frac{t_{on}}{t_{on} + t_{off}} \tag{3.17}$$

The average pulse current density (i_m) is then given by $i_{pp}\gamma$, which corresponds to the plating rate given in *DC* plating at the same current density. It can be emphasised that the overall (integrating the current over the pulse period (t_{on}+t_{off})) plating rate for pulse plating is the same or lower than in a *DC* deposition [103].

It is important to consider some basic limits of the pulse time, the total current of a pulse consists of two parts, the capacitive and the Faradic currents ($i_T = i_C + i_F$). The charging of the double layer will consume some of the total current delivered to the system during t_{on} but the same amount of charge will be given back to the system during t_{off} as the double layer discharges. If the current density is high and t_{on} and t_{off} is short enough, the pulsed Faradic current will take the shape of a *DC* current. This can be calculated exactly, but a simple check can be made by utilising the following relation for a typical galvanic bath (($CuSO_4$) with $j_0 = 5$ mAcm^{-2}, $C = 50$ µFcm^{-2}, 20 ºC , and $\alpha = 0.5$) [101, 104].

$$t_{on} = 17/j_{pp} \tag{3.18}$$

$$t_{off} = 120/j_{pp} \tag{3.19}$$

Due to the frequency of current pulses the distribution of ions in the diffusion layer may not look exactly the same as during a constant current experiment. Ibl [101] proposed a diffusion layer consisting of two parts, one inner pulsating layer, where the concentration gradient constantly changes between the t_{on} and t_{off} pulses and an outer layer whose gradient is established after a few pulses and then remains constant through the whole series of pulses.

When the concentration of reactants is zero near the surface the current can be described in terms of limiting pulse current density (j_{ppl}) Eqn. 3.20 [96, 102]. Higher current densities from this point will give mass transfer limited plating. The thickness of the pulsating diffusion layer can be calculated by Eqn. 3.22 [96, 102]. Those equations are adjusted forms of the original equations given by Ibl and verified experimentally by Datta and Landolt [102].

$$j_{ppl} = j_l \left[\frac{\delta_{pp}}{\delta} (1-\gamma) + \gamma \right]^{-1} \tag{3.20}$$

Where δ is the Nernst diffusion layer thickness (Eqn. 3.5-6) and j_l is the steady state limiting current density

$$j_l = \frac{nFDC^b}{\delta} \tag{3.21}$$

and the pulsating diffusion layer is written

$$\delta_{pp} = \left[\frac{4}{\pi} D t_{on} (1-\gamma) \right]^{1/2} \tag{3.22}$$

The theoretical thickness (d) of a plated alloy can be calculated, assuming a dense structure, by

$$d = \frac{MQ}{nFA\rho} \tag{3.23}$$

Where the molar mass (*M)* and the density (ρ) are calculated as the fraction of the species that the specific alloy consists of. The charge (*Q)* in pulse plating is the sum of the current during t_{on}.

$$Q = \sum_{+1}^{n} i_p \times t_{on} \tag{3.24}$$

Clearly these equations give some fundamental understanding of the mass transport, current distribution etc. but as the number of parameters of a pulsed system increases the predictability of the actual plating results decreases. A quick look at Table 3.1, describing all the phenomena that may occur during pulse plating, indicates that the development of a material with specific properties indeed suggests a very elaborate experimental setup to reduce the tedious work to optimize all possible parameters. Despite the above mentioned difficulties pulse plating has been and still is one of the most interesting techniques for creating new material in the field of electrochemistry.

3.1.5 Differential Electrochemical Mass Spectrometry

Electrochemical measurements such as CV and CA with direct detection of volatile species in a mass spectrometer can be made in a setup called Differential Electrochemical Mass Spectrometry (DEMS) (Fig.3.6). Then an electrochemical cell is constructed in such a way that the working electrode is placed tight on a Teflon membrane connected to a low vacuum chamber. The WE must of course be permeable for the chemicals and can either be sputtered directly on the Teflon membrane or, as in the case in paper III, consist of a fine textured net pressed towards the membrane. All volatile species in the cell, products and reactants as well as electrolyte will pass through the membrane. A typical Teflon membrane (e.g. Gore-Tex) is 50-100 μm thick and has a nominal pore width of 20 nm with a porosity of 50% [105-106]. The response time of a particular DEMS setup is largely determined by the distance that the product molecules need to be transported from the electrode surface to the pores of the membrane. For bulk electrodes such as single crystals for which the longer distance between the electrode and the membrane is compensated with thin layer flow cells, the response time can vary from 1-2 s. For sputtered membranes however, the response time may be down to 0.1 s and for the setup used in paper III the response time should be in the lower region. The products as well as the decay of the flow of reactants are measured in-situ by the mass spectrometer when the electrochemical experiment is carried out.

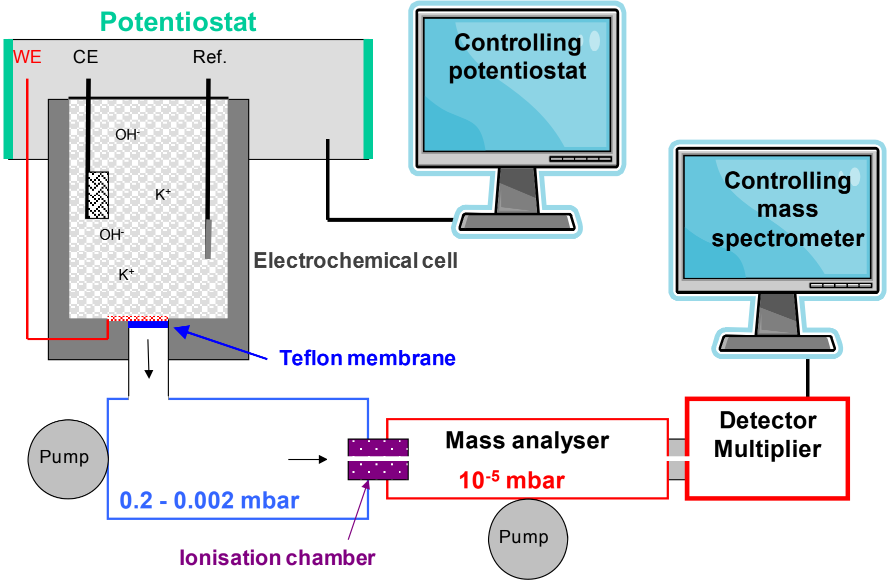

Fig. 3.6 Schematic figure of the DEMS setup used in paper III.

3.2 Characterisation techniques

3.2.1 AFM

Atomic force microscopy (AFM) [107] utilises a physical probe that is scanned over a sample surface to generate a 3D image with a resolution down to 0.1 nm. A great advantage with AFM over most other surface characterisation techniques is that it can work in any environment, which also includes in-situ electrochemical measurements.

The parts of the probe that interacts with the sample surface is a sharp tip (common tip materials are Si_3N_4 and SiO_2) that can interact with the surface in several different ways such as contact mode, non-contact mode and tapping mode. When the sample approaches the tip of the probe t at first be long range electrostatic forces are formed (e.g. at 10 nm) between them and at a closer distance van der Waals forces (e.g. at 3 nm) will start to contribute as well. The tip is attached to a flexible cantilever that works as a “nanospring” whose movement is picked up by (in most cases) a laser reflection from the top of the cantilever into an array of photodiodes - this is called a force transducer. A feedback control is in addition used to maintain a set of force between the probe and the sample based on the signal from the force transducer so that the piezo electric transducers can be corrected for height differences above the sample. All movements during a sample scan are controlled by piezo electric transducers, which can be one (z-direction) or several (x-, y- and z-direction) depending on instrumentation. The force transducer, the feedback control and the z-piezo electric transducers keep the tip of the probe at a constant position and close enough distance for the cantilever to move up and down with the topography of the sample without crashing into it. The image is created by mapping the voltage applied to the z-piezo transducer that corrects for the height differences on the sample and the lateral movement is monitored by the x- and y-piezos.

The basic description given above is valid for contact mode AFM, which later was further developed to involve oscillating probes. The great advantage of oscillating probes is in the less contact or even in non-contact with the sample, which saves both the tip and the sample from being changed or damaged and also improves the signal to noise ratio. The above basic description is still valid but the probe is now oscillating while it is moving across the surface instead of being in a constant contact-force position. The oscillating modes are divided into Non-Contact/close contact mode (NC-AFM) and Intermittent Contact/Tapping mode (IC/TM-AFM) .

For the measurements presented in this thesis, tapping mode was used in which large amplitudes of the oscillations are used so that the tip is moving between direct contact with the sample and out in the zero-force regime. The tip is in periodic contact with the sample and can be damaged but the lateral forces to the tip are avoided and the signal response is not affected by contamination layers on the sample such as humidity etc. TM-AFM is somewhat simpler and quicker to handle than the more instable NC-AFM in which the small oscillations only work in the attractive force regime in which e.g. humidity can have a large impact [91, 108].

3.2.2 SEM and EDX

A Scanning electron microscope (SEM) generates a 2D image with a resolution down to 5 nm and even down towards 1 nm, which is considered to be the fundamental limit to this technique [109-110]. The images are detailed with a topographic "feeling" due to the large depth of field and shadow relief effects. However, for an accurate 3D determination of e.g. spherical objects, special stereo imaging arrangements needs to be applied in the measurement.

In SEM a beam of high energy electrons is focused on a sample but first the electron beam passes a number of lenses, raster and scan coils, which transforms the fairly wide and poorly focused electron beam into a well-controlled electron probe. Four major parameters defines how the beam interacts with the sample and the resulting resolution; the probe diameter, the probe current, the probe convergence (related to the angle of the cone of electrons focused down to the small area of the probe) and the accelerating voltage of the electron beam. When the electron beam hits the atoms in the sample, electrons, characteristic x-rays and other photons of various energies are emitted. Two types of electrons are emitted secondary and backscattered, the secondary electrons are scattered in-elastically (significant loss of the kinetic energy to the surroundings) from the sample with lower energy and generally provides the best topographic image. The backscattered electrons which are scattered elastically (the kinetic energy is conserved) from the sample are higher in energy and may provide information of the distribution of different elements in the sample.

An important inherent function in both SEM and EDX is that the information given is an average of the interaction volume including the surface and the bulk to some depth (100 nm to 5μm) depending on the energy of the electron beam and the properties of the sample. The interaction volume can be imaged as the shape of a pear directly under the electron probe and the larger the energy of the beam the larger is the volume of the pear. As follows, the lateral scatter from the "pear" may be significantly larger than the diameter of the probe. The second issue with a large "pear" is that the information about the surface is mixed with information from the bulk of the sample. For high resolution pictures (down to single nm range) the electron probe needs to be in the range of the smallest object that is to be resolved, one solution to the "pear" problem is to go down in beam energy to minimize the size of the pear (down to 100 eV or even less for high resolution SEM). The problem with a low energy beam is that the signal with useful information is masked by the background scattering and sets the limit for a useful detection.

The topographic information is given by the differences in number of trajectories of backscattered electrons and the number of secondary electrons, arising from the change of the angel between the incidence beam and the local inclination on the specimen when the probe is moved across the sample.

The surface composition is conveniently measured by energy dispersive X-ray spectroscopy (EDX or EDS) which is usually integrated in the SEM instrumentation. The electron beam excites a core electron and the core hole is refilled by an outer shell electron and the energy difference is emitted as X-ray photons highly characteristic for each atomic species.

The same electron gun is used for all different type of experiments but different detectors are used depending on the type of analysis.

3.2.3 XPS

X-ray photoelectron spectroscopy (XPS), also known as electron spectroscopy for chemical analysis (ESCA), provides a surface sensitive chemical analysis with a sampling depth below 10 nm [111]. The elemental composition, empirical formula, chemical state and electronic state of the elements in a sample of atomic number higher than two can be measured. The sample is irradiated with soft monochromatic X-rays (200-2000 eV) and the kinetic energy of the photons is transferred to the core electrons, which then are emitted and detected as photoelectrons. The energy of the core electrons is atom specific and well known and since the photons are monoenergetic the kinetic energy of the emitted core-photoelectrons will act as a fingerprint of the atom. Photons may penetrate 1-10 µm into a sample but the free mean path for electrons in a solid is very short and only photoelectrons without energy loss to the surrounding environment are useful, the sampling depth is typically between 20-100 Å. The detection will be in the means of number of electrons that escape and their kinetic energy (E_{kin}), which are given as:

$$E_{kin} = hv - E_{BE} - E_W \tag{3.25}$$

where hv is the energy of the photons, E_{BE} the binding energy between the core level electron and the core and E_W is the work function of the solid as the electron leaves surface for the detector. Generally the XPS spectra show the number of electrons detected, often in a time or energetic interval versus the binding energy. XPS is due to its surface sensitivity an important technique in the study of surface oxides and hydroxides and it was used in the study of oxide layers on Ni and NiZn electrodes in paper I.

3.2.4 XRD

In x-ray diffraction, lattice constants can be measured in a crystalline material (long range order necessary) by the use of x-rays of similar wavelength as the separation of the planes in the lattice that is to be diffracted. The relation between the wavelength of the x-rays and the lattice planes of a crystal was formulated by W. L. Bragg in Braggs Law, where n is an integer, λ is the wave length of the x-rays and d is the spacing between the planes and θ is the angle between the incident x-rays and the lattice plane.

$$n\lambda = 2d\sin\theta \tag{3.26}$$

Indeed it is most often far more complicated than this but it starts with the Bragg equation.

A number of X-ray diffraction methods have been developed over the years and of these methods two have been used in this thesis for two different types of samples, powder and thin films. Powder diffraction is a method where the sample should be made into a reasonably homogeneously sized powder (0.1 μm < particle size > 40 μm) by e.g. mortaring. The idea is that every crystal orientations in the powder are equally represented and a few of them will be oriented to give Bragg reflections.

A powder diffractogram will have 2θ (or scattering vector q) on the x-axis and intensity on y-axis. The peak position gives the dimension of the elementary unit cell as the peak is determined by the d-spacing of the lattice planes which in turn depend on the unit cell. The peak intensity may reveal the content of the elementary unit cell as it is caused by the crystallographic structure, the positions of the atoms within the elementary cell and their thermal vibration. These parameters will generate a finger print that readily can be compared with known structures. The width and shape of the peak may give information of properties besides crystal structure such as particle size in nano materials and stresses in the samples.

Grazing incidence x-ray diffraction is typically used for thin layers that differ from the bulk in species or structure. X-rays has a large penetration depth into any matter and a "normal" diffraction setup will generate structural information from far into the bulk of the material and a thin layer will drown in the scatter from the bulk. The unwanted interference from the bulk material is avoided by keeping the angle between the beam and the sample constant but very low (typically between 0.3 and 3^o) while the detector is moved in array over the sample, called grazing incident diffraction (GID). As a consequence of the low angle the main x-ray penetration will be almost parallel to the surface layer and by that increase, the signal from the film enough for a conventional phase identification to be done. With the GID method films down to nm thickness can be resolved and depth profiles from layered samples can be obtained without significant interference from the bulk by changing the incident angle.

3.2.5 XAFS

Overview

The x-ray absorption fine structure (XAFS) technique offers detailed information of an x-ray absorbing atom and its surrounding neighbours by photoelectron excitation from core level orbitals. XAFS is the modulation of an atom's x-ray absorption probability depending on the chemical and physical state of that atom and is usually divided into two regimes: x-ray absorption near-edge structure (XANES) and extended x-ray absorption fine-structure spectroscopy (EXAFS). The XANES region is from the lower part of the XAFS spectra from which element specific information of the oxidation state and coordination chemistry can be extracted. The XANES signal is larger than the EXAFS signal and can be performed at lower sample concentrations and demands less optimal sample conditions. A full theoretical treatment of the XANES signal is however very difficult and it is generally more qualitatively described. XANES data can often be used as an easy excess of fingerprints of the species involved and its symmetry, phases and oxidation states, but exact and reliable descriptions of all physical and chemical features are still difficult to gain. The upper wider EXAFS region gives information about the neighbouring species of the absorbing atoms such as bond length, coordination number and information about local structure in a non-crystalline or short range ordered sample, that very few (if any) other technique can offer. The theory of the EXAFS is relatively well understood compared to XANES and will be treated in a general description in the next section.

One of the main drawbacks of the XAFS technique is that only a synchrotron source can produce the high flux of monochromatic x-rays needed. With a high flux of x-rays it is also possible to perform experiments on very dilute samples and on samples in solution in e.g. in-situ electrochemical experiments, which is not accessible by an “in-house” laboratory x-ray equipment.

Description of the origin of the XAFS data and the EXAFS function

For the x-ray absorption the x-rays need to be slightly higher in energy than the binding energy of a specific core electron to be able to remove it from its quantum level, the excess energy is ejected with a photoelectron from the atom out in the continuum (the conduction band of a metal), where it then can be backscattered from a neighbouring atom (Fig.3.7).

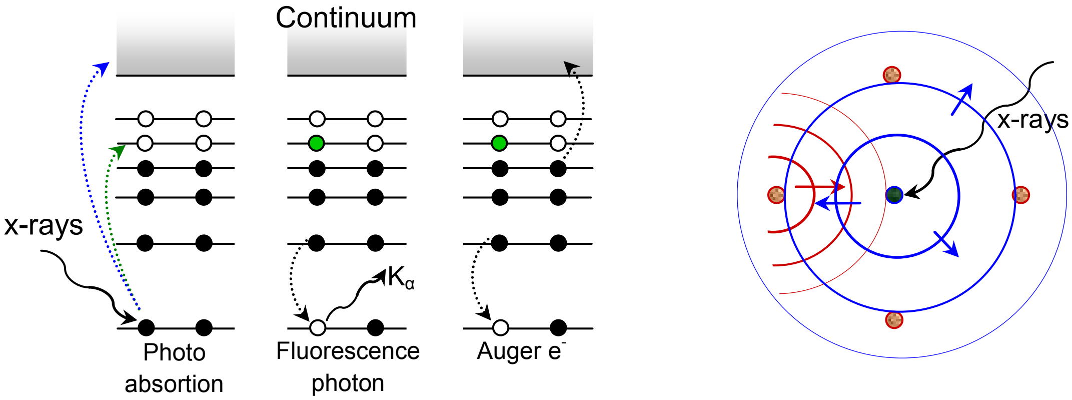

Fig. 3.7 Schematic figure of, (left) photo absorption of a core electron with a photoelectron emitted out in the continuum or excited within the atom and the release of a fluorescence photon or an Auger electron. (right) The outgoing photoelectron wave (blue rings) that are backscattered (red rings) by neighbouring atoms before it return to the absorbing atom.

It can be added to Figure 3.7 that when the photons from the x-rays hits the sample it is only strongly bond electrons that can absorb the photon and be emitted as photoelectrons, the “free” electrons can also absorb but they only emit another photon.

The difference in intensity between the incoming and the detected x-rays is referred to as the absorption coefficient μ and can be measured in transmission or fluorescence mode as schematically shown in Figure 3.8.

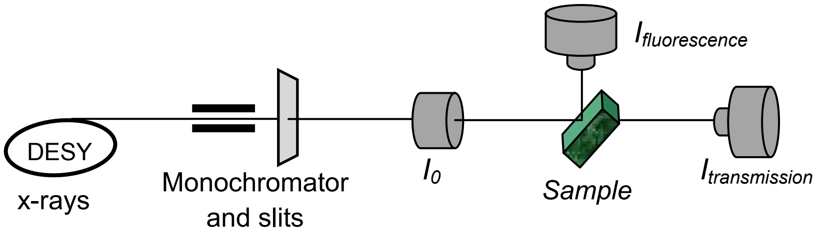

Fig. 3.8 Schematic figure of an XAFS setup with synchrotron x-rays and detection in transmission and fluorescence mode. I_0, I_t and I_f refers to the different x-ray detectors.

The difference in intensity related to the absorption coefficient μ follows Beer’s law

$$I_t = I_0 e^{-\mu l} \tag{3.27}$$

where I_0 is the incoming x-ray intensity, I_t the intensity transmitted through the sample and l is the thickness of the sample. The absorption spectra will clearly show the atom specific absorption edges of the excited core electrons as shown in Figure 3.9.

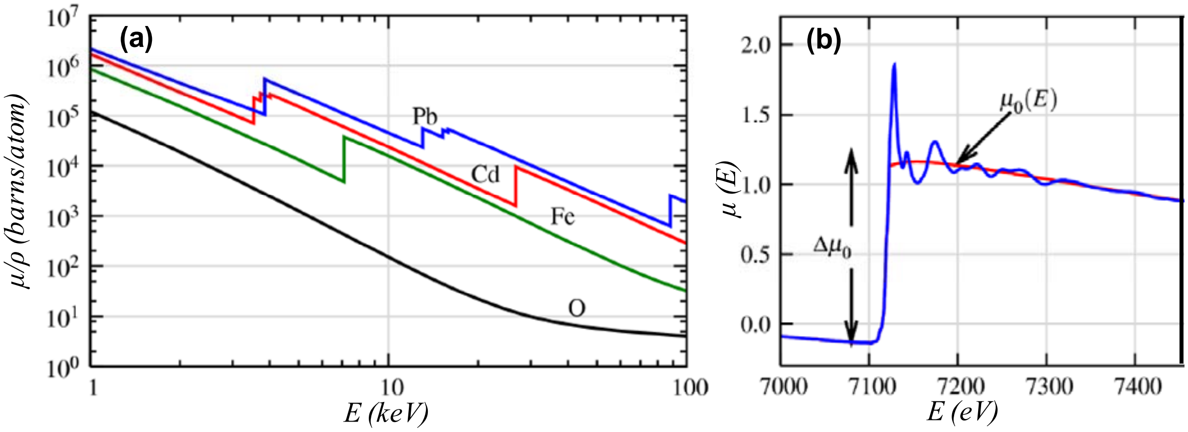

Fig. 3.9 (**a**) Absorption spectra showing photoelectron excitations from core electrons. (**b**) Magnification of one absorption edge showing the $\mu_0(E)$ for the single atom (reference spectra, red) and the spectra of the same atom with neighbouring atoms causing oscillations (blue). Reprinted by permission [112].

The absorption coefficient μ is a function of energy and a generally accepted approximation for μ/ρ is written in Eqn. 3.28, in which ρ is the sample density, A the atomic mass and Z the atomic number and E the x-ray energy [113].

$$\frac{\mu}{\rho} = constN_a \frac{Z}{A}\left(\frac{Z}{E}\right)^3 \qquad \text{or} \qquad \mu \approx \frac{\rho Z^4}{AE^3} \tag{3.28}$$

As can be seen in Eqn. 3.28 μ depends strongly on the x-ray energy and atomic number and can be correlated to the photoelectron emission corresponding to the different characteristic core level energies (K, L, ...) of the atom (Fig. 3.9). This bound for good contrast between different materials of nearly any thickness and concentration. In an XAFS measurement it is the oscillating intensity of μ near and just above the absorption edges that are used to extract the information of the state and the surroundings of an atom.

The energy dependence of the absorption coefficient $\mu(E)$ can be measured in transmission mode or in x-ray fluorescence mode (or Auger emission), where I_f is the monitored intensity of a fluorescence line or electron emission proportional to the x-ray absorption.

$$\mu(E)l = \log(I_0 / I_t) \quad (3.29) \qquad\qquad \mu(E) \propto I_f / I_0 \quad (3.30)$$

An XAFS spectra can, as mentioned in the overview, be divide into two regions, during and just after the first large rise of the edge ($\Delta\mu$) which occurs at a certain energy characteristic for the core electron chosen in the sample named XANES (Fig. 3.9-10). The second region contains the oscillations in $\mu(E)$ that follows the sharp rise and is the part that contains the EXAFS information, the XANES region is usually within 30 eV of the absorption edge and the rest of the spectra belongs to the EXAFS region.

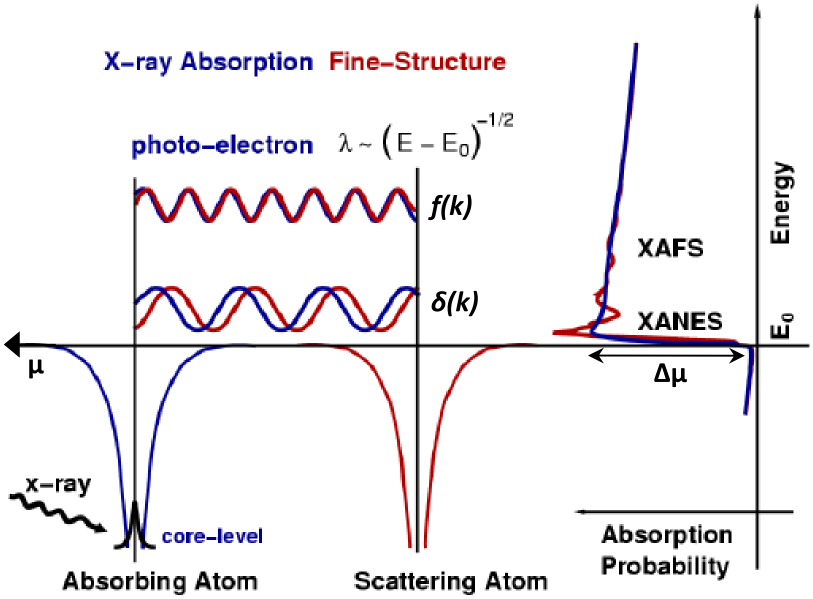

Fig. 3.10 This figure capture the essence of EXAFS, the blue curves represent a single absorbing atom and the red curves when the atom is affected by a neighbour. The left part of the figure represents one absorption edge of a core electron and the right part the wave and the amplitude of the outgoing and back-scattered photoelectron. Relate to Fig. 3.7. Reprinted by permission [112].

The energy dependent oscillation in $\mu(E)$ is defined in the EXAFS fine structure function $\chi(E)$

$$\chi(E)=\frac{\mu(E)-\mu_0(E)}{\Delta\mu_0(E)} \tag{3.31}$$

where $\mu_0(E)$ is a smooth background function equivalent to absorption of an isolated atom. Since the information in EXAFS is in the oscillation of the photoelectron wave emitted from the sample the energy of the x-rays are often converted into an expression for the wave number of the photoelectron itself k (distance^{-1}), defined as

$$k=\sqrt{\frac{2m(E-E_0)}{\hbar^2}} \tag{3.32}$$

where m is the mass of an electron $\hbar$ is the reduced Planck constant.
The primary quantity for EXAFS, describing the oscillation $\chi(k)$, decays quite rapidly and is often multiplied by some power of k (often k^2, k^3). This signal can then be modeled in the EXAFS equation (Eqn. 3.33) [112-113] which is the basis in the conversion of an oscillating signal from an ejected photoelectron to relevant physical properties of a sample.

$$\chi(E)=\sum_j \frac{N_j S_0^2 f_j(k) e^{-2k^2\sigma_j^2} e^{-\frac{2R_j}{\lambda(k)}}}{kR_j^2} sin\left[2kR_j+\delta_j(k)\right] \tag{3.33}$$

Where $f(k)$ and $\delta(k)$ are scattering properties the neighbouring atoms (amplitude and phase shift respectively, Fig. 3.10), N is the number of neighbouring atoms, R is the distance to the neighbouring atom and σ^2 is the disorder in the neighbour distance. In a real system the time frame of the mean free path of the photoelectron before it scatters inelastically and before the core hole of the absorbing atom is filled, is limited. The mean-free-path (λ) is typically 5 to 30 Å and depends on k in the function $exp(-2R/\lambda(k)$. The amplitude reduction term (S_0^2) corrects for the relaxation of all the other electrons in the absorbing atom to the hole in the core level, this value is standard values received from data from a well known structures.

The EXAFS equation is now ready to be used and it is “only” the scattering properties $f(k)$ and $\delta(k)$ that needs to be calculated. When the physical measurement has been done both data reduction and data modeling have to be performed for extraction of useful information. This work has apparently been known as “nasty” in the past of the EXAFS history but can since some decade be calculated quite conveniently by computer programs such as FEFF, GNXAS and EXCURVE [114]. This section intended to give the reader a brief introduction to the origin of the EXAFS data and is not going into detail of the data reduction and modeling. It can however be added that in most cases the weight EXAFS $\chi(k)$ is Fourier Transformed to $\chi(R)$ and the x-axel of an XAFS plot changes from k /Å^{-1} to R /Å.

The majority of the fundamental explanations of XAFS has been gathered from a unpublished documents by Matthew Newville [112] and Hitoshi Abe [115] which are recommend for a pedagogic explanation of XAFS. However, well referenced literature has been used as well in [113, 116].

4 Pulse Plated Ni and NiZn alloys

The background of nickel and the reactions studied in this chapter has been described in Section 2 and its importance has been elucidated. The first part of Chapter 4 will describe the fabrication of the different pulse plated alloys used in paper I-III and show how the alloys evolve with the treatment steps. This part will be slightly more extensive than what has been presented in the papers. In the second part the characterisation of both the surface layer and the bulk of the alloys will be presented. Finally, in the third part the proton and oxygen reduction ability of the alloys will be presented.

4.1 Fabrication of electrodes by pulse plating

4.1.1 General

In paper I-III three different types of pulse plated electrodes (Fig. 3.1) were used in three different types of measurements; rotating electrode voltammetry, DEMS and XAFS. The goal was to make the plated material as similar as possible despite the different geometries of the substrates. The pulse plating parameters and bath composition for the plated nickel (Ni(pp)) and nickel-zinc (NiZn) (alloy b10) coatings were first determined for a RDE in hard-coating experiments by Ahmed [117]. Those coatings were later proven to be interesting catalysts for O_2 reduction to H_2O_2 and were used in all three papers, plus some variations of pulse parameters for NiZn in paper II. The substrate material used in all three studies was platinum, with the exception of a complementary measurement in paper II (Section 4.3). The first hard-coating platings made by Ahmed were however on steel substrates, but an investigation by Alfantazi et al. [118] showed that only minor changes in the structure were induced by the substrate. The catalytic properties of the electrodes were investigated for the proton reduction reaction (PRR), the ORR and the propenol oxidation/OER (Chapter 5). Galvanic plating was used as it is the method of choice in most industrial applications and the first development of the NiZn alloys where made for hard-coating applications [1]. In this thesis the catalytic properties of the pulse plated NiZn alloy were investigated as a possible cathode material for co-generation of energy and chemicals in collaboration with Johnson Matthey, within the European research program CLETEPEG.

4.1.2 Model system for plating of the rotating ring disc electrodes

The plating parameters used for the galvanic square wave pulse plating of the RDEs as well as the resulting maximum plating potentials are shown in Table 4.1. The RDEs plated with the parameters in Table 4.1 were used in the study of oxygen reduction (Section 4.4) and propenol oxidation (Section 5).

Table 4.1 Plating bath and parameters for galvanic square wave pulse plating.

	Chemicals	C mol L^{-1}	ω rpm	t_{on} s	t_{off} s	i_p mA cm^{-2}	$E_{max}{}^{a}$ V	$E_{max}{}^{b}$ V
Ni(pp)	$NiSO_4 \cdot 6H_2O$ Na_2SO_4	0.30 1.2	200	0.66	7	28.4	-1.2	-1.1
Zn	$ZnSO_4 \cdot 7H_2O$ Na_2SO_4	0.28 1.2	1600	0.66	7	187.5	-1.7	-1.4
NiZn (10b)	$NiSO_4 \cdot 6H_2O$ $ZnSO_4 \cdot 7H_2O$ Na_2SO_4	0.30 0.028 1.2	1600	0.66	7	187.5	-1.6	-1.3

pH = 2.8, 40 pulse cycles for the standard RDEs, ω is the rotation rate of the RDEs,
[a]*resulting potential,* [b]*IR (23Ω) compensated resulting potential*

Immediately after the last pulse a potential sweep from -0.4 to 0.5 V was performed on the Ni and NiZn electrodes, referred to as "stripping". Thereafter both Ni and NiZn electrodes where cycled 44 times between 0.05 and -0.9 V (vs. Ag/AgCl) in O_2 saturated 0.1 M KOH at 10 mVs^{-1}. For use in oxidation reactions the electrodes were cycled 40 times between H_2 and O_2 evolution to attend a stable response from the $Ni(OH)_2$/NiOOH redox couple. For a more detailed experimental description the reader is referred to paper I-II.

4.1.3 Different electrode geometries

The mesh electrodes used in paper III (Fig. 3.1e) were made to fit in the DEMS setup and its area was approximated to 3.5±0.5 cm^{-2} measured by the charge associated with PtO reduction [119]. The plating conditions listed in Table 4.1 were followed as far as possible. If however the same current density was used for the mesh electrode as for the RDE a higher maximum plating potential was received with massive H_2 evolution and $Ni(OH)_2$ precipitation. The current density was therefore adjusted so that the maximum cathodic potential corresponded to the ones received from the RDEs. The second experimental parameter that differed was the rotation, obviously the mesh electrode could not be rotated instead the solution was stirred.

The third type of electrode (Fig. 3.1(d)) was made to fit the setup of the XAFS instrument at the Hasylab facility at the Deutsches Electronen-Synchrotron (DESY). For the XAFS measurements thicker layers than those received from the "standard" 40 pulses for RDEs were needed and the number of pulses were therefore increased (Table 4.2). The current density had to be adjusted to control the value of the resulting maximum potential during t_{on}, as previously described for the mesh electrodes.

Table 4.2 Pulse plating parameters for XAFS specific electrodes

Electrode notation Foil	 RDE	t_{on}/s	t_{off}/s	No. of pulses	$[Zn^{2+}]$ = 0.030 M^{a}	$[Zn^{2+}]$ = 0.015 M^{b}
A'	a'	0.24	2	684	A'10	-
A	a	0.33	3.5	400	A10	A5
B	b	0.66	7	200	B10	B5
C	c	1.30	14	100	C10	C5

[a,b] *For A/a, A'/a', B/b and C/c the electrolyte also contains* $[Ni^{2+}]$*=0.30 M and* $[Na_2SO_4]$*=1.2 M, pH = 2.8*

A second set of RDEs used for proton reduction (Section 4.3) were plated with the pulse and bath parameters listed in Table 4.2, but with 40 pulses and at 200 and 1600 rpm for Ni and NiZn, respectively. These electrodes were not cycled in 0.1 M KOH as was the case for the electrodes used for oxygen reduction (Table 4.1), since the PRR was studied in acid media where the hydroxide is less stable. The RDEs used for the PRR study are named a10, b5 and so on in analogy with the foil electrodes, which are named A10, B5 etc.

The major concern with the three different electrode fabrications was the difference in surface roughness of the substrate between polished Pt RDEs and the unpolished the Pt-mesh and Pt-foil. The second concern was the difference between the perfectly controlled hydrodynamic movement of a RDE and the less well defined hydrodynamic properties of the fluid induced by the magnetic stirrer. Comparable characterisation of the three electrode types where made by CV, SEM and EDX and are presented in Section 4.2.

4.1.4 Pulse analysis

In galvanic plating the applied cathodic current is forced through the system and if the reaction with the lowest overpotential is not fast enough to receive all the charge the potential will increase until the potential for the next reaction is reached and so on, until all the charge has been "delivered". Since the reduction of Ni is fairly slow [120-121] various amounts of hydrogen evolution occurred at t_{on} for both Ni and NiZn but in a larger amount for the NiZn plating due to the higher current density used. The charge applied was however not high enough to change the pH within the diffusion layer of a stationary electrode and with rotation the effect will be even lower [121]. Alloys plated under these conditions were silver-bronze coloured and hardly visible (Fig. 4.7), but if the current density was further increased the alloys became visibly thick and greenish in colour, which was identified as $Ni(OH)_2$. It was therefore important to keep the resulting maximum voltage between -1.5 – -1.6 V and -1.15 – -1.25 V for NiZn and Ni respectively, to avoid the chemical precipitation of $Ni(OH)_2$.

The pulsating diffusion layer (δ_{pp}) for Zn, Ni and NiZn was calculated to 23 μm (Eqn. 3.22) and the Nernst diffusion layer to 24 μm (Eqn. 3.21), meaning that t_{off} is long enough to more or less re-establish the bulk concentration outside the pulsating diffusion layer (Section 3.1.4). The electrodes were however, rotated and the stagnant layer (in where a diffusion gradient can be build up) for the Ni deposition (200 rpm) was calculated to 31 μm and 11 μm for Zn and NiZn (1600 rpm) (Eqn. 3.7). The calculated pulsating diffusion limited current density (j_{ppl}, Eqn. 3.20) for Ni is 175 $mAcm^{-2}$ and the time to reach zero concentration Ni^{2+} at the surface is 2.2 s (Sand's equation), the pulse plating of Ni can therefore be considered to be under kinetic control as the pulse used was 28 $mAcm^{-2}$. The case with Zn and NiZn is different since a higher rotation rate was used which makes the stagnant layer much smaller than the pulsating layer, the current density was however also much higher (188 $mAcm^{-2}$). The calculated diffusion limited current at 1600 rpm is as high as 370 $mAcm^{-2}$ (Eqn. 3.14) for Ni in the Ni^{2+}/Zn^{2+} plating solution but only 35 $mAcm^{-2}$ for the Zn. The reduction of Ni can therefore be assumed to be kinetically controlled during the whole pulse while the Zn quite rapidly will become diffusion controlled.

The current-on (t_{on}) part of the pulse cycle in the pulse order of 1, 2, 5 and 40 for Zn, Ni and NiZn are shown in Figure 4.1(inset). The theory for galvanostatic plating [122-124] is much less developed compared to potentiostatic plating [92] (due to the risk of having more than one reaction in same response) and it is therefore difficult to gain fundamental information about the plating behaviour from the characteristics of the plating curves. The curve from the first pulse differs significantly from the following pulses, and an AFM image (Fig. 4.8) of the electrode after one pulse in a NiZn bath shows that the plated layer grow as isolated 3D clusters and that the cluster size of only one pulse is significant. At the following pulses for both Ni and NiZn a process in the initial part of the pulse may be addressed as a nucleation process with some energetically favourable reduction states that generates a decrease in the reduction overpotential [125]. The reduction of the overpotential for Ni is visible for a short time only and hardly not at all for NiZn, since a second process appears to take over and determine the overpotential. The second process is likely to be H_2 evolution (visually confirmed) and it appears as this process is dominating the second part of the pulse. In a qualitative comparison with theories from potentiostatic plating the first pulse for both Ni and NiZn has the shape expected for single growth centres not interacting with each other, which in the second pulse takes the shape of growth centres with overlapping diffusion fields as discussed in [92]. The theories discussed in reference [92] assume chronoamperometric electro-crystallisation but similar experiments were made for cadmium deposition in [125] where the corresponding results for both chronoamperometric and chronopotentiometric measurements were shown for the same system. From [92] and [125] and the results in Figure 4.1 it may be argued that the marked difference between pulse 1 and 2 for Ni and NiZn originates from single islands of growth centres in the first pulse which grows together in the second pulse. Further support for the single growth centre of the first pulse is shown in Figure 4.8 for NiZn. The deposit is growing in 3D with free substrate around a single growth centre.

The reduction of Zn is much faster than for Ni and the plating curves indicate that a covering layer is formed after the first nucleating pulse which then increases in a fairly uniform manner. The static profile of the potential response during t_{on} shows that the Zn^{2+} reduction continues under the same energetic conditions from the 2:nd to the 40:th pulse (Fig. 4.1(a)) which supports deposition on a Zn covered surface [126].

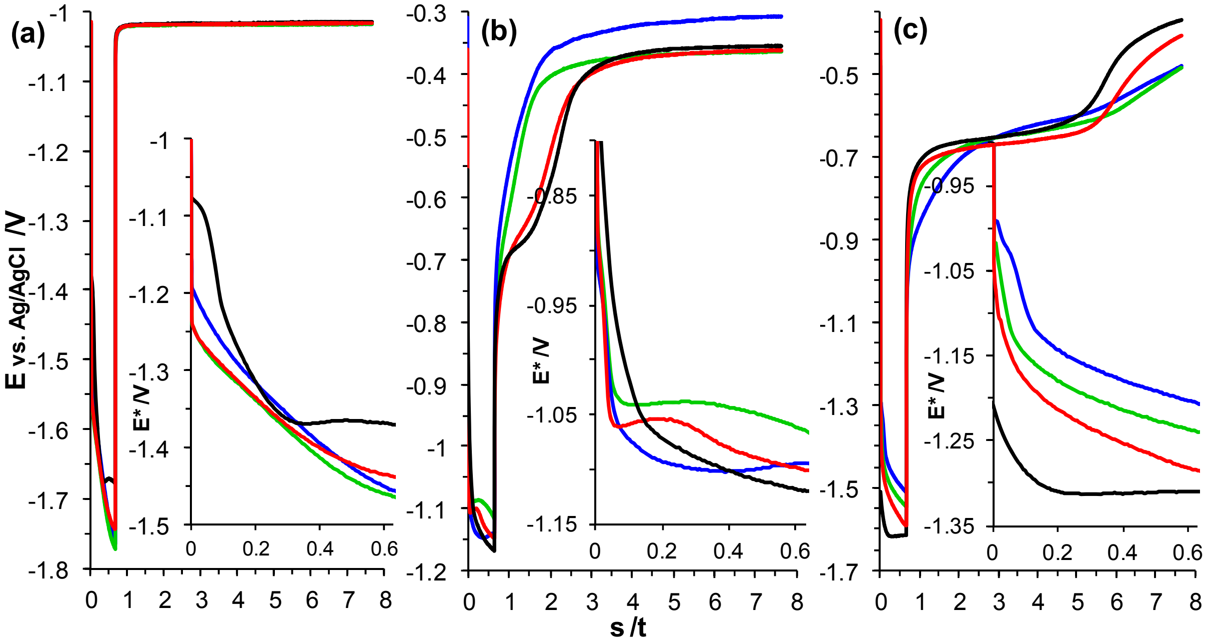

Fig. 4.1 The galvanostatic pulse cycle (t_{on}+t_{off}) shown for the RDEs pulse plated with (**a**) Zn, (**b**) Ni and (**c**) NiZn. Cycle nr: ▬ 1, ▬ 2, ▬ 5 and ▬ 40 are shown. (*Inset*) t_{on}, the potential (E*) has been compensated for the IR (23Ω) drop.

During t_{off} (i.e. at the OCP) the system strives towards an equilibrium potential between the specimens at the surface and the species in the solution. All three electrodes approach their equilibrium potential in different ways. The Zn electrode reaches a stable OCP very fast and keeps the same value from the very first cycle and this value is also very close to its E_{eq} value (-0.97 V vs. Ag/AgCl). The OCP of the Ni electrode has however a distinct plateau at -0.7 V for the first couple of cycles which after more than five cycles becomes less pronounced. The final OCP is close to -0.31 V which is 160 mV more positive than the expected E_{eq} value (-0.47 V vs. Ag/AgCl). The NiZn electrode has a plateau at the same potential as Ni but it continues for almost 5 seconds before it takes a second semi-stable OCP value. The OCP values decreases for the first 5-10 pulses and is then more or less stable. The measured and calculated OCP value for the composition of this NiZn alloy ($Ni_{80}Zn_{20}$ by EDX) is -0.48 and -0.57 V respectively. The last t_{on} and t_{off} potential values at each pulse cycle can be followed in Figure 4.2. The difference between the E_{eq} and the measured OCP for Ni and NiZn reveals that additional processes are active during t_{off}, the Zn content in the NiZn alloy do however push the OCP towards the expected potential region. The OCP for NiZn during t_{off} makes it impossible for any Zn-phases to exist whiteout a strong stabilising effect by Ni.

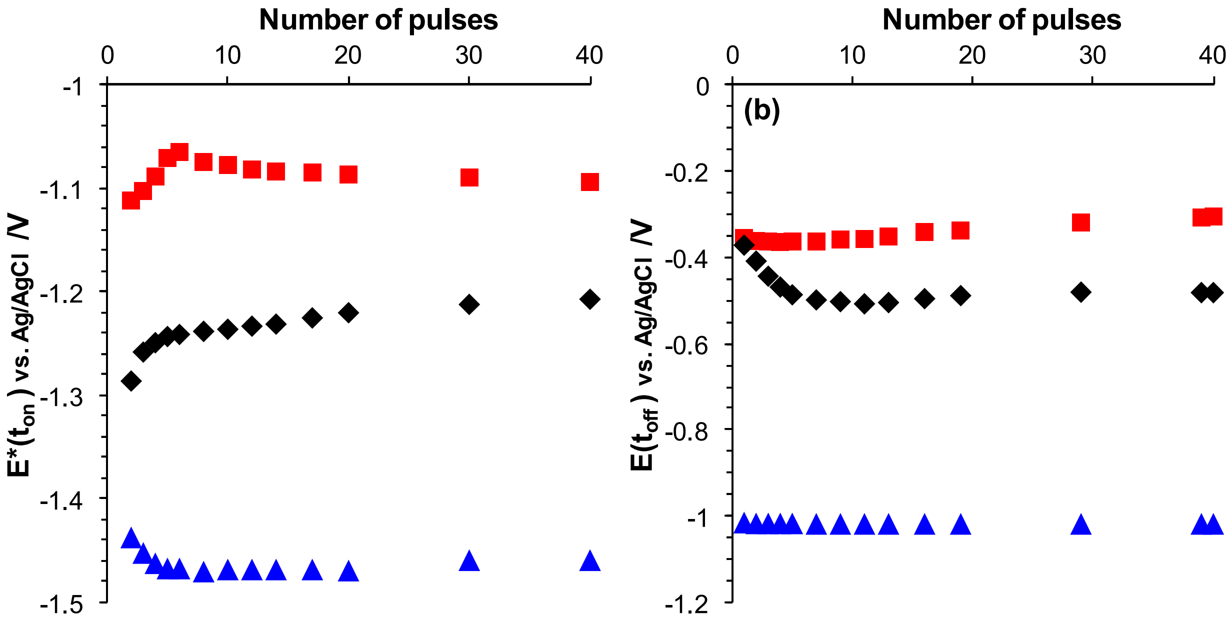

Fig. 4.2 The last potential values of the galvanostatic pulse cycles, t_{on} (left) and t_{off} (right), from the pulse plating of ■ Ni, ◆ NiZn and ▲ Zn. E*(t_{on}) has been compensated for the IR (23Ω) drop

4.1.5 Stripping analysis

The stripping sweep performed in the plating solution directly after the last pulse, to stabilise Ni and NiZn, did however generate complete stripping of the Zn electrode (Fig. 4.3(a)). The thickness of the pulse plated layers was investigated by complete stripping by a potential sweep from -0.4 to 0.4 V in 0.1 M HCl. Both electrodes that were pre-stripped in the plating solution and those without pre-stripping were completely stripped in HCl (Fig. 4.3(b)). The stabilising stripping sweep for Ni is about a tenth of the one for NiZn but the shape and peak potential of the two are exactly the same and can therefore be assumed to have the same origin, oxidation and/or dissolution of Ni. From Figure 4.3(b) it appears as the deposit of stabilised Ni to some extent was protected by the pre-stripping since more positive potentials wa needed for complete oxidation. This effect was not seen for NiZn, indicating that there is a difference in the stability of the oxides formed on Ni and NiZn in the stripping step.

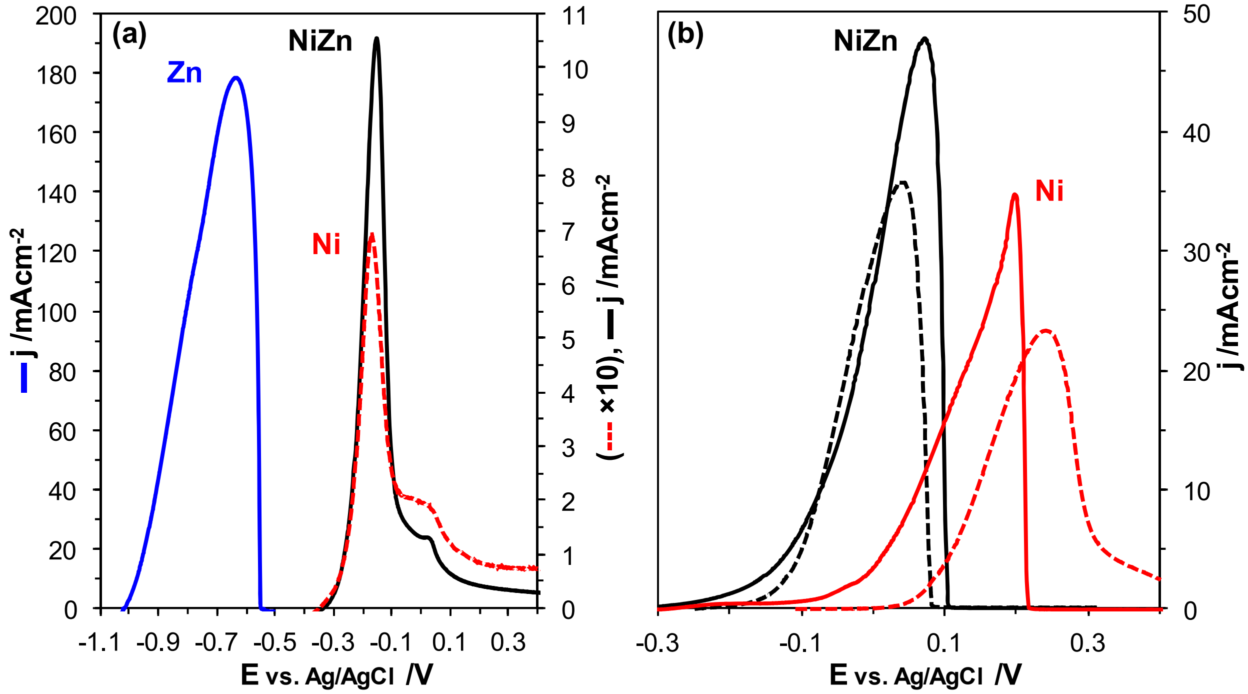

Fig. 4.3 Potential sweep stripping curves 10 mV^{-1}. (**a**) Directly after the last pulse in the plating solution ▬Zn, ---Ni (j×10) and ▬NiZn. (**b**) In 0.1 M HCl, *dashed curves* are from electrodes previously stripped in the plating solution.

By comparing the stripping results from several electrodes it could be seen that approximately 6 and 28% of the plated layers were oxidised during the stripping of Ni and NiZn, respectively. The thickness of the plated layers was calculated from the integrated charge of the stripping peaks and Eqn. 3.21, assuming a dense and smooth layer, to 2.26 µm, 120±15 nm and 197±14 nm for Zn, Ni and NiZn, respectively. The current efficiency was calculated by the use of Eqn. 3.21-22 to 96% for the Zn deposit, 51% for Ni and 11% for NiZn. For Zn this means that there was very little H_2 evolution during t_{on} or Zn(pp) dissolution during t_{off}. For Ni and especially for NiZn the current efficiency is very low, a part of the current is from H_2 evolution which is visibly larger for the NiZn electrode that is completely covered by H_2 bubbles after each t_{on} in the plating step and it is difficult to say if there is a surface accumulated Zn-phase that is dissolved during t_{off} or not.

A 20 s long OCP measurement made after the last plating pulse, ended at the same value for both Ni and NiZn (-0.35 V). The corresponding measurement after the stripping showed a larger variation but pointed at a 50 mV more positive value for NiZn (-0.20 V) than for Ni (-0.25 V).

The reason for the discrepancy between the OCP during t_{off} and the OCP measurements that followed is not clear but the more positive OCP after longer time in the solution and the stripping sweep indicates less influence from Zn and a higher degree of influence from processes other than the equilibrium between Ni and Ni^{2+}. Marshakov et al. [127] showed that a Ni rich top layer was formed on a NiZn electrode in 1 N H_2SO_4 and together with adsorbing properties of the sulphate made it impossible to judge the character of the NiZn based on the electrode potential. It has also been claimed [128] that nickel oxide/hydroxide is formed during stripping at pH = 5 and it is likely that the Zn atoms in the top layers are dissolved together with some neighbouring Ni atoms until a stable layer of nickel oxide/hydroxide has been formed. Such combined stripping and oxidation may explain the much larger stripping peak for NiZn in Figure 4.3(a) and the lack of a protected layer for the pre-stripped samples seen for Ni in Figure 4.3(b).

The redox response of $Ni(OH)_2$/NiOOH on two newly plated NiZn electrodes were compared in 0.1 M KOH, one directly from the last pulse and the other from after the stripping procedure (Fig. 4.4(a)). The stripping changed the surface in a way that the redox couple became better defined and the stability in alkaline solution increased. Important is also that the charge of the redox couple was about the same, which indicates that the real surface area is not significantly changed during the stripping procedure.

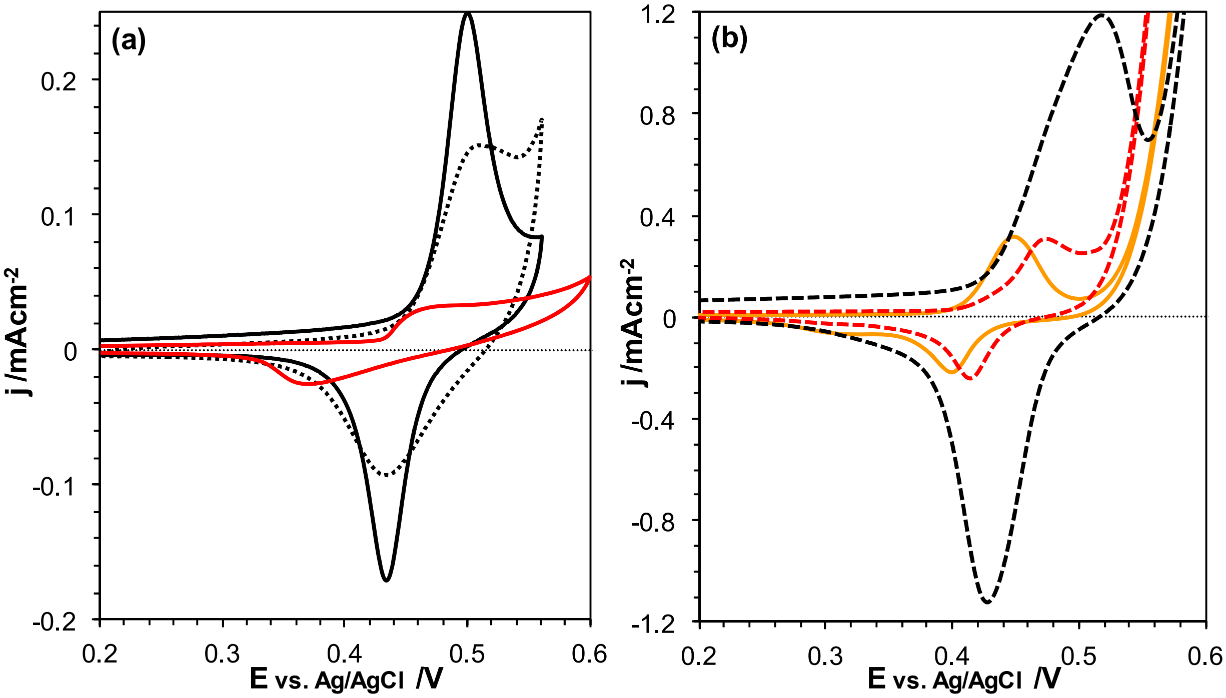

Fig. 4.4 Potential sweep curves in 0.1 M KOH, 10 mV^{-1}. (**a**) ••• NiZn directly after plating, ▬ NiZn and ▬ Ni(pp) directly after the stripping sweep in the plating solution. (**b**) After the cathodic cycling (×44) and anodic cycling (×40) in 0.1 M KOH; --- NiZn, --- Ni(pp), ▬ Ni(s).

The charge of the $Ni(OH)_2$/NiOOH redox couple has been used as a relative estimate of the active area of the Ni(pp) and NiZn electrodes and has been determined for several different electrodes and falls in the range of 3.5 to 5 times in favour of NiZn. Figure 4.4(b) shows the redox response of the fully treated electrodes which includes the cycling (×44) in the negative potential region plus the 40 cycles between H_2 and O_2 evolution for a stable redox response in 0.1 M KOH. The repetitive cycling across the redox couple increases the amount of oxidised species on the surface by several times and was used in paper III.

4.1.6 The effect of different pulse parameters

In paper II the local structure of the different NiZn alloys was investigated by XAFS and the structure differences were correlated to the PRR. Two different Zn^{2+} concentrations in the plating baths were used for three different plating time parameters as described in Table 4.2.

The first pulse and the stripping that followed on the RDEs with the plating parameters outlined in Section 4.1.3 are shown in Figure 4.5(a). The change in pulse parameters from the ones used in Table 4.1 does not change the kinetic control of the Ni^{2+} reduction, but the lower concentration of Zn^{2+} lowers the short initial part of the pulse that is kinetically controlled. The maximum plating potential also becomes a bit lower with less Zn^{2+} in the solution (compare with --- b10) and a longer pulse time increase the maximum plating potential.

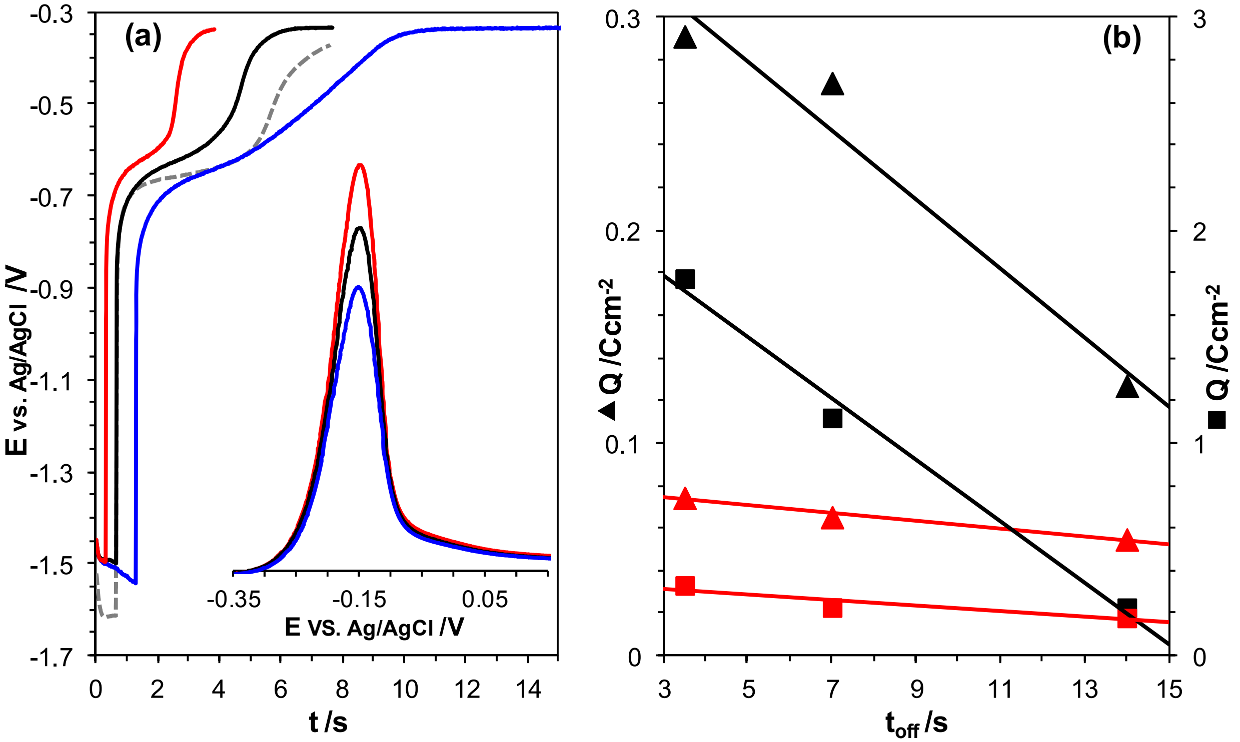

Fig. 4.5 (**a**) The first plating pulse in 5% [Zn^{2+}] at — 0.33/3.5s (a5), — 0.66/7s (b5), — 1.3/14s (c5), --- 0.66/7s (b10) pulse and the corresponding stripping peaks (inset). (**b**) The charge from the stripping peaks of the RDE at ▲5% (a-c5) and ▲10% (a-c10) [Zn^{2+}] and the charge from the stripping of the plated foils for XAFS at ■5% (A-C5) and ■10% (A-C10) [Zn^{2+}].

The time it takes for the electrodes to reach a steady OCP during t_{off} is linearly related to t_{on} during the first pulses but just as can be seen in Figure 4.1(c) for NiZn b10, the difficulty to reach a steady OCP increases with the number of pulses also for NiZn a-c5. Interesting is also that the time to a steady OCP is longer for the 10% [Zn^{2+}] electrolyte (dashed line in Fig. 4.5(a)). The stripping current decreases linearly with increasing pulse time for both concentrations but with a 10 times larger slope for the higher Zn^{2+} concentration. The same relation in stripping behaviour between the 5 and 10% [Zn^{2+}] electrolytes can be seen also for the foil electrodes even though the charge density is higher (Fig. 4.5(b)). The higher charge density for the foils is related to the larger number of pulses used and the same effect can be seen for RDEs if the number of pulses is increased. Plating and stripping of RDEs at 10% [Zn^{2+}] electrolyte also confirms that the stripping charge increases with both increasing number and shorter pulses. The results from Figure 4.5 indicate that the effect of Zn^{2+} concentration and pulse length is the same for RDEs and foil electrodes despite differences in the plating condition due to the different electrode geometries.

The EDX measurements show that with the lower Zn^{2+} concentration in the bath two to three times thicker plating is obtained. The EDX results also show that longer plating cycles give thinner layers for both plating solutions and less Zn in the alloy for the bath with high Zn^{2+} concentration. In the lower Zn^{2+} concentration the alloy composition appears to be independent of the change of pulse parameters. The EDX results indicate that the stripping charge is more related to the Zn content in the alloy as the difference in thickness between the two $[Zn^{2+}]$ electrolytes is quite similar for the different pulse times, but the slope of the charge for 5% $[Zn^{2+}]$ is almost negligible compared to the one for 10% $[Zn^{2+}]$ (Figure 4.5(b)) which is more of the trend for the Zn content in the alloy seen in Figure 4.6(b).

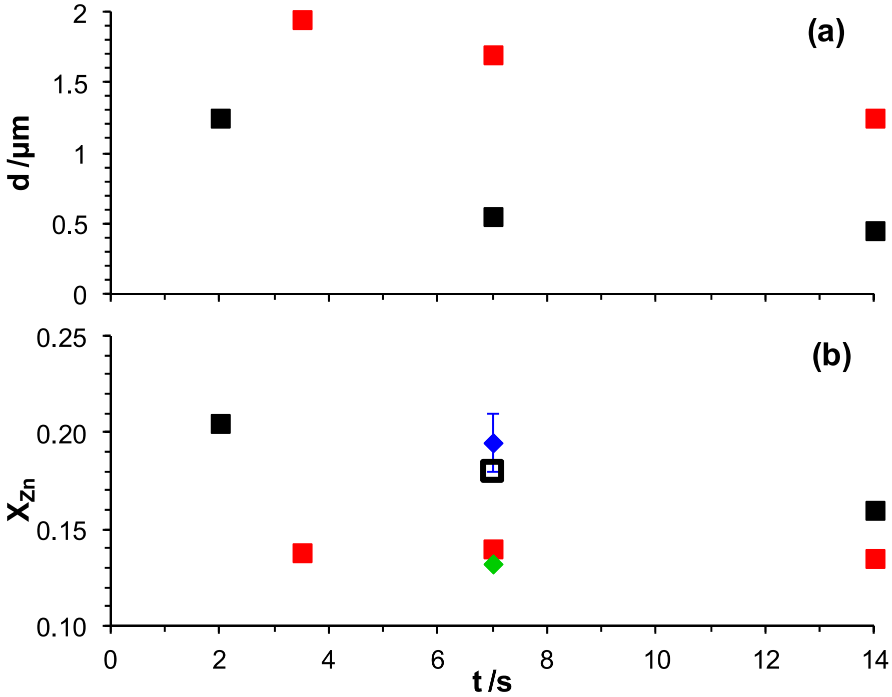

Fig. 4.6 EDX measurements on: Plated foil electrodes 🟥5% (0.015 M) and ■10% (0.030 M) $[Zn^{2+}]$ and RDEs ◆5% (a5) and ◆10% (a10). (**a**) The thickness of the plated layer. (**b**) The molar fraction of Zn in the alloy.

EDX measurements on RDEs of NiZn (a5) and (a10) indicated a substantially thicker layer from (a5) than from (a10), and the Zn concentration in the alloys was in the range of the plated foil electrodes (Fig. 4.6(b)). The composition of the alloy (a10), which is referred to as the “model system”, was measured several times at different stages such as directly after the last pulse (t_{on}), after the stripping and after the cycling (x44) and the result always showed a content of 19.5±1.5% Zn.

This may be interpreted as the longer the pulse the more material will need to be oxidised to reach equilibrium, but EDX measurement indicates that longer times gives thinner layers and less Zn which would mean more H_2 evolution during t_{on} and /or more dissolution during t_{off}. This clearly indicates that the majority of the Ni^{2+} and Zn^{2+} reduction occurs at the beginning of t_{on} and that the H_2 evolution increases at the last part of the on-pulse which is to be expected from this high current density and the general advantage with short pulses.

4.2 Morphology and local structure of the NiZn alloy

In the first part of this section images closely related to the results outlined in Section 4.1 will be shown. The second part will discuss different ways of measuring the local structure and about the results for the pulse plated alloys.

4.2.1 Morphology

The first surface analysis of these alloys was made by optical microscopy, before and after the stripping procedure. Stripping of the NiZn alloys results in a darker and more contrast rich layer even if the main morphology did not seem to change (Fig. 4.7). The same tendency was seen for Ni(pp) but the change was small and needed a computer screen to be visible.

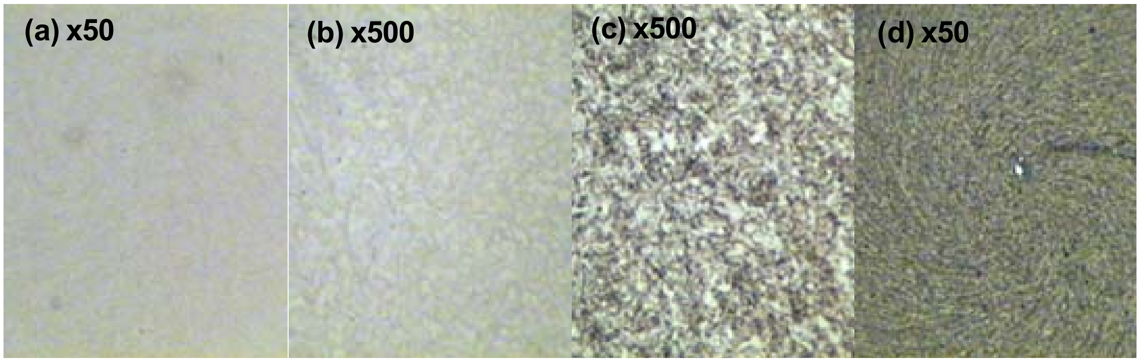

Fig. 4.7 Optical images of a NiZn alloy plated by 40 pulses, 50 and 500 times magnification are shown. (**a**) and (**b**) are from before and (**c**) and (**d**) are from after the stripping in the plating solution.

The darkening of Ni and NiZn electrodes exposed to positive potentials has been reported by several groups [127, 129-131] and one reason for the change was believed to be the roughening of the surface due to the dissolution and re-passivation that follows [132]. Rehim et al. [129] observed that the darkening occurred at the second peak (peak II in Fig. 4.3) and was referred to as Ni_3O_4 formation based on publications from the 1960th [133-134], there was however no real proof of such species. For the present investigation the most relevant observation for the NiZn alloys was made by Marshakov et al. [127]. They observed that the alloy was uniformly dissolved (except at very positive potentials) but that a black deposit was formed on the surface. The black deposit was determined by XRD to be Ni in its own phase as a result of a phase transformation in the surface layer. They stated that NiZn dissolves to form a “peculiar” layer enriched in Ni but with a NiZn crystal structure. Also Petrauskas et al. [131] recognised the black coloration of stripped NiZn alloys to be a consequence of Ni enrichments during stripping.

An AFM image of a NiZn (a10) plating after the first pulse is shown in Figure 4.8. Despite the low resolution the image shows how spherical nucleates in the 50-100 nm range grow together creating 3D agglomerates on a flat substrate. This image supports the interpretation of the profile of the t_{on} curves that the growth takes place on isolated island at the first pulse and then grows together at the coming pulses.

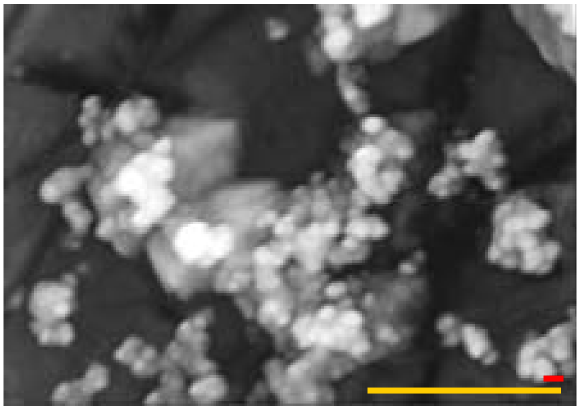

Fig. 4.8 AFM images of a first single pulse of a NiZn (a10) alloy, ruler 🟨1 µm, 🟥100 nm.

SEM images of the three different electrode types with the same NiZn deposit are shown in figure 4.9(a), (b) and (c). The surfaces of all three electrodes appears to be build up by about 60-100 nm large clusters which are especially well defined for the plated mesh electrode (b). Increased magnification of the mesh electrode (d) shows that on top of the 60-100 nm clusters new clusters are growing, which at this point has reached a size of approximately 10 nm. The AFM and SEM images indicate that the growth limit of the particles that forms the alloy during these plating conditions are between 60-100 nm as the same particle size can be seen both after the first and the last pulse. In Figure 4.10(a) and (b) the XPS analysis of pulse plated Ni and NiZn is presented. The Ni2$p_{3/2}$ signal (a) shows that there are oxidised products present on the metal surface. Deconvolution of the O1s spectra shows one feature at 529.8 eV (O) and a second at 531.5 eV (OH), which indicates that both NiO and $Ni(OH)_2$ are present on the Ni surface (Fig. 4.10(b)). For NiZn the XPS spectra in Figure 4.10 (curve ii) shows a large $Ni(OH)_2$ signal, a small Ni-metal signal and an even smaller rather indistinct NiO signal, shown as a lack of minima between the signal from $Ni(OH)_2$ and Ni. The small sholder like O signal from the O1s spectra in Figure 4.10(b) (curve ii) indicates that the indistinct NiO signal from the Ni2$p_{3/2}$ spectra is likely to be NiO. An increase of the take-off angle (30° and 45° with the respect to the sample surface) gave a signal decrease of the $Ni(OH)_2$:NiO intensity ratio, which is in accordance with a bi-layer structure with an outer hydroxide and an inner oxide phase [135-136]. Similar build-up of nickel oxide has also been shown by STM and X-ray scattering using synchrotron radiation [132] as well as by electrochemical quartz crystal microbalance [128]. The presence of the metal Ni2p-peak in Figure 4.10(a) indicates that the oxide layer is thinner than the escape depth of the photoelectrons. The thickness of an oxide can be estimated by assuming a homogeneous surface layer [135, 137-138] and by using this method the oxide layer on the Ni electrode was estimated to 0.8 nm. The metal peak from the NiZn shows (Fig. 4.10(a), curve ii) that the escape dept of the photoelectrons barely reaches through the oxide layer of the NiZn layer and due to the lack of a well defined Ni metal signal the thickness of the oxide layer could not be accuratly calculated. Platinum was not detected, indicating full coverage of both the Ni and the NiZn film on the Pt substrate.

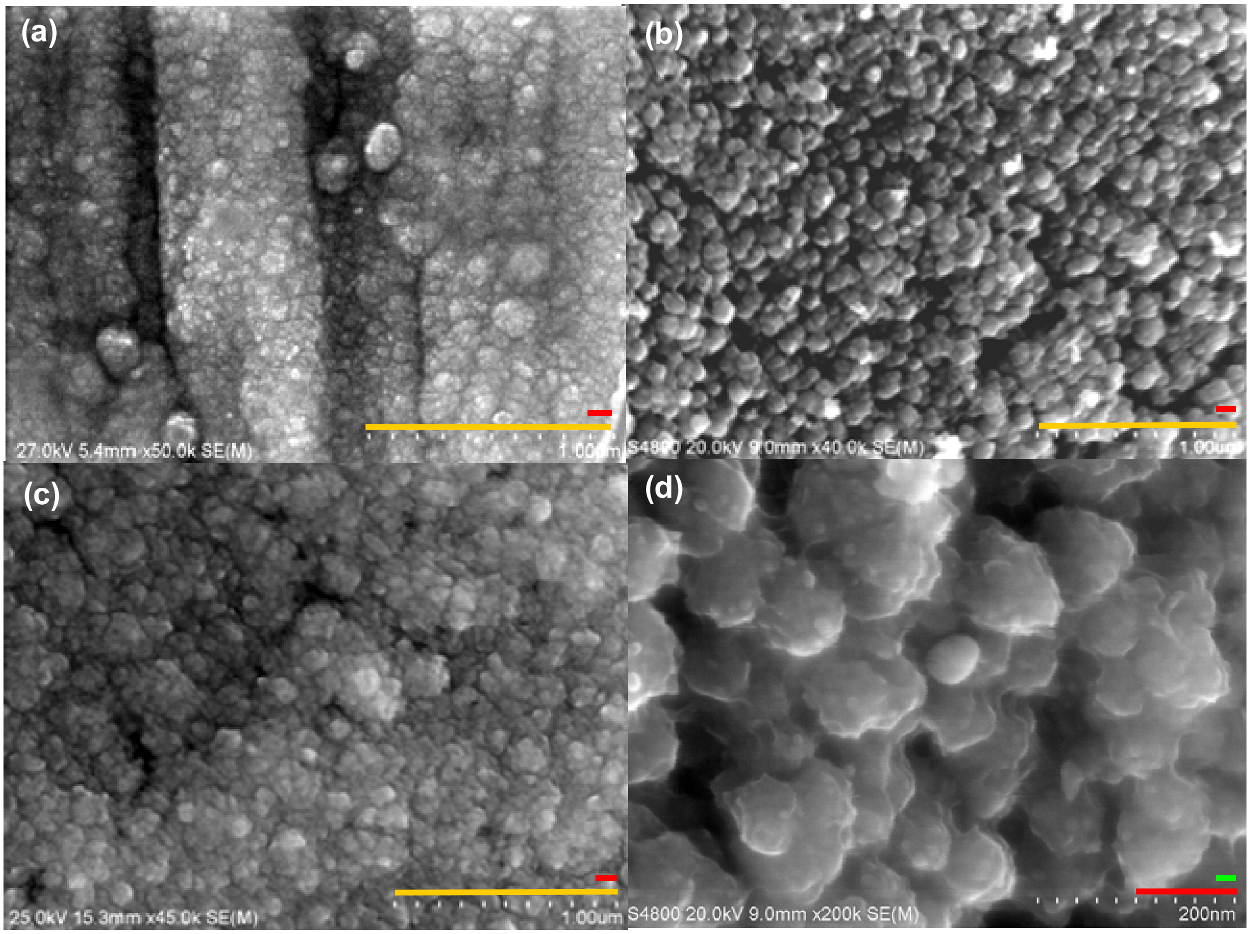

Fig. 4.9 SEM images of pulse plated NiZn alloys, ruler 🟨1 µm, 🟥100 nm, 🟩 20 nm. Electrode type: (**a**) RDE, (**b**) mesh, (**c**) foil, (**d**) mesh.

Due to the very weak NiO signals for the NiZn alloy its presence can be questioned. Since the literature is quite consistent with the two layered oxide structure on Ni metal, it is tempting to believe that changed properties for Ni in the NiZn matrix also changes the properties of the oxidised layer. This change may yield a more open structure where H_2O, H^+ and OH^- can be more easily transported and by that hinder the formation of NiO [27] (Section 2.1.2). A consequence of a more open structure would be that the hydroxide can grow much thicker before a NiO layer becomes thick enough to slow down the overall Ni oxidation process which could explain the thicker hydroxide layer seen for NiZn.

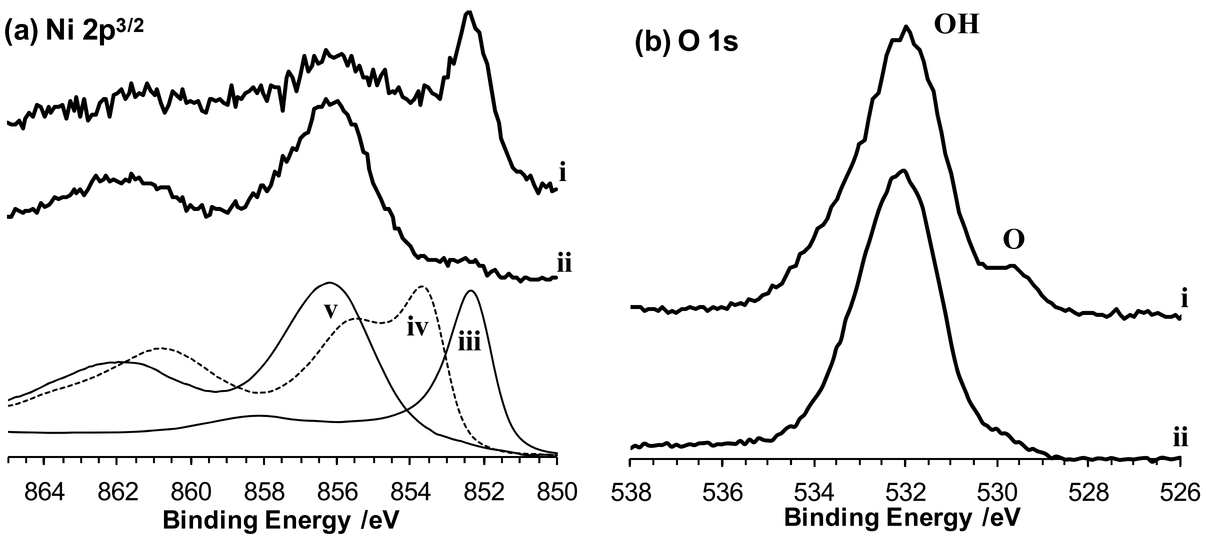

Fig. 4.10 XPS spectra from pulse plated RDEs of Ni and NiZn. (**a**) Ni signal and (**b**) O signal for: (**i**) pulse plated Ni and (**ii**) NiZn. Reference spectra: (**iii**) Ni metal, (**iv**) NiO and (**v**) $Ni(OH)_2$.

Depth profile investigations by XPS under mild Argon-ion etching showed that only Ni and Zn metal was detected after the removal of the oxides on the surface of the sample (Fig. 4.11).

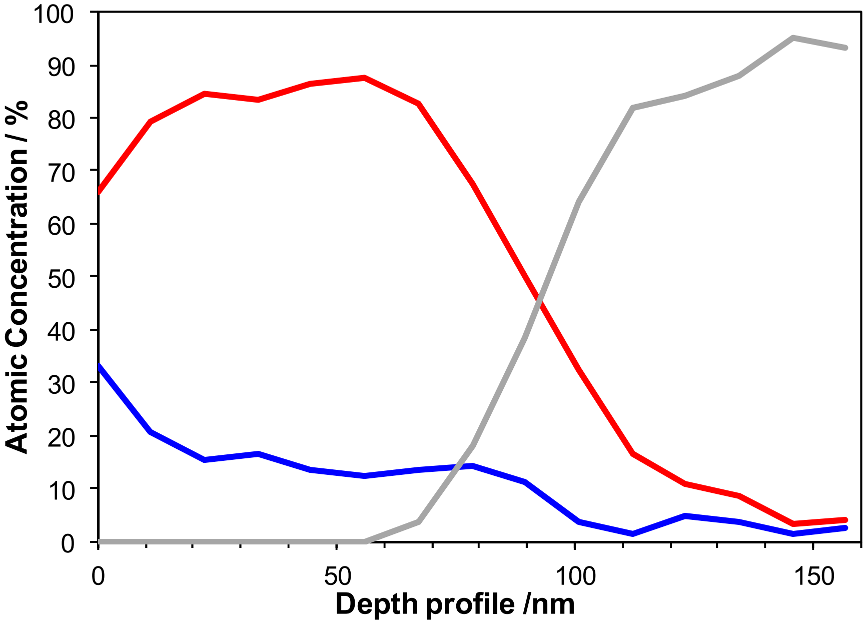

Fig. 4.11 XPS depth profile by argon sputtering of NiZn alloy a10, photoelectron signal for the metal atom: ▬ Pt4f, ▬ Ni2p, ▬ Zn2p.

4.2.2 Long Range Structure

The crystal structure of the pulse plated alloys was first investigated with XRD by Ahmed [117], but since the main signal received was from Ni(111) which overlapps with the signals from the fluorescent Fe substrate (giving high background), the structure could not be determine. The XRD spectra of the NiZn foil electrodes from paper II are shown in Figure 4.10. The relative intensity of the broader diffraction peaks vs. the sharp Pt peaks (substrate) reflects the relative thickness of the alloys which corresponds well to the EDX results in Figure 4.6(a). The peak at 44.12 can be attributed to either the (111) reflection of a cubic lattice of Ni or to a (101) reflection of Zn and corresponds to a Me-Me bond with an interatomic distance of 2.51 Å.

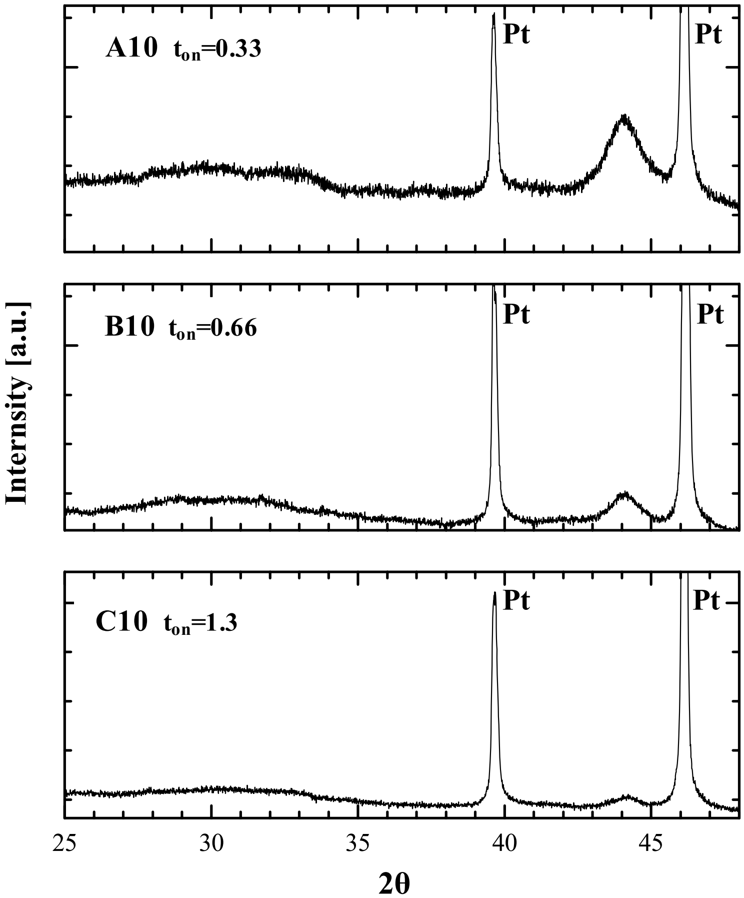

Fig. 4.12 XRD spectra of the pulse plated NiZn foils at three different pulse times (Table 4.2).

The lack of well defined peaks from the broad scattering area in the 20-30 2θ range does not provide enough information to determine a real atomic arrangement, instead this area indicates a randomly arranged co-existing stacked *hcp* and *fcc* motives. A short range mix of these crystal structures would give an apparent amorphisation when analysed with XRD which relies on a "long range" order for proper diffraction. In the case of a short range ordered or an amorphous structured atomic arrangement, XAFS is one of few techniques that can provide useful structure information.

4.2.3 Short Range Structure

Due to the indication of a possible short range crystalline structure in XRD the NiZn plated alloys were investigated by XAFS. Both XANES and EXAFS were measured in fluorescence mode on Ni K and Zn K edges. All the data handling necessary prior to the local structure refinement, such as normalisation, smoothing and background subtraction, the Fourier transformations of the spectra and the windowing, was made in the IFEFFIT software package [114]. The analysis of the local structure was then carried out using Artemis (non-linear least square) NLLS module of the IFEFFIT package. The theoretical models were generated by the use of the FEFF6.2 library. For a more detailed description see paper II.

The scattering parameters for Zn and Ni are very similar and the two can therefore not be easily distinguished which was a problem also for the XRD spectra (Fig. 4.12). In XAFS however, it is possible to lock at the closest environment of "single" atoms and the whole refinement had to be based on bond distances. The theoretical models used for the XAFS refinement are modified *hcp*- and *ccp*-like structure models. When the EXAFS function was calculated for the different pulse times and concentrations it was shown, for the A-C5 series, that the Ni EXAFS functions were sensitive to the plating times while the Zn functions were not (Fig. 4.13(a)). The opposite relation was seen for the A′-C10 series of electrodes (Fig. 4.13(b)). The trend of having one component in the alloy reflecting the EXAFS function of the different pulse conditions while the second component does not, implies that the alloy is more of a multiphase system with a non-homogeneous distribution of Zn, rather than a solid solution.

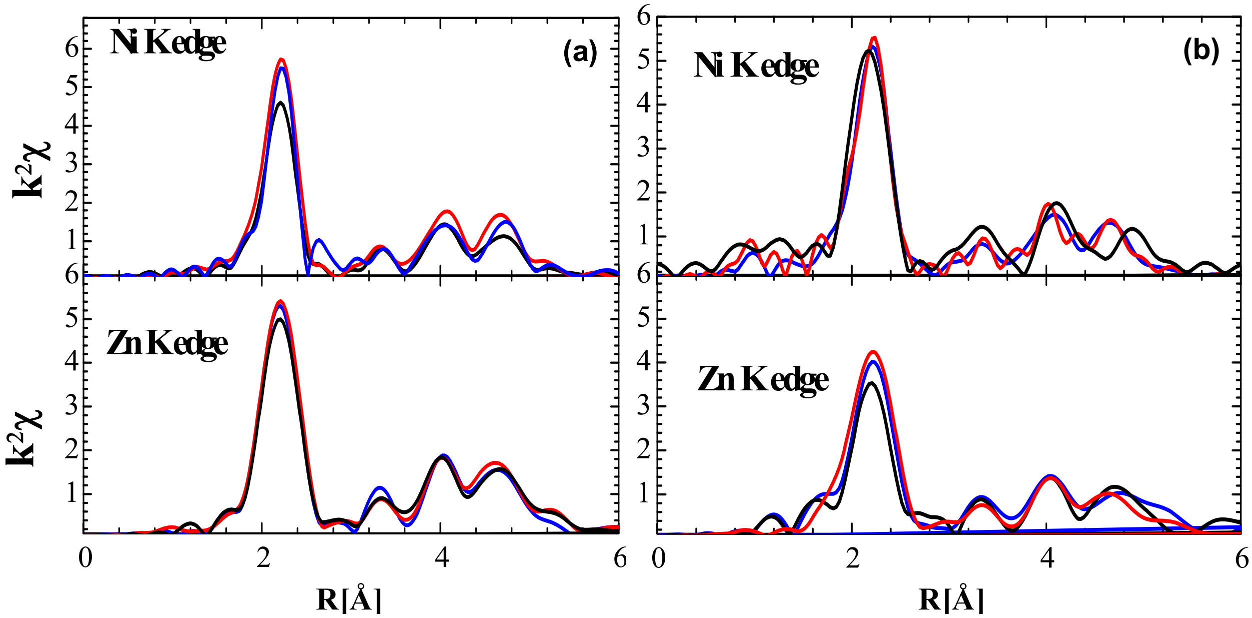

Fig. 4.13 EXAFS spectra's of pulse plated NiZn foils. (**a**) ▬ (A5)0.33/3.5s, ▬ (B5)0.66/7s, ▬ (C5)1.3/14s, k^2 normalised to Ni and Zn EXAFS function. (**b**) ▬ (A′10)0.24/2s, ▬ (B10)0.66/7s, ▬ (C10)1.3/14s, k^2 normalised to Ni EXAFS function.

For the A-C5 series it was shown from the Zn edge EXAFS data that the local environment of the Zn atoms are identical regardless if the initial structure model was *hcp* or *ccp*, which suggests that both arrangements are almost identical on the length scale of the refinement (~4 Å). The Ni edge refinement model was based on the coexistence of Ni in both *hcp* and *ccp* environment, anticipating that that the *hcp* contains both Ni and Zn while *ccp* is Zn free. In the refinement model for Ni the local arrangements from Zn edge data and overall composition of the alloy was constrained. The refinement of the EXAFS data showed that alloys A-C5 contained 80-90% *hcp* (Table 4.3) with the bond distances; Zn-Zn=2.62-2.66, Zn-Ni=2.50-2.51 and Ni-Ni=2.48-2.50 Å. The fraction of the phases are little affected by the changes in pulse cycle time but the alloyed material (the *hcp* phase) in the deposit showed a decrease of Zn content with increasing pulse cycle time which, as there is no overall change in Zn content of alloy A-C5, indicates a larger amount of clustering Zn with increasing pulse times (Table 4.3). This difference is likely to induce different amounts of strain in the differently pulsed samples due to the large variation in bond distances.

Table 4.3 Chemical composition and relative representation of the hexagonal and cubic like local structure in pulse plated NiZn alloys. The XAFS refinement results for A′-C10 have been combined with the EDX composition data for an estimate of the fraction of coexisting *hcp* and *ccp* environment.

Electrode notation	Zn(at%) EDX	*hcp* fraction	*hcp* compostion	*ccp* fraction	*ccp* compostion
A5	14	0.8	Ni_3Zn	0.2	Ni
B5	14	0.8	$Ni_{3.4}Zn$	0.2	Ni
C5	14	0.9	$Ni_{5.5}Zn$	0.1	Ni
A′10	21	0.62	Ni_4Zn	0.32	Ni_5Zn
B10	18	0.52	$Ni_{3.6}Zn$	0.48	$Ni_{4.2}Zn$
C10	16	0.31	$Ni_{2.1}Zn$	0.68	$Ni_{11}Zn$

For the A′-C10 series the Ni XAFS function show a low sensitivity towards the change in plating times compared to the large change in the function for Zn. The differences in the XAFS function compared to the A-C5 series required a modification of the refinement procedure, and both alloy components had to be assumed to be present in both considered environments (*hcp* and *ccp*), and that the composition of both coexisting phases may vary. The Ni edge EXAFS functions indicates that the Ni-Ni and Ni-Zn bond length are generally shorter, and closer to that in pure Ni (2.50 Å) in the *ccp*-like environments than in the *hcp* (2.53 Å). The amount of Ni present in the *hcp* environment decrease significantly with increasing length of the pulse cycle. The Zn edge EXAFS functions show that the Zn-Zn distances differ considerably between *hcp* and *ccp* environment. The bond length of Zn-Zn in the *hcp* environment (2.62-2.64 Å) is slightly shorter to that of pure Zn, but in the *ccp* environment the bond length is more like the cubic allotrope of Ni. The coexistence of these two very different Zn environments is expected to induce a large stress on the local structures in the alloy. The fraction of Zn in the *hcp* environment is however independent of the length of the pulse cycle.

The results from the XAFS refinements for A′-C10 was combined with the average chemical composition data and the fraction of coexisting *hcp* and *ccp*-like environments and the most probable chemical composition of each fraction is shown in Table 4.3. From Table 4.3 it can also be seen that the fraction of *hcp* and the fraction of Ni in the *hcp* environment decrease with increasing length of the pulse cycle. In the A-C5 series (5% [Zn^{2+}]) the trend is opposite with an increased fraction of Ni in the *hcp*-like structure with increased pulse length.

The *ccp* phase for the longest pulse cycle of 10% [Zn^{2+}] (C10) resembles the samples from the 5% [Zn^{2+}] electrolyte and the lower Zn concentration in the alloy appears to make the *ccp* phase strive towards a Zn free environment.

It was suggested already in 1950th that the presence of hydrogen in plating or sputtering step can induce metastable *hcp* arrangement in pure Ni [139]. Fast potential scan methods [140] and epitaxial deposition [141] have been used to deposit Ni with a prevailing *hcp* structure but for a pure *hcp* phase the use of more complicated electrolytes has been used [142-144]. It is well known that an *hcp* arrangement can be induced to a Ni structure by small amounts of alloying material, even on impurity level [145], which can be seen for e.g. $Ni_{95}Si$ [146]. Relevant literature for NiZn alloys with low Zn content in analogy with the $Ni_{95}Si$ [146] system is sparse, but it is not too difficult to imagine that Zn can induce the *hcp* structure also when it is present in low amounts. It is also very likely that Zn is deposited anomalously in higher amounts than what EDX show during t_{on}, which is partly dissolved during t_{off}. Hydrogen induced *hcp* is also possible explanation since it is a part of the pulse current but there are no pure hcp Ni phases, and from Table 4.3 and series A-C5 and A´-C10 the effect of Zn in the alloys appears to have been the important factor for the formation of the *hcp* fraction.

It has also been suggested that phase transition between densely packed structures (*fcc* to *hcp*) can occur in small particles (~20 nm) if the molar volume becomes larger when a foreign atom is induced [146]. This effect would be in analogy with the phase transition from *bcc* to *ccp* as the importance of a lower surface tension increases when the surface/bulk fraction increases [146]. The plated NiZn alloys are built up by particles in this size range and the effect of larger volume of the unit cell in nanoparticles may well contribute to the formation of the *hcp* structure.

4.3 Proton reduction on NiZn alloys

The proton reduction reaction (PRR) was used to study the electrocatalytic properties of the different NiZn alloys and the relation to the pulse parameters. The proton reduction was chosen for several reasons, first it is a very important reaction and a good and cheap catalyst for this reaction is of great interest in the perspective of the hydrogen economy. Secondly, an acid environment prevents the build up of thick oxide layers, which is important since the properties the alloy should refer to the metal phase, Thirdly, proton reduction is an electrocatalytic process i.e. the electron is transferred as the protons adsorbs on the surface and the formation of H_2 takes place on the surface which makes the reaction sensitive to changes in the surface properties.

The proton reduction ability of the NiZn alloys was investigated by the use of RDEs in 0.5 M $NaClO_4$ at pH 2.8. The pulse parameters described in Table 4.2 were used with the exception of the number of pulses that was 40 for all the RDE alloys. In Figure 4.12(a) it is shown that the NiZn alloy plated in the 10% Zn^{2+} bath is far more reactive towards the PRR than the alloy plated in the 5% Zn^{2+} bath and that both alloys are far better than a solid Ni electrode. Corresponding NiZn plating was made on a Ni(s) RDE and the PRR results were very similar, as can be seen in Figure 4.12(a) (purple curve). Figure 4.12(b) shows that the electrocatalytic activity of the NiZn electrodes are significantly affected by the change in pulse parameters and the largest difference in activity can be seen when the pulse time is decreased from t_{on}=0.66 to t_{on}=0.33 s. The same trend was seen also for the electrodes plated in the lower Zn^{2+} bath.

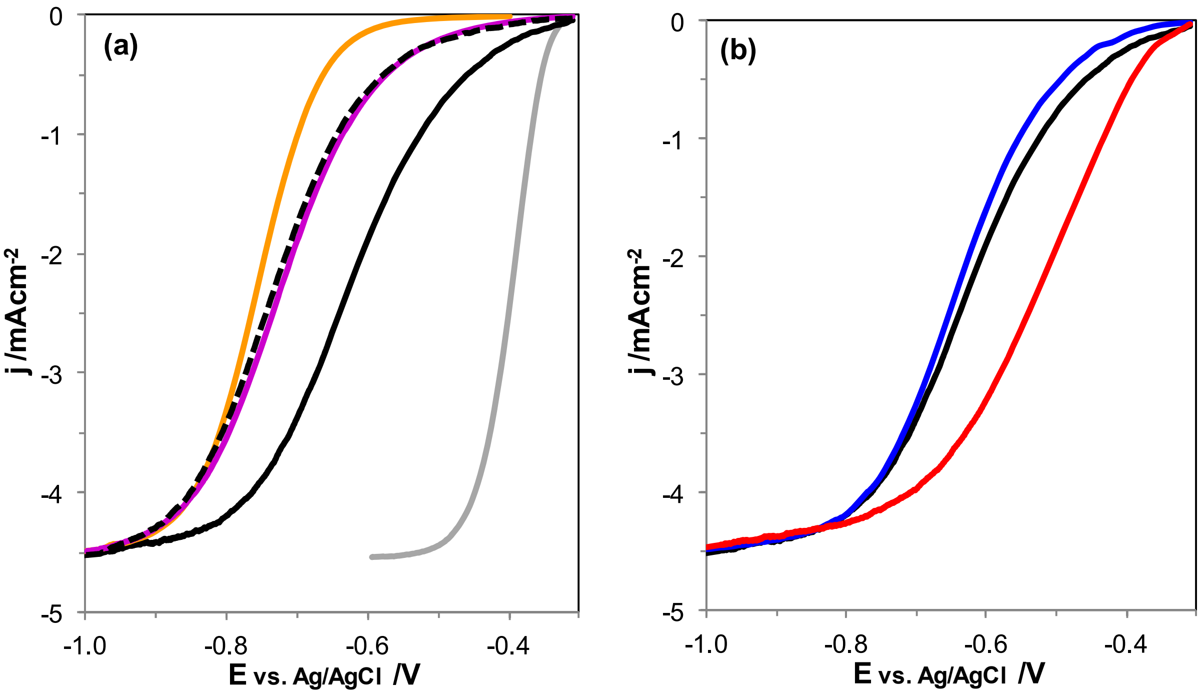

Fig. 4.14 PRR in 0.5 M NaClO4 at 10 mV^{-1} and 2500 rpm. (**a**) ▬NiZn(b10) t_{on}=0.66 s, --- NiZn(b5) t_{on}=0.66 s, ▬ NiZn(b5) on Ni(s) t_{on}=0.66 s, ▬ Ni(s) and ▬ Pt(s). (**b**) ▬NiZn(a10) t_{on}=0.66 s, ▬NiZn(b10) t_{on}=0.66 s, ▬ NiZn(c10) t_{on}=1.3 s.

The measurements of proton reduction on NiZn electrodes in pH 2.8 was however not straight forward as the alloys were not completely stable in pH 2.8, and a decrease in activity was seen between each measurement. This possible error source was however minimised by experimental planning in terms of the use of the exact same order of the sweeps at different rotations and time in between them, for all the electrodes. A reference sweep at 2500 rpm was repeated in between the other rotation rates so that the decrease of activity could be followed. All comparisons of the electrode activity could then be made between electrodes with the same history.

The kinetic parameters (k and α) and the diffusion coefficients (D) were received by non-linear least squares fitting to the experimental data and are presented in Table 4.3. The first electron transfer was assumed to be the rate limiting step. The rate constant for the NiZn electrodes varied from 0.28 to 29×10^{-4} cms^{-1} for b5 to a10, which is significantly higher than for the solid Ni electrode (5.2×10^{-6} cms^{-1}). The value of the transfer coefficient (α) for NiZn is between 0.3 and 0.5 and the value for Ni is 0.6, which indicates that the transition state is more proton like on Ni and closer to adsorbed hydrogen on NiZn. It can also be noted that α is significantly lower (0.33) for the three electrodes with the highest rate constants than for the three electrodes with the lowest rate constants (α=0.47). This indicates, for these alloys, that when a transition state resembles the adsorbed hydrogen more than the loosely interacting proton, faster reaction rates are obtained.

Table 4.3 Results of the kinetic analysis of the PRR on NiZn RDEs at various plating parameters and 40 pulses.

Electrode notation	t_{on} /s	$[Zn^{2+}]$ /mM	α	k /cms^{-1} ×10^{-4}	D /cm^{-2}s^{-1} ×10^{-5}
a5	0.33	5	0.3	2.34	4.98
b5	0.66	5	0.5	0.283	4.79
c5	1.30	5	0.5	0.353	4.70
a10	0.33	10	0.4	28.9	4.80
b10	0.66	10	0.3	9.36	5.21
c10	1.30	10	0.4	4.36	4.97

Kinetic experiments were performed in 0.5 M $NaClO_4$ at pH 2.8

From the results of the kinetic analysis in Table 4.3 it can be seen that the higher Zn^{2+} concentration in the plating bath increases the reactivity of the NiZn alloy towards proton reduction. For the alloys plated with 10% $[Zn^{2+}]$ in the electrolyte an increase in reaction rate with a decrease in pulse time was also clearly seen. The alloys plated from the lower Zn^{2+} concentration only showed an increased reactivity for the shortest pulse. When the kinetic analysis is compared with the EDX results from Figure 4.6, the activity of the PRR may be correlated to the Zn content of the alloys (even though the differences are small) in the case of 10% $[Zn^{2+}]$ in the plating bath. The high rate constant of a5 can however not be correlated to Zn content in the alloy, as determined by EDX. The effect of substrate can also be excluded since the results from the NiZn plated on Ni(s) show that the substrate is not important for the catalytic activity of the NiZn alloys towards the PRR (Fig. 4.14(a)). Another possible correlation with reactivity is the fraction of *hcp* and *ccp* structural motives in the alloy. Also this correlation fails when alloys from 5 and 10% $[Zn^{2+}]$ electrolyte are compared, mainly due to the rate constant of a5. It is suggested in paper II that the increase in rate constant with the increase of *hcp* fraction could be a consequence of the increase in strain in the Ni-Zn *hcp* structure which would shift the *d*-band centre of the Ni upwards and possibly increase the coupling to the adsorbed specie. The results from the 5% $[Zn^{2+}]$ series does not allow such generalisation but rather indicates that there are other factors that control the catalytic properties of the these alloys. However, the fact that some of these alloys show significantly higher reaction rates depending on pulse conditions deserves further attention and to establish a correlation between reaction rate and structure, additional measurements and possibly also theoretical calculations of the band state in such complex alloys are necessary.

4.4 Oxygen reduction

The electrocatalytic properties of pulse plated Ni and NiZn towards oxygen reduction was evaluated by the use of rotating ring disc electrodes (RRDE) in alkaline electrolyte. The general importance and the theory of the ORR are further discussed in Section 2.2.1. The RRDEs were used to investigate the fraction of oxygen reduced to hydrogen peroxide (H_2O_2) and water, respectively. The theory for the evaluation of a RRDE experiment is described in Section 3.1.3 and Eqn. 3.8-13. The theoretical value of the collection efficiency (N) was calculated to 0.526 and experimentally determined to 0.516 for the un-plated Pt RRDE that was used as a substrate for the pulse plating. The average number of electrons involved in the ORR was calculated in two ways; by the use of both the disc and ring current as in Eqn. 3.13 and secondly by the use of the disc current at different rotation rates and the Koutecký-Levich (K-L) equation (Eqn. 3.15). The pulse plated RRDEs were, after the plating and stripping procedure, cycled 44 times in 0.1 M KOH to receive a steady response in alkaline solution as described in Section 4.1.2.

Figure 4.15 shows the voltammetry of the RRDE measurements for pulse plated Ni and NiZn and there are several significant differences between the two in both the disc and the ring currents. Most important is that the onset potential for O_2 reduction at -0.05 mA is 64 mV more positive on the NiZn than on the Ni(pp) electrode. Secondly, the reduction path for the ORR on the NiZn electrode changes with potential which is not the case for Ni(pp).

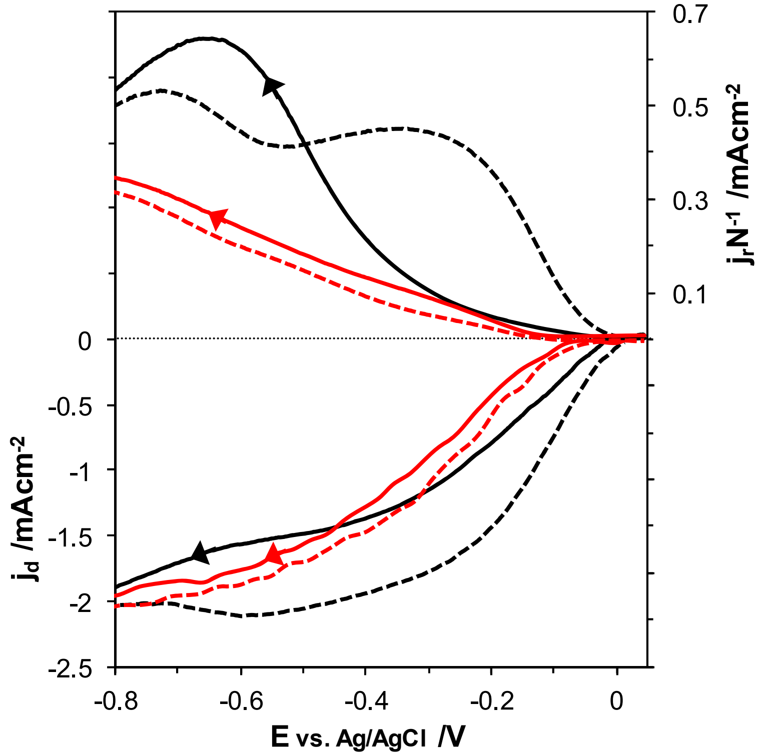

Fig. 4.15 ORR in O_2 saturated 0.1 M KOH at 10 mV^{-1} and 900 rpm. ▬ Ni(pp) and ▬ NiZn(b10).

A change in the reaction path for the ORR on NiZn can be seen at -0.65 V in the negative sweep direction when the disc current increases and the corresponding ring current starts to decrease. The second change of the reaction path occurs during the positive going scan at 0.55 V when there is a large increase of the ring current not seen in the negative going sweep direction. The higher disc current for both Ni(pp) and NiZn for the scans in positive direction implies that a change in the surface take place at the very negative potential. The impact on the O_2 reduction path of these changes between disc and ring currents shown in Figure 4.15 is more clearly shown in a plot of the number of electrons involved in the reduction, or as the percentage H_2O_2 produced from each O_2 molecule that has been reduced (Fig. 4.16).

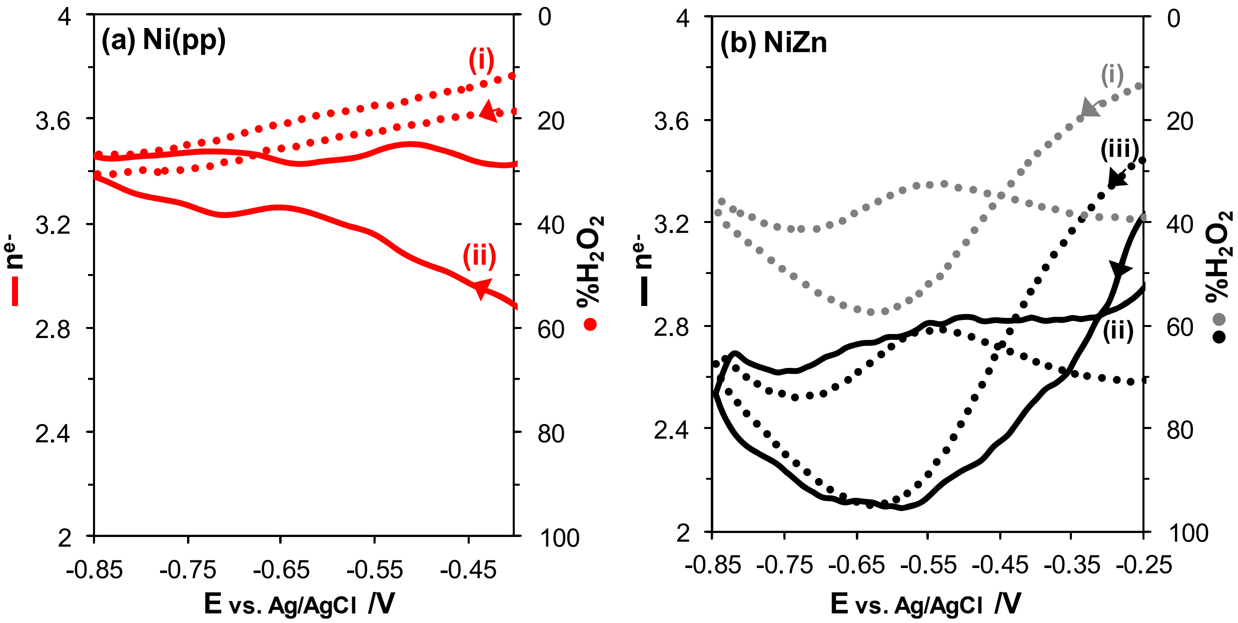

Fig. 4.16 Average number of electrons (from K-L equation) and %H_2O_2 (from the disc to ring current) involved in the ORR. (**a**) Ni(pp), (**b**) NiZn. (**i**) ●● %H_2O_2 with experimentally determined *N*, (**ii**) —/— K-L, (**iii**) ● %H_2O_2 with apparent *N*.

The two different ways of calculating of the number of electrons involved in the ORR are presented in Figure 4.16. A substantial discrepancy between the two calculations can be seen for Ni(pp) at low overpotentials and for NiZn over the whole potential region. The larger amount of H_2O_2 given by the K-L equation indicates that the collection efficiency determined for the un-plated Pt RRDE may not be valid for the plated NiZn alloy. An apparent collection efficiency of 0.23 for the NiZn electrode was used to fit to the number of electrons involved calculated from Eqn. 3.12 to the numbers given by the K-L equation (Fig. 4.16(b), iii). The amount of H_2O_2 produced varied between 25 and 55% on Ni(pp) and between 40 to 95% on NiZn, depending on sweep direction and potential.

The ORR on these pulse plated electrodes is a complicated matter which can be seen first in the low overall current response, and secondly by the discrepancy of reduction path between the values calculated from the disc only (K-L) and the value from the disc and ring (*N*). The low limiting current may be explained by assuming a porous structure of the hydroxide formed on top of the nanostructured metal surface (formed during the cycling in KOH). If the oxide/hydroxide layer has a low conductivity and is thick enough it can generate a recessed electrode with a substantially smaller geometric area and thereby a lower limiting current [147]. In the case of a recessed electrode an extra term is added to the K-L equation (Eqn. 6.1, Section 6.5.1), though the number of e^- calculated from the slope of the K-L equation is still valid [147]. The discrepancy of the results from the number of electrons involved in the O_2 reduction may be explained by O_2 reduction within the porous $Ni(OH)_2$ structure, the H_2O_2 formed may not be transported rapidly enough to the ring and instead decompose chemically within the pores.

Even though the system is complicated it is quite clear that the oxygen reduction path towards hydrogen peroxide is significantly increased by alloying Ni with Zn and that the overpotential for the ORR is decreased.

5 Electrochemical propen and propenol oxidation

5.1 Background

A large part of the work presented in this thesis was undertaken within the objectives of two European collaboration project CLETEPEG (se Chapter 6) and ‘‘Nanostructures for Energy and Chemicals Production’’ (NENA) and the task in paper III was to investigate new electrode materials for oxygen insertion (preferably epoxidation) reactions that could be used in a fuel cell reactor for co-generation of clean chemicals and energy. Propen oxidation to epoxypropan was considered highly prioritised in project NENA due to its importance in the chemical industry (7-8 million tons/year) and the lack of simple direct production rout.

In a literature search a few papers were found reporting direct electrochemical epoxidation of propene on silver, steel, nickel and palladium electrodes [148-152] and there were also a number of patents on this topic. Based on the promising results found in these reports, the project was started by screening these known materials for direct epoxidation of propen in alkaline solution. Both propen and its alcohol analogue, propenol, was investigated using some of the electrode materials that was reported to work successfully as epoxidation catalysts. Propenol was chosen due to its liquid properties, which makes it more easy and safe to handle and it can easily be added in any concentration. Propenol had previously been reported to be readily oxidised to 2,3-epoxy-1-propanol on TS-1 [153], even though this was epoxidation by in-situ produced H_2O_2. Stainless steel was the most efficient catalyst for direct epoxidation in the investigation by Oduoza [150] and since steel contains a variety of alloying elements three different types of steel (430L, 304L and 316L), iron, chromium, nickel and manganese were investigated.

The oxidation of propen was subsequently investigated by the use of cyclic voltammetry (CV) in 0.1 M KOH, de-areated with nitrogen gas and then saturated with propen gas at room temperature. None of the investigated materials gave any current response between H_2 and O_2 evolution that could be interpreted as oxidation of propen. When the corresponding measurements were made with propenol an increased current response was observed for manganese and nickel materials. Due to large response for Ni a simple CV investigation was performed also for its nearest neighbours in the periodic system, cobalt and copper. The CV response of the four transition metals (Mn, Co, Ni and Cu) in 1 M propenol is shown in Figure 5.1, the oxidation current from Cu shows the largest potential decrease with the addition of propenol of the four but Ni show oxidative currents at even less positive potentials. The oxidation currents of interest for this investigation where found prior to the oxygen evolution and is most likely to be propenol oxidation but could also be due to an increased activity of water oxidation induced by the presence of propenol.

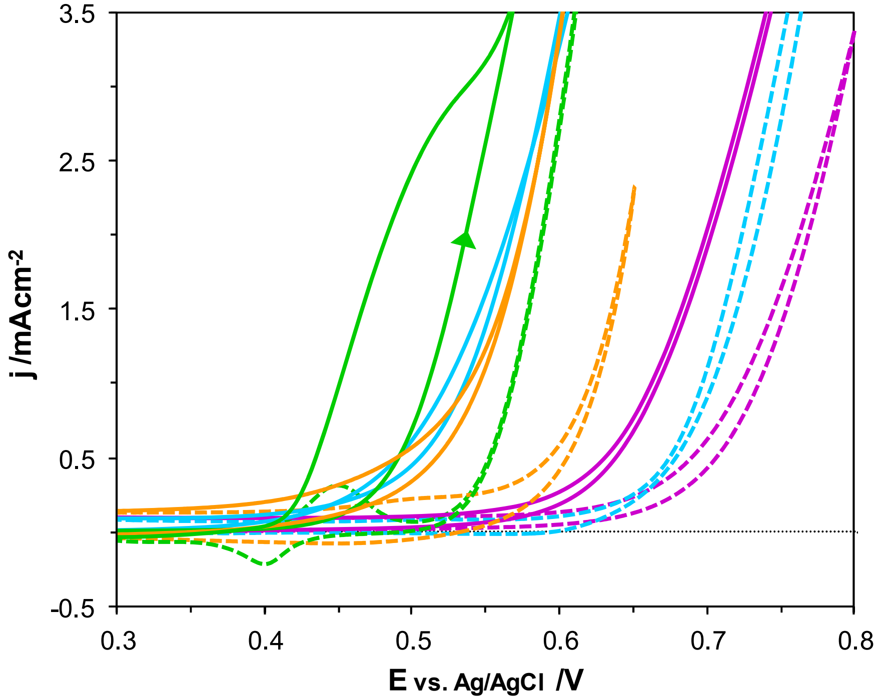

Fig. 5.1 CV response from 0 (dashed curves) and 1 M propenol (full lines) oxidation in 0.1 M KOH, 10 mVs^{-1}. Electrode material: ▬ Mn, ▬ Cu, ▬ Co and ▬ Ni.

Only nickel based electrodes were chosen for further analyses by CV and differential mass spectrometry (DEMS) and the major investigations were made on Ni(s), pulse plated nickel (Ni(pp)) and pulse plated NiZn alloys. The propen oxidation on the 316L steel electrode was also further evaluated by the use of DEMS in a chemical approach and will be presented shortly in Section 5.3.

5.2 Electrochemical characterisation of propenol oxidation

Oxidation of propenol was investigated by the use of CV on Ni(s) and NiZn RDEs (Fig. 5.2). Propenol was added sequentially (0.01 M, 0.1 M and 1 M) to the de-aerated 0.1 M KOH electrolyte and the potential was swept in positive direction until a substantial level of O_2 evolution was gained before the direction of the sweep was reversed.

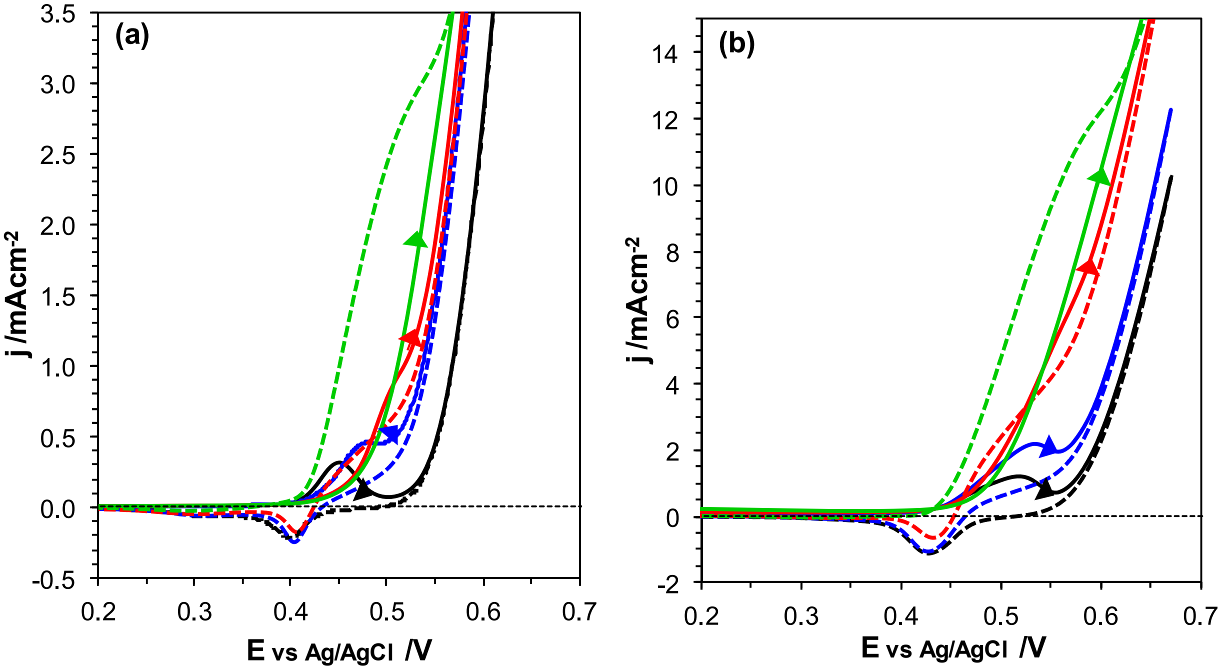

Fig. 5.2 CV in 0.1 M KOH at 10 mVs^{-1} with sequential addition of propenol: ▬ no propenol, ▬ 0.01 M, ▬ 0.1 M and ▬ 1 M propenol. (a) Ni(s) disc, (b) pulse plated NiZn on Pt disc. The reverse sweeps are shown as dashed lines.

The black curves show the familiar redox couple $Ni(OH)_2/NiOOH$ discussed in detail in Section 2.1.2 and 4.1, and the larger peak separation of the less reversible redox couple on NiZn is clearly shown. A current increase was seen for each concentration at the potential of the $Ni(OH)_2$ oxidation. In the presence of propanol the CV response for the three different electrodes is similar, however the magnitude of the currents differ, which is connected to a larger amount of active sites (real area) on the NiZn electrode. The NiZn electrodes also show slower redox properties, which generate a wider peak separation (the properties of the electrodes are further discussed in Chapter 4. The current increase in the presence of propenol may be interpreted either as oxygen evolution at a less positive potential, propenol oxidation or both. It has previously been reported that oxidation of organic compounds on certain IrO_2 modified titanium and Boron Doped Diamond surfaces pursues only if O_2 is simultaneously evolved and then at a significantly lower positive potential than expected [154-155].

The sweep rate dependence was in addition investigated for 2, 10 and 100 mVs^{-1} in 1 M propenol but the current was, as expected from Figure 5.2, neither controlled by reactants in solution nor by strongly adsorbed reactants according to Eqn. 3.1-3. The oxidation current is, by other words, not determined by a simple electron transfer reaction.

There are *three* main interesting features seen in the anodic part of the voltammograms that need to be further investigated; *first* the large increase in oxidation current at on-set potential, *second* the disappearance of the NiOOH reduction peak with increasing amount of propenol and *third* the large increase in the oxidation current for the negative reversed sweep compared to the positive going sweep.

5.2.1 The increase of the oxidation current at the initial positive going sweep

The on-set potential for the current increase on Ni(s) and NiZn due to the propenol/water oxidation during the sequential addition of propanol appears to follow different mechanisms. Figure 5.2 shows that the oxidation on Ni(s) start after significant conversion to NiOOH has taken place but for NiZn the oxidation appears to start before the conversion to NiOOH begins. The corresponding measurements at 2 mVs^{-1} (Fig. 5.3) indicates however that the on-set potential follow the same pattern for both Ni(s) and NiZn electrodes and that the oxidation take-off shows only minor potential difference (±0.02 V) where the higher propenol containing solutions appear to start at the less positive potential.

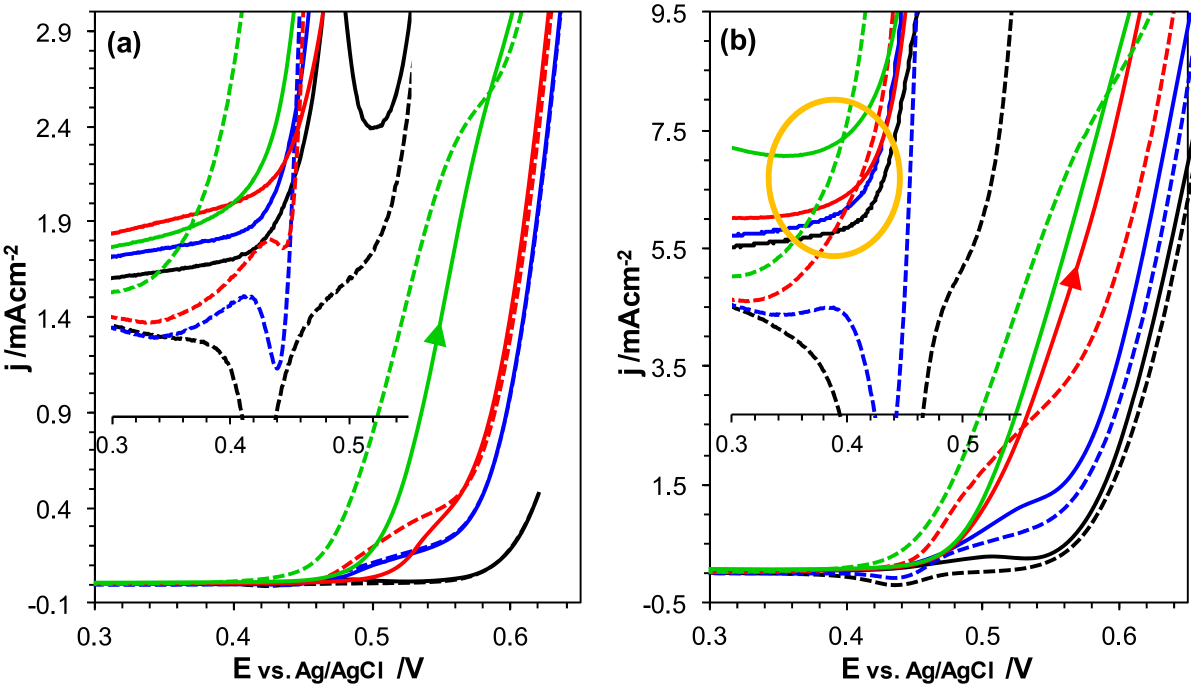

Fig. 5.3 CV on (a) Ni(s) and (b) NiZn in 0.1 M KOH at 2 mVs^{-1}; ▬ no propenol, ▬ 0.01 M, ▬ 0.1 M and ▬ 1 M propenol, (inset) highlights the on-set points for the oxidation. Solid line positive sweep direction and dashed line the reversed negative sweep.

5.2.2 The disappearance of the NiOOH reduction peak

From Figure 5.2(a) and (b) it can be seen that the reduction peak of the NiOOH becomes smaller and eventually disappears as the concentration of propenol increases for all three electrodes. In Figure 5.4 the three concentrations of propenol are shown at three different sweep rates, which clearly indicate that the size of the NiOOH reduction peak depends on both the propenol concentration and the sweep rate. At a sweep rate of 100 mV^{-1} the reduction peaks are present for all concentrations and at the slowest sweep rate of 2 mVs^{-1}, only the reduction peak from 0.01 M propenol is seen. In the following cycles the oxidation of $Ni(OH)_2$ is, however, still equally large as in the sweep before, which implies that the NiOOH has to be reduced chemically, since no reduction is seen in the voltammogram. From the sweep rate behavior it can be assumed that the chemical reduction of NiOOH takes place at more positive potentials than its natural reduction potential and that the reduction rate is rather slow.

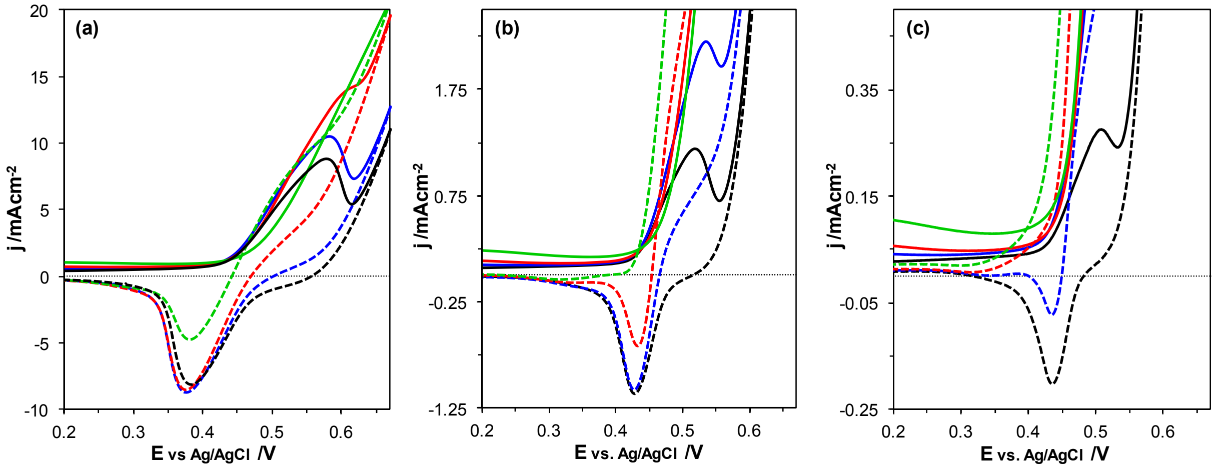

Fig. 5.4 CV on NiZn in 0.1 M KOH with addition of: ▬ no propenol, ▬ 0.01 M, ▬ 0.1 M and ▬ 1 M propenol. (a) 100 mVs^{-1}, (b) 10 mVs^{-1}, (c) 2 mVs^{-1}.

The sweep rate dependence of NiZn in presence of 0.01 M of propenol was analysed in paper III in Figure 4, in where the current density was normalised with the sweep rate assuming surface confined reactions. It was concluded that propenol oxidation on NiZn is slow and not governed by a simple electron transfer reaction. In same figure the poor reversibility of the Ni oxy/hydroxide for the NiZn plating, that caused the apparent different mechanisms discussed in Section 5.2., was also shown.

5.2.3 The enhanced oxidation current at the reversed potential sweep

It is clearly understood that the unexpectedly higher oxidation current during the reversed sweep compared to the positive sweep depends strongly on the propenol concentration and the sweep rate (Fig. 5.4). When the electrode was rotated the current increased even more above a certain potential marked with vertical lines in Figure 5.5. The most distinct effect from rotation was seen for 1 M propenol at the reversed sweep (Fig. 5.5 dark green curve).

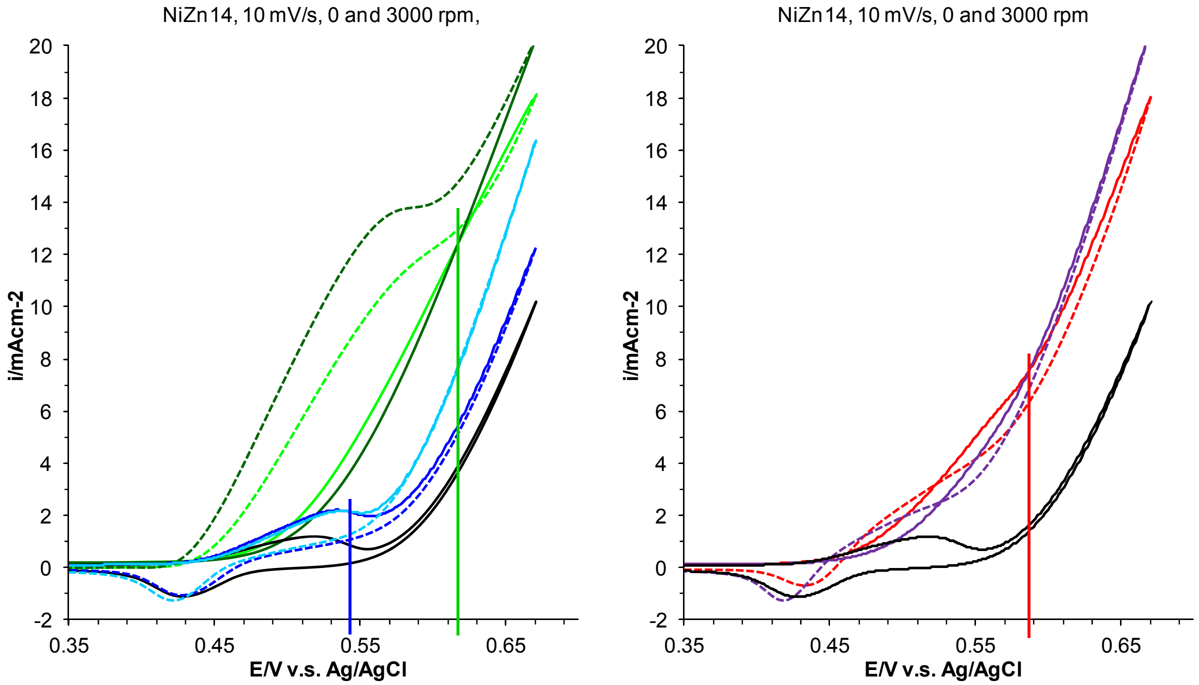

Fig. 5.5 CV on NiZn in 0.1 M KOH at 10 mVs^{-1}, 0 rmp; ▬ no propenol, ▬ 0.01 M, ▬ 0.1 M and ▬ 1 M propenol. 3000 rpm; ▬ 0.01 M, ▬ 0.1 M and ▬ 1 M propenol. The vertical lines mark the current cross-over between 0 and 3000 rpm measurements.

The very large increase of the current at the reversed sweep appears to be an effect of an activation of the surface at more positive potentials that is consistent even when the potential becomes less positive at the reversed sweep. The activated oxidation reaction benefits from the sharper concentration gradients, due to the rotation, all the way down to a potential prior the formation of the NiOOH in the positive sweep. These results indicate that the currents become influenced by mass transport only at more positive potentials and this effect sets in at higher potentials the higher the propenol concentration is. The reaction will not be fast enough to build up any concentration gradient until higher potentials are reached. At those high potentials (see the markers in Fig. 5.5) the reaction becomes influenced by mass transport.

Similar change in the diffusion dependency at increased concentrations in methanol oxidation has been observed by El-Shafei [69]. The type of cross-over of the reversed current shown for 0.1 M propenol has previously been seen for 0.5 M n-propylamin [60] and for 400 ppm glucose [67] on Ni electrodes but only very weakly for methanol oxidation [69] and in some cases not at all [70]. The much larger oxidation current at the reversed sweep seen for 1 M propenol in this study has, however, not to our knowledge been reported before.

5.2.4 Propanol oxidation

Propanol oxidation on NiZn and Ni(s) electrodes was investigated in analogy with propenol and is compared in Figure 5.6.

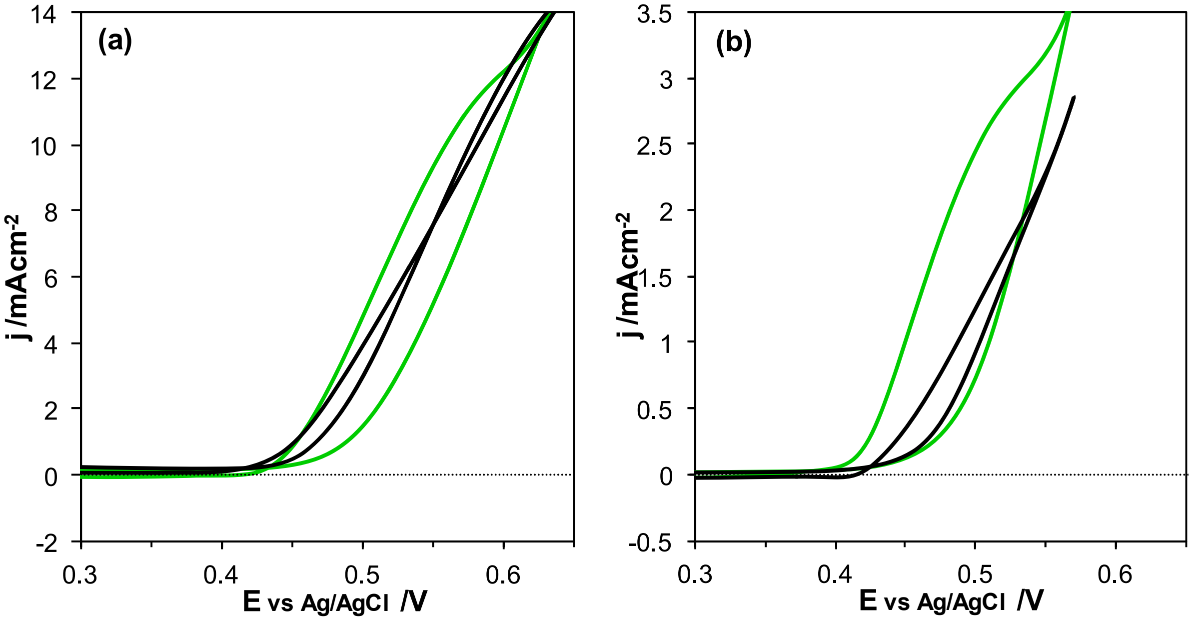

Fig. 5.6 CV on (a) NiZn and (b) Ni(s) in 0.1 M KOH at 10 mVs^{-1}: ▬ 1 M propanol and ▬ 1 M propenol.

The trends for propanol oxidation on NiZn and Ni are the same as for propenol, the on-set potentials are the same even if the activation profile for propanol is a bit sharper and the disappearance of electrochemical NiOOH reduction at high concentrations is about the same. The difference between the two can be seen in the hysteresis between positive and negative going scan, which for propanol is much smaller and can be compared with what has been reported previously in the literature (Section 5.2.3).

The chemical difference between the propanol and propenol is the carbon- carbon double bond and the role of unsaturated bonds in alcohol oxidation has been discussed in the literature for Au [156] and Pt [157] electrodes but not for Ni. The much higher oxidation ability for propenol over propanol on Au has been attributed to the higher free enthalpy of adsorption for propenol and the more stable de-protonated intermediate due to the different resonance structures it may attain. As can be seen from the activation currents from Figure 5.6 the oxidation process is most likely to be the same with or without the double bond but the large current increase at the reversed sweep seen only for propenol strongly indicates that the double bond is involved in the adsorption step also on Ni.

5.2.5 The change in surface properties by potential cycling in propenol

To investigate the hypothesis of “enhanced water oxidation” further, a NiZn electrode used for the CV analysis in 1 M propenol was utilised again in a propenol free electrolyte and cycled 1300 times at 10 mVs^{-1}. The CV responses from the measurements in different electrolytes are compared in Figure 5.7.

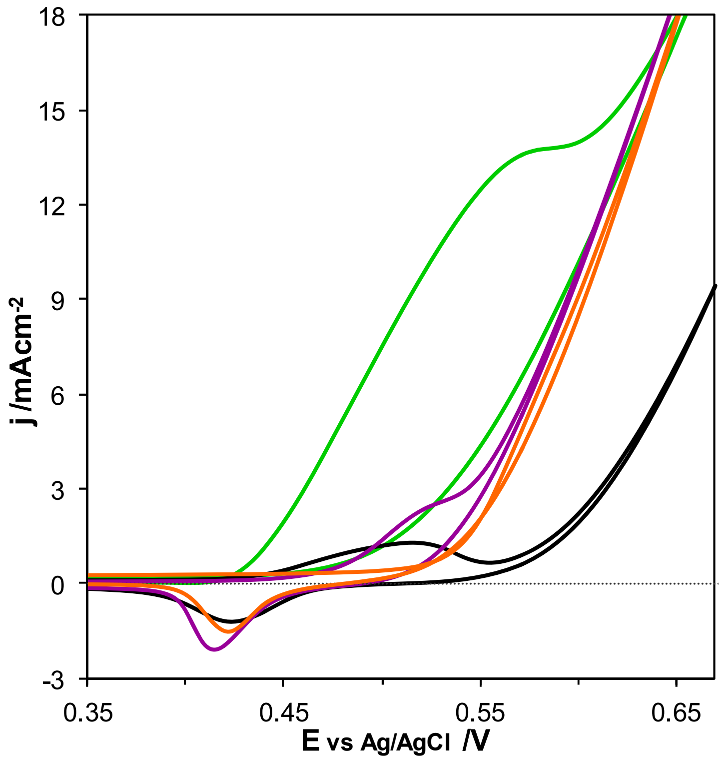

Fig. 5.7 CV on NiZn in 0.1 M KOH at 10 mVs^{-1}, 3000 rpm; ⬛ no propenol, 🟩 1 M propenol, 🟪 first sweep in pure 0.1 M KOH and 🟧 after 1000 cycles in pure 0.1 M KOH.

The first part of the sweep in pure 0.1 M KOH (purple curve in Fig. 5.7) is likely to be related to oxidation of adsorbed propenol derivatives, it can also be seen that the NiOOH reduction is regained and that the oxidation of $Ni(OH)_2$ is hidden in the O_2 evolution. After 1000 cycles the O_2 evolution is still activated 50 mV or more and it seems like the electrode has been permanently affected by the treatment in 1 M propenol. It is, however, not investigated further if the activity increase is due to a change in the nickel hydroxide structure/properties or by permanently attached residues at the surface.

5.2.6 Summery of the CV analysis

From the very first screening of different electrode materials (Fig. 5.1) it was shown that Ni poses electrocatalytic properties towards propenol oxidation since it decreased the overpotential by 150 mV compared to Mn. The results from the CV analysis have shown an oxidation process that is influenced by diffusion only after exposure to high overpotentials (Fig. 5.5) and that it is not a surface process controlled by a simple electron transfer reaction at a Langmuir isotherm. The $Ni(OH)_2$/NiOOH redox couple is clearly involved in the oxidation process since the oxidation starts only when NiOOH is about to form and the NiOOH is also completely consumed if the propenol concentration is high enough and enough time is given at high anodic potentials i.e. at slow sweep rates (Fig. 5.4). The difference in reversibility between NiZn and Ni(s) for the propenol induced current as well (Fig. 5.2) is related to the slower $Ni(OH)_2$/NiOOH redox process for pulse plated NiZn compared to pure Ni (Paper III, Fig.4), which further supports the indications of a redox dependent oxidation process. The comparison of the oxidation of propenol and propanol indicates that the double bond in propenol is involved in the process and may explain the large current increase at the reversed sweep (Fig. 5.6). The measurements from the "used electrode" in pure 0.1 M KOH show that the electrode becomes modified by the cycling in propenol with an enhanced water oxidation activity as a result and that this modification is quite stable, lasting over 1354 cycles with an electrode rotation of 3000 rpm (Fig. 5.7).

From the result above it appears as the oxidation current consists of two parts, the first part of the current increase is from propenol oxidation, which takes place at the formation of NiOOH (first activation potential) but at more positive potentials this process becomes accompanied by water oxidation (O_2 evolution). The water oxidation process occurs, however, at less positive potentials than expected when a Ni electrode has been exposed to propanol, but the exact potential for the water oxidation when propenol is simultaneously oxidised cannot be determined from the CV data. The oxidation process also shows a concentration and potential dependent change in the oxidation process, progressing from independent of diffusion to show a current increase due to rotation i.e. the current became diffusion limited. It seems likely that the reaction rate of the adsorbed species involved in the process is increased above a certain potential (a second activation potential Fig. 5.5). When the concentration is low the full oxidation can proceed within the timeframe of the sweep but when the concentration is large the slow process continues well below the second activation potential at the reversed sweep. The larger adsorption energy of propenol (due to the double bond) compared to propanol increases the reaction rate beyond the second activation potential and causes the larger current at the reversed sweep.

5.2.7 Separation of the three simultaneously occurring oxidation currents

For a better understanding of the propenol oxidation on nickel containing electrodes the three oxidation reactions (oxidation of $Ni(OH)_2$, H_2O and propenol) that are all active in the same potential region (above 0.4 V) need to be separated. The information from CV on pulse plated NiZn and Ni may be sufficient to do this even though some assumptions will be necessary.

The *first* step was to determine the contribution of $Ni(OH)_2$ oxidation to the overall current. This is fairly straightforward in an electrolyte without propenol since only the second half of the oxidation peak was interfered by water oxidation as can be seen in the CV and DEMS measurements. Background currents not belonging to the redox couple were subtracted. In the presence of propenol, the charge of the NiOOH reduction peak was then used to determine the contribution from $Ni(OH)_2$ oxidation to the overall oxidation charge. In this step the reduction peak was assumed to reflect the oxidation peak in the same way as it does without propenol.

The *second* step was to separate the water oxidation from the propenol oxidation and a thorough investigation of the O_2 reduction currents (below -0.15 V), with and without addition of propenol, on Ni(pp) and NiZn was made. In a potential sweep on the pulse plated electrodes, without propenol, there is a substantial amount of O_2 produced at high anodic potentials that are reduced during the subsequent negative reversed sweep (Fig. 5.8). However, as can be seen in Figure 5.8, after the sequential addition up to 1 M of propenol, the charge from reduced O_2 is negligible. In this subtraction, the ratio between produced oxygen and reduced oxygen is assumed to be constant and independent of the propenol concentration.

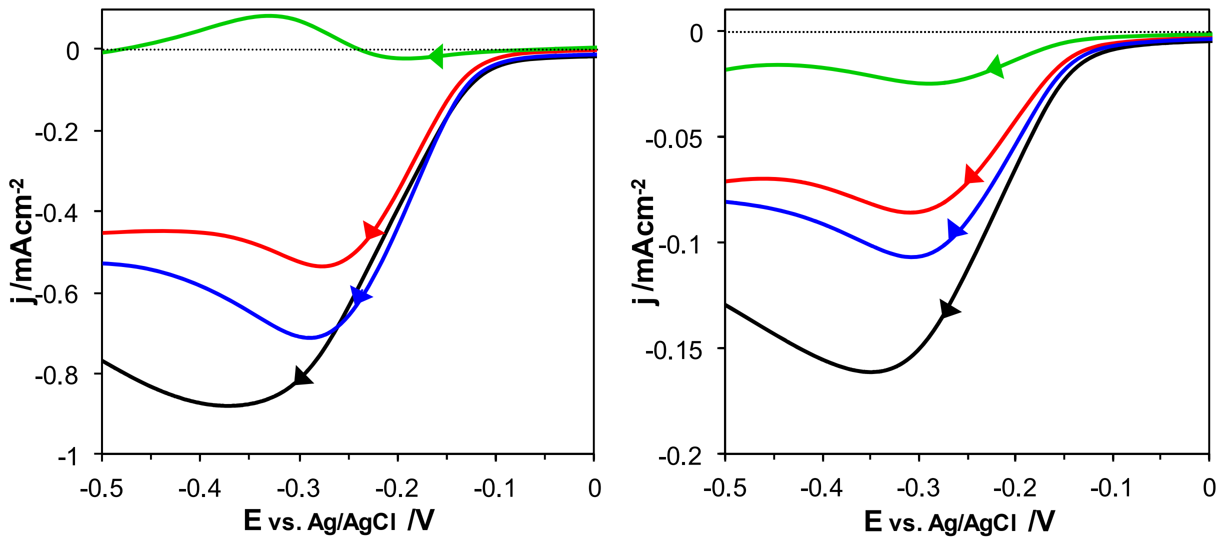

Fig. 5.8 CV in 0.1 M KOH at 10 mVs^{-1} showing the negative sweep direction only, ▬ no propenol, ▬ 0.01 M, ▬ 0.1 M and ▬ 1 M propenol. (a) NiZn on Pt disc. (b) Ni(pp) on Pt disc.

A detailed study of this phenomenon shows that if both the kinetic and diffusive contribution of O_2 reduction is included during the sweep below -0.15 V (both negative and positive sweep directions), 88% and 42% of the O_2 produced anodically is reduced cathodically on NiZn and Ni(pp), respectively. This ratio can then be used to calculate the amount of water oxidation also in the presence of propenol by the use of the oxygen reduction peak at different concentrations in relation to pure electrolyte. For these calculations the ratio of the O_2 reduction products (H_2O_2 and H_2O) were based on a previous study showing that the same Ni(pp) and NiZn alloys gave 60% and 90% H_2O_2, respectively [158].

The large amount of O_2 reduction on NiZn also indicates that the surface of the NiZn layer must differ significantly from the surface of Ni(pp) in a way that makes the oxygen stay at the surface for a longer time on the NiZn electrode. This is likely to be explained by the thicker hydroxide layer on the NiZn electrode in which the diffusing O_2 molecules are delayed compared to those formed closer to the surface.

If the NiOOH sites are assumed to be crucial for water oxidation to proceed [22] a comparison in oxidation efficiency between Ni(pp) and NiZn can be made. The potential window for water oxidation is not exactly the same for the two materials therefore the charge from the O_2 evolution was calculated during 20 s at 10 mVs^{-1} from the start of the O_2 evolution, i.e. in the following potential window 0.55→0.65→0.55 V for NiZn and 0.50→0.60→0.50 V for Ni(pp).

From a comparison based on the number of NiOOH site from charge calculation of the redox couple, the Ni(pp) electrode is the more efficient water oxidation catalyst per site by roughly 2.5 times over the NiZn electrode.

The *third* oxidation reaction, the 2e$^-$ oxidation of propenol to propenal (the product was determined in DEMS measurements, Fig. 5.10), is simply what is left of the oxidation current after the subtraction of the background, the nickel hydroxide oxidation and the water oxidation.

In the evaluation of the propenol oxidation it was observed that the reduction of NiOOH decreases linearly with the logarithm of the propenol concentration and the propenol oxidation relation is the opposite with a much larger slope. The water oxidation is not completely linear with the logarithm of the propenol concentration due to the large O_2 evolution at 0.1 M propenol, but it follows the NiOOH reduction behaviour in general terms (Fig. 5.10).

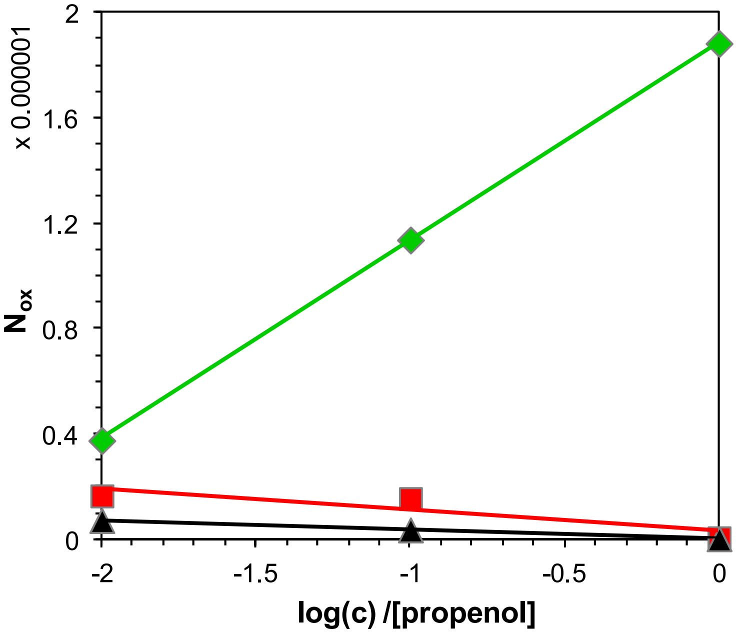

Fig. 5.9 Calculated moles of oxidised species on NiZn; ▲ NiOOH sites not ”used/consumed” in the propenol oxidation mechanism, ■ oxidised water and ◆ oxidised propenol.

The oxidation behaviour shown in Figure 5.9 indicates a site-specific behaviour, where the propenol oxidation at increased concentration occupies more and more of the NiOOH sites that are necessary also for the water oxidation. The ratio between moles of propenal produced and moles of Ni(III) sites not visible in the reduction peak ($N_{propenal}/N_{NiOOH\text{-}consumed}$) can now be calculated to be 22±1 for NiZn and 30±0.3 for Ni(pp) at all concentrations. The corresponding ratio for $N_{O2}/N_{NiOOH\text{-}not\ consumed}$ is 2.5±0.4 for NiZn and 3.9±0.7 for Ni(pp) at all concentrations. Since the number of active sites (N_{NiOOH}) is almost 5 times higher on NiZn a comparison based on number of sites is of interest and the Ni(pp) is actually 20% more effective in O_2 production and 35% more effective in propenal production per site than NiZn.

This type of calculation can of course be questioned due to the assumptions that has to be made but since detailed information about site efficiency is very difficult to obtain it may, together with other analysing techniques, generate some further understanding of this multi reaction process.

5.3 In-situ product analysis with DEMS

The purely electrochemical analysis of propenol oxidation described above does not provide enough information for a quantitative analysis of the oxidation products. The complex nature of the anodic process during propenol oxidation may be characterized in greater detail by combining cyclic voltammetry with a differential electrochemical mass spectrometry (DEMS) procedure. The mass spectrometer of this instrument characterises the products (if volatile enough, section 3.1.5) and the potentiostat reveals at what potential the products are formed.

The anodic currents and mass response of pulse plated Ni and NiZn electrodes in absence and presence of 0.1 M of propenol were characterized by DEMS and are summarized in Figure

5.10. The CV and the mass response are plotted on the same potential axis which show the potential dependence of two products observed, propenal (m/z 56◆) and oxygen (m/z 32●). The mass data were normalized to a zero baseline and smoothed.

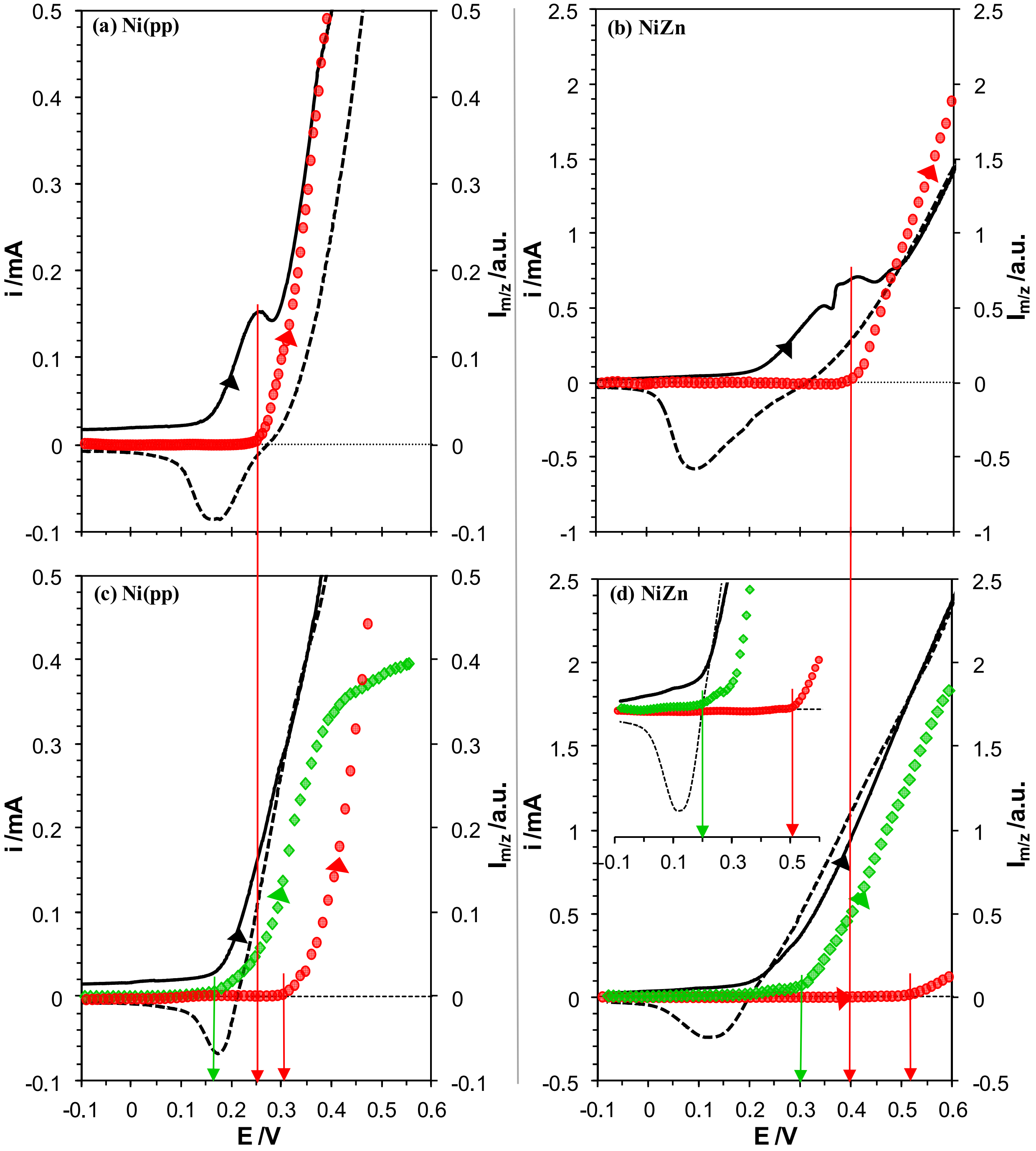

Fig. 5.10 DEMS response on Ni(pp) and NiZn in 0.1 M KOH at 10 mVs^{-1}. (a) Ni(pp) in KOH, (b) NiZn in KOH, (c) Ni(pp) in KOH and 0.1 M propenol, (d) NiZn in KOH and 0.1 M propenol. ▬ Current response (positive sweep direction), ● m/z 32 O_2, ◆ m/z 56 propenal. Positive sweep direction shown.

The first interesting observation obtained from Figure 5.10(a) and (b) shows that the O_2 evolution starts when roughly half of the electrode surface has been converted from $Ni(OH)_2$ to NiOOH. The potential difference for the onset of O_2 evolution for the two electrodes indicates that the water oxidation reaction is strongly dependent on a certain amount of pre-formed NiOOH to be able to proceed, rather than on a particular potential. This dependency indicates that water oxidation requires involvement of more than a single NiOOH site to proceed which implies a binuclear mechanism for the oxygen evolution [159-160]. Further indication of an increasing amount of sites with increasing potential was given by an increase of the Tafel slope from 60 to 150 mV from low to high overpotentials.

The addition of 0.1 M propenol gave a similar response to the CV measurements in Figure 5.2 and with two potential dependent products as reflected in the increase of abundances for fragments with mass to charge ratio (m/z) of 56, 27, 26 specific for propenal, and (m/z 32) for oxygen. The formation of the two reaction products is complemented with a decrease of the DEMS signal for propenol (m/z 57), no other products could be detected. A reference spectrum for the possible product, propenoic acid, was measured in the DEMS setup used, which showed that the acid was detectable even though the signal was rather weak, however, the CO_2 could not be detected. The desired epoxide, epoxypropane, was not detected either.

The mass response in beginning of the sweep follows the previous indications from the CV measurements with propenal formation simultaneously to the NiOOH formation. The mass response shows, however, that the O_2 evolution becomes suppressed in the presence of propenol and in addition, complementary measurements showed that the magnitude of the suppression depends on the concentration of propenol. The O_2 evolution takes off at a potential where the propenal detection starts to level out, which can be clearly seen in figure 5.10(c) but only sensed in 5.10(d). Complementary DEMS measurements to higher potentials show, however, that this is also the case for NiZn. The DEMS experiment clearly shows that the oxidation of propenol starts immediately after the first formation of the surface NiOOH which has also been seen in the oxidation of methanol on nickel hydroxide electrodes [69].

The CV experiments with a used electrode in clean 0.1 M KOH (Fig. 5.7) indicated oxidation of adsorbed species and the same experiment in the DEMS setup was made to analyse possible oxidation products (Fig. 5.11). The results showed the same oxidation products and the same oxidation pattern as with propenol in the solution but with a much smaller response. This suggests that the oxidation step is preceded by an adsorption step that is strong enough to survive several minutes on the electrode surface in a clean 0.1 M KOH solution and in fact also several sweeps, which explains the slowness of the reaction.

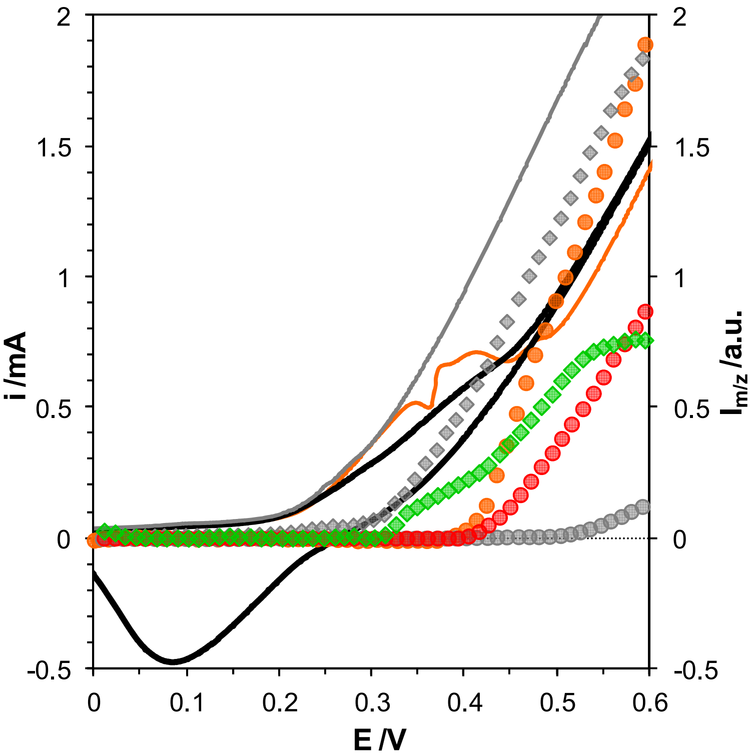

Fig. 5.11 DEMS response from a NiZn electrode previously used in propenol oxidation, the first sweep of in clean 0.1 M KOH, 10 mVs^{-1}. This measurement: — i/mA, ● m/z 32 O_2, ◆ m/z 56 propenal. *From Fig. 5.10.* Clean electrode and clean solution: — i/mA, ● m/z 32 O_2. 0.1 M propenol solution: — i/mA, ● m/z 32 O_2, ◆ m/z 56 propenal. Positive sweep direction shown.

Since the oxidation process appears different at different sweep rates (CV section) due to the slow kinetics of the reaction and the inherent time delay of the DEMS, the reaction pattern may be different at a constant potential i.e. real steady-state. To complement the picture given by the results from Figure 5.10 a constant potential step measurement in DEMS (Fig. 5.12) was performed. The potential step measurement starts at a potential where no reaction takes place (0.2 V, 240 s), stepping up to 0.4 V (240 s) where there should be only propenal response and then to 0.5 V (240 s) where both propenal and oxygen should be detected and to 0.65 V (120 s), where propenal should either decay or remain constant and oxygen production increase vigorously. The exponential decrease seen in the mass signals (Fig. 8) during the initial 500 s is due to levelling of pressure misbalances and not due to any electrochemical reaction. When the potential is stepped to 0.4 V the formation of propenal (m/z 56) is clearly observed while the signal for oxygen (m/z 32) still decreases. The production of propenal increases when going from 0.4 and 0.5 V and oxygen starts to evolve. During the last step to 0.65 V, oxygen evolution increases drastically while the propenal formation remains constant. The consumption of propenol (m/z 31) is harder to follow but small changes can be observed when propenol is oxidised. The intensity weaker intensity of the measured propenol depletion is due to differences in boiling point between propenol and propenal (97 and 53 ºC, respectively) and the vapour pressure differs by one order of magnitude.

The response from the potential step measurements connects very well to the DEMS-CV response and also confirms that the propenol oxidation continues at a constant level when water oxidation becomes the main source of the oxidation current.

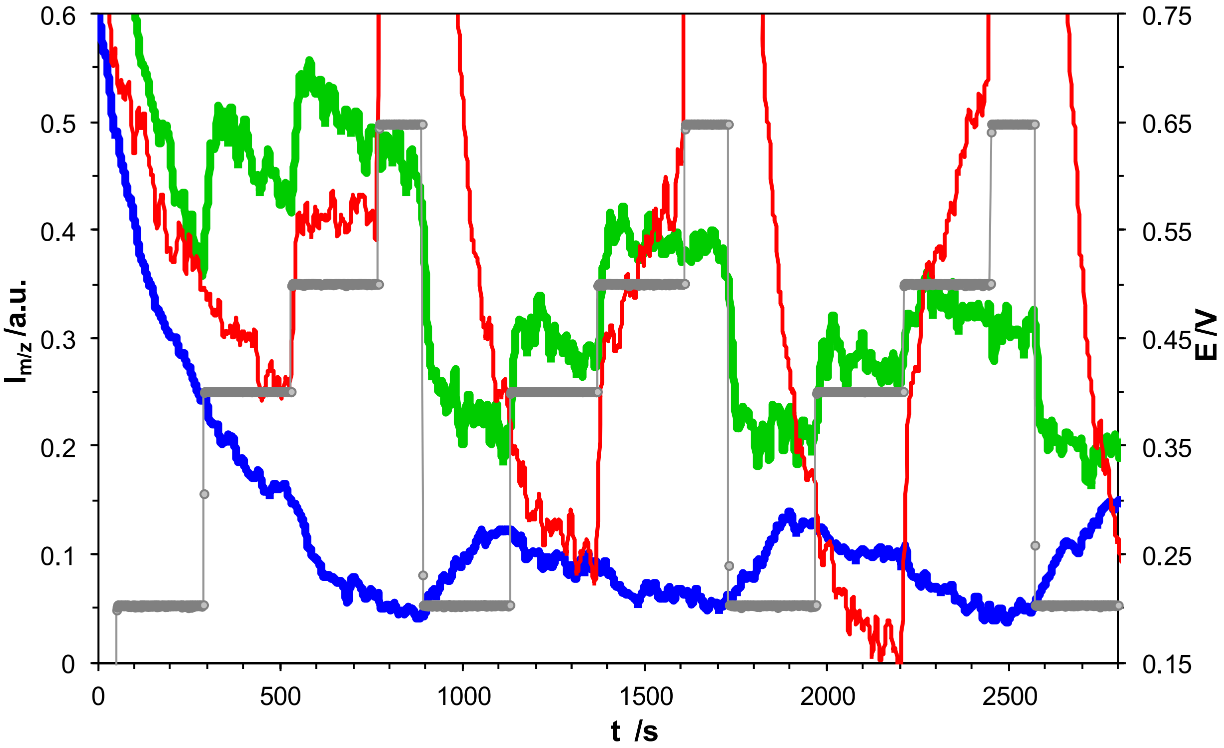

Fig. 5.12 DEMS on NiZn in 0.1 M KOH in a potential step experiment. ● E /V, ▬ m/z 32 O_2, ▬ m/z 56 propenal, ▬ m/z 31 propenol.

DEMS has to our knowledge not previously been used to investigate propenol or propanol oxidation on nickel electrodes. Propenol oxidation on other electrode materials such as platinum [161], palladium [162] and gold [163] has, however, been studied in DEMS in acid electrolyte in which aldehyde and various amounts of CO_2 were detected. Oxidation of other alcohols on nickel electrodes in alkaline electrolyte has previously been studied with CV complemented with product detection from bulk products analysed by gas chromatography [60-61] or by in-situ infrared spectroscopy [64]. The products measured by those methods were mainly the acid with some CO_2/carbonate at higher over potentials. It is, however, not possible to detect propenal from bulk chromatography in strong alkaline solution due to the rapid polymerization of propenal under these conditions.

Due to the reported oxidation of propen to propen oxide (epoxide) on both nickel and steel in alkaline solution [149-150, 152] this reaction was also investigated in DEMS. The CV for propen did not show any electrochemical reaction (section 5.1) and to eliminate the possibility of a chemical reaction by for example contamination by chromium from a steel cell, 0.1 M K_2CrO_4 was added in an experiment with a 316 steel electrode. Propen oxide was, however, not detected in any of the DEMS experiments made, with our without chromium.

5.4 Reaction Mechanism for NiOOH catalysed propenol oxidation

In analogy with previous studies [60-61] a redox mediated mechanism is suggested for propenol oxidation including an intermediate formation of a surface nickel ester.

1. Oxidation of nickel (II) hydroxide

$$\overset{II}{Ni}(HO)_2 + OH^- \rightarrow \overset{III}{Ni}OOH + e^- + H_2O \tag{E 5.1}$$

2. Adsorption of propenol by charge transfer between the alcohol and the surface group.

$$\overset{III}{Ni}OOH + RCH_2OH \rightarrow HOO\overset{II}{Ni}-\overset{\oplus}{O}HCH_2R \tag{C 5.2}$$

3. Formation of an intermediate surface ester.

$$HOO\overset{II}{Ni}-\overset{\oplus}{O}(H)CH_2R \rightarrow_2 (HO)\overset{II}{Ni}-OCH_2R \tag{C 5.3}$$

4. Oxidation of the intermediate.

$$(HO)_2\overset{II}{Ni}-OCH_2R + OH^- \rightarrow HOO\overset{III}{Ni}-OCH_2R + e^- + H_2O \tag{E 5.4}$$

5. Formation of the oxygen-carbon double bond and release of a proton, which will be incorporated in the $Ni(OH)_2$ structure. This step closes the redox cycle in Figure 5.13.

$$HOO\overset{III}{Ni}-OCH_2R \rightarrow \overset{II}{Ni}(HO)_2 + RCHO \tag{C 5.5}$$

The five step nickel redox mediated mechanism is also illustrated in Figure 5.13 and the complexity of this suggested mechanism may well explain why the current response depends so much on both the sweep rate and the propenol concentrations, but is not explained by any model based on diffusion or a simple adsorption isotherm.

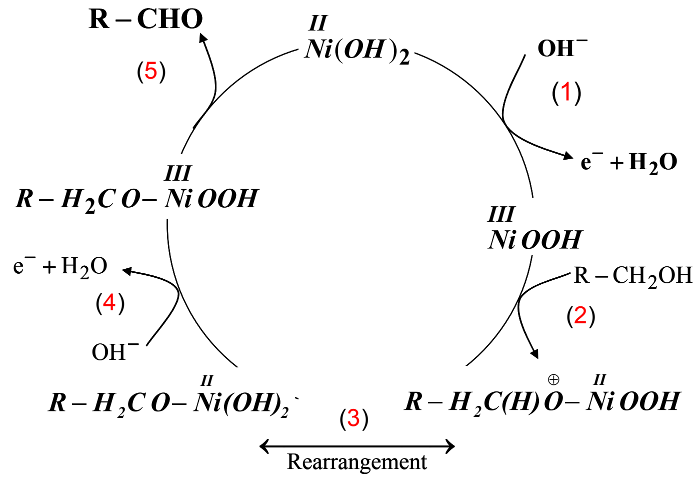

Fig. 5.13. Suggested redox cycle for propenol oxidation on oxidised nickel.

5.5 Conclusions

- The pulse plated NiZn electrodes show a considerable larger redox current from $Ni(OH)_2$ /NiOOH compared to the geometrical equal Ni(pp) and Ni(s) electrodes which also generated a larger oxidation current in the presence of propenol.
- Separation of the three simultaneously occurring oxidation currents ($Ni(OH)_2$, water and propenol oxidation) in CV shows that Ni(pp) is the more efficient catalyst over NiZn per NiOOH site, for both water and propenol oxidation. This is likely due to the difficulties for the propenol to penetrate deep in the thicker NiZn hydroxide.
- DEMS measurements show that water oxidation needs a surface half covered with NiOOH to proceed. Oxidation of propenol starts immediately at the first formation of NiOOH and the oxygen evolution is hindered in its presence. Oxygen evolution, however, does proceed but at a more positive potential and appears to be connected to when the propenol oxidation reaches its maximum value for a specific concentration.
- The DEMS result for the O_2 evolution indicates a binuclear water oxidation mechanism.
- The only oxidation product of propenol found in the DEMS analysis was its corresponding aldehyde, propenal. No propen oxidation could be detected during potential sweep analysis, electrochemically (CV) or chemically (DEMS).
- Sweep rate experiments with and without rotation indicated a complex surface confined reaction mechanism that changes from diffusion independence to certain diffusion dependence at high overpotentials. A reaction mechanism governed by the formation of NiOOH is suggested in analogy with previous studies on other alcohols.
- No Propen oxidation could be detected by CV or DEMS, neither on NiZn or on steel.

6 NiO, CoO and $Ni_{1-x}Co_xO$ in carbon paste electrodes

6.1 Background

This chapter treats the work in paper IV which was made within the frame of a European collaboration network, "Clean Technologies for Peroxide Generation" (CLETEPEG). The task for this project was to improve the development of H_2O_2 production by electrochemical O_2 reduction in smaller units, preferably based on fuel-cell technology for co-generation of chemicals and energy.

In the search for a catalyst suitable for an electrochemical on-demand H_2O_2 production plant (further discussed in Section 2) NiO, CoO and $Ni_{0.75}Co_{25}O$ were investigated using the RRDE technique. The oxygen reduction properties of nickel and cobalt oxides have been investigated previously [164-168] and as long as mixed oxidation states of the oxide is avoided, the $2e^-$ reduction to H_2O_2 appears to prevail [164]. The goal for this particular investigation was, however, to investigate the effect of the oxides themselves, without the influence of its metal substrate. This can be a troublesome task for two reasons; the oxides are only semiconducting, which implies that thicker layers made with for example sputtering would generate an electrode with very large resistance. Secondly the brittleness of the oxides makes them unsuitable for the metalwork necessary to produce a RDE. For these reasons carbon paste (CP) was chosen as a matrix for the oxides and by mixing the oxides with CP, the two problems outlined above could be circumvented. The benefit with carbon is that the overpotential for H_2 and O_2 evolution becomes large and it does not have any redox couple, which provides a large potential window for other reactions to be studied. There may, however, be functional groups formed on all carbon surfaces that can influence the measurements to various extents. Even though carbon paste electrodes (CPE) were introduced by R.N. Adams already in 1958 [169] only a few studies have been made using CPE in O_2 reduction analysis [89, 170-171] and even fewer characterisation studies of nickel- and cobalt oxide species have been undertaken [172]. The reason for this may be the inherent difficulties in the stability and the impact of the binder that may give the results an uncertainty factor larger than those found for solid electrodes [173]. However, when it comes to materials unsuitable for electrode fabrication CPE provides a unique window for electroanalysis of such materials.

6.2 Synthesis and characterisation of $Ni_{1-x}Co_xO$

The CoO and $Ni_xCo_{1-x}O$ were synthesized by mixing $Co(OH)_2$ and NiO (Puratronic®, 99.998 %) in molar ratios and mortared into the appropriate mixtures (1:4, 1:1, 4:1). The mixtures were sintered at 1000 °C for 14 h and were left to cool at room temperature. The $Co(OH)_2$ was prepared from $Co(NO_3)_2$ that was added to a 1 M NaOH solution at constant stirring for 1.5 h. The precipitate was then washed, filtered and dried in a desiccator. Pure $Co(OH)_2$ was detected using x-ray analysis. The sintered Ni and Co mixed oxides were analysed by x-ray powder diffraction and 10 mol% Si was added to the samples as an internal standard for 2θ correction. A sample of a simple mixture of the pure NiO and CoO (1:1) was also measured as a reference for the pure oxides. The X-ray analyses clearly show that the mixed oxides form pure solid solutions of $Ni_xCo_{1-x}O$ follow Vegards law (Fig.6.1), as previously shown by Holgersson et al. [174].

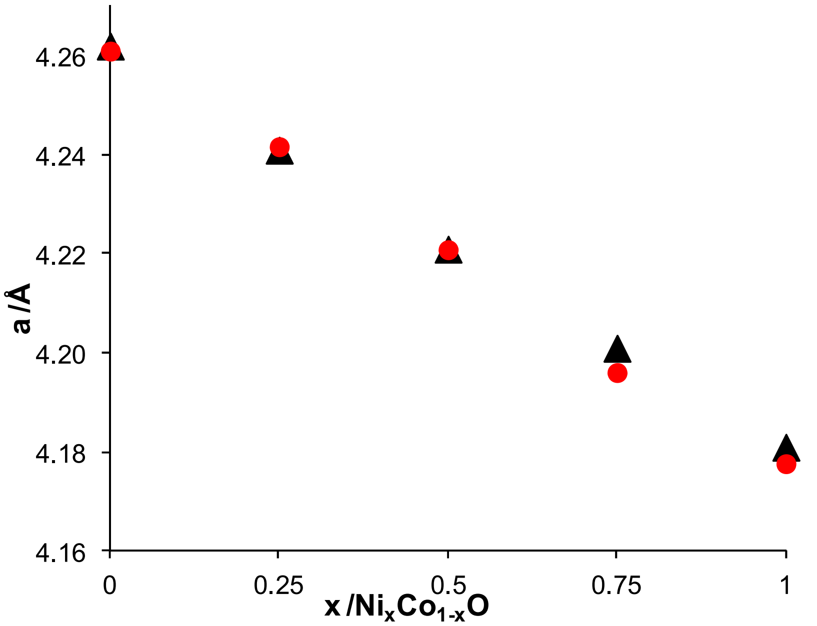

Fig. 6.1 (●) Experimental lattice constant **a** compared with (▲) reference [174] value.

6.3 Preparation of carbon paste rotating ring disc electrodes

The CP-RRDE was constructed with a gold ring moulded in epoxy and a cavity milled into the epoxy in the centre of electrode, which was filled with a conducting material to form the disc. The area of the disc space was 0.076 cm^2 and a theoretical collection efficiency (N) was determined to be 0.37 [91]. The cavity of the disc was filled and packed tight with a standard manufactured carbon paste from Metrohm (CP). After packing, the excess carbon was smoothen off by a Teflon® ruler, the gold and epoxy areas were cleaned carefully with ethanol soaked tissues and finally, the disc was compressed once more with a hand-press. The electrode was then cleaned again and checked under microscope to control contamination of the ring and that the disc surface was at the same level as the surface of the electrode. The oxide powders were weighted and mixed with carbon paste by mortaring. The disc compositions are named and presented in Table 6.1. When the mixed carbon electrodes were prepared, 0.6 mm of the top layer of the CP was carved off and replaced by the CP-oxide mixture and prepared as the pure CPE described above.

Table 6.1 Disc materials in the CP-RRDEs

Electrode	Disc: (wt)% oxide in CP
CPE/100%	0
CPE/33%NiO	33
CPE/67%NiO	67
CPE/67%$Ni_{0.75}Co_{0.25}O$	67
CPE/67%CoO	67

Background currents (currents not belonging to the ORR) were compensated for by subtracting a measurement in N_2 saturated electrolyte from the corresponding measurement in O_2 saturated electrolyte. More advanced treatments of the background currents were necessary for CPE/67%NiO and CPE/67%CoO and this procedure is further discussed in paper IV.

6.4 Oxygen Reduction

All the electroactivate CPEs (Table 6.1) were cycled in the same potential region starting from 0 V to -1.4 V (vs. Ag/AgCl). Limitations in the negative region (-1.2 V) was, however, necessary for the cobalt containing electrodes due to the reduction of Co(II) to Co and the massive H2 evolution. Several current corrections were necessary due to redox activity arising from the oxides, which are explained in detail in the experimental section in paper IV. A typical voltammogram from CPE/67%NiO RRDE showing the rotations from 600 to 3000 rpm is presented in Figure 6.2. A small change of both the disc and the ring currents between the first and the last sweep can be seen, leading to a slight change (1 - 5%) in the percentage of H_2O_2 produced from each O_2 molecule.

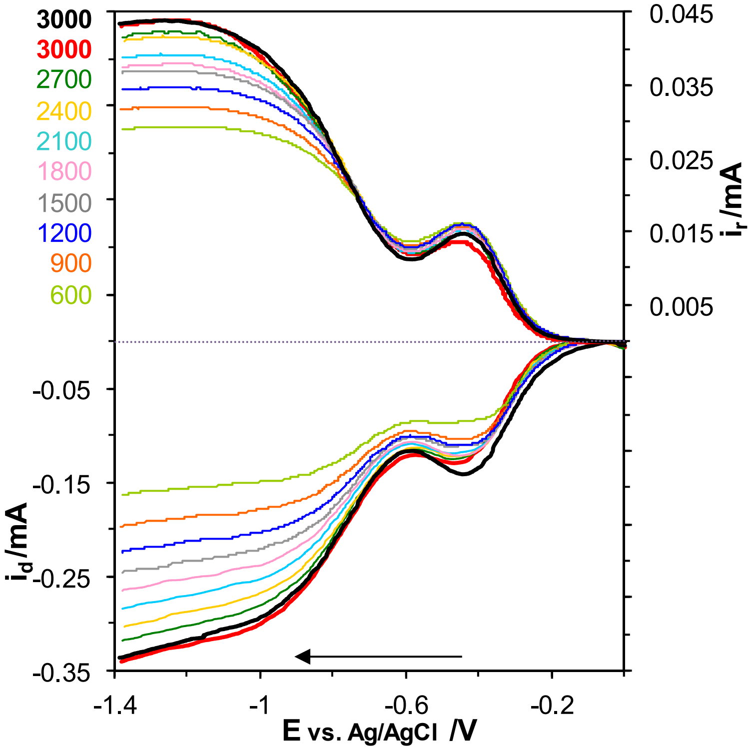

Fig. 6.2 RRDE experiment with CPE/67%NiO in O_2 saturated 0.1 M KOH at 10 mVs^{-1}, the rotation rates (600-3000 rpm) are given in the figure. ▬ First sweep 3000 rpm and ▬ last sweep 3000 rpm.

The measurements at 1200 rpm were chosen for all evaluations since the potential sweeps were stabilising the electrode and the 1200 rpm run was in the middle part of the sequence. Secondly, the slightly rotation dependent collection efficiency (determined in a collection efficiency experiment) was closest to the theoretical value at 1200 rpm for all the electrodes.

Figure 6.3 shows the voltammetry for all the disc materials of this study at 1200 rpm. From the CPE/100% (a) curve it can be seen that there is a two-wave process coupled to oxygen reduction, one process that generates a peak at -0.45 V and a second process that starts approximately at -0.6 V then rising towards a diffusion limited current plateau. The corresponding ring current shows that O_2 is reduced to H_2O_2 to some extent in the whole potential region, which can be expected from any carbon electrode in alkaline solution.

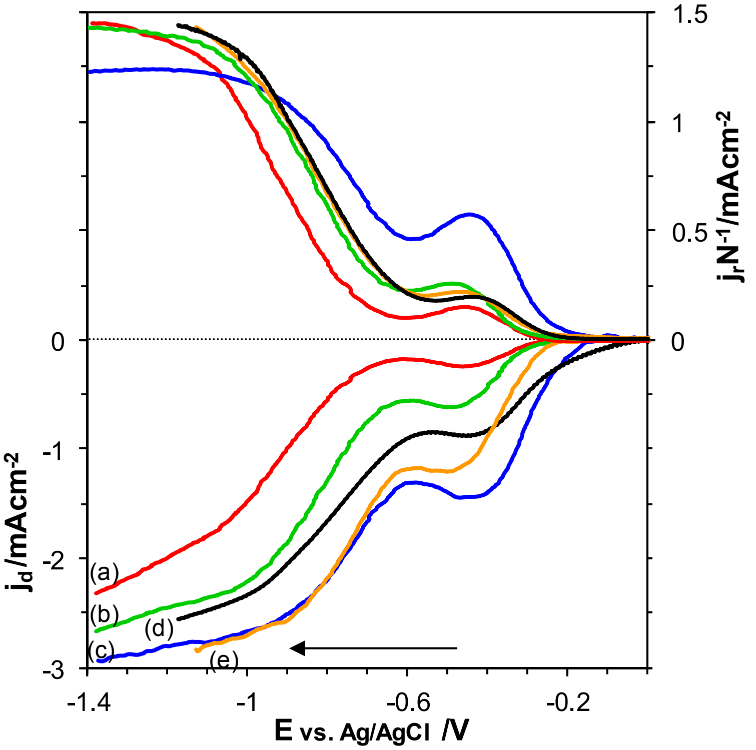

Fig. 6.3 RRDE experiment in O_2 saturated 0.1 M KOH, 10 mVs^{-1}, 1200 rpm: (a) 🟥 CPE/100%, (b) 🟩 CPE/33%NiO, (c) 🟦 CPE/67%NiO, (d) ⬛ CPE/67%$Ni_{75}Co_{25}O$, (e) 🟧 CPE/67%CoO

The important observation from Figure 6.3 is that the current increases substantially when the carbon paste is mixed with a metal oxide and the more oxide produced the larger the increase in current. The properties of the oxide also matters since CPE/67%NiO generates the largest current increase at the first wave compared with CPE/67%CoO and CPE/67%$Ni_{0.75}Co_{0.25}O$. The second wave is equally activated by both CoO and NiO, the mixed oxide is, however, slightly less activated than the pure compounds. At the first wave the CPE/67%NiO produces the same current at 200 mV less negative potential compared to the current at the peak potential of CPE/100%. The corresponding decrease of the overpotential for the ORR at the second wave right after the minimum between the two processes is 350 mV.

To be able to compare how efficient the catalysts are to convert O_2 into H_2O_2 the currents in Figure 6.3 were converted into percentage H_2O_2 produced from each unit of O_2. This was calculated from equation 3.12 and the result is shown in Figure 6.4, in which also the number of e^- transferred is indicated (Eqn. 3.13). The results from this comparison suggest that the pure CP converts roughly from 80% of the O_2 reduced to H_2O_2 and that the addition of 67% NiO lowers the conversion to 60%. The % H_2O_2 at two potentials for all the electrodes is tabulated in Table 6.2.

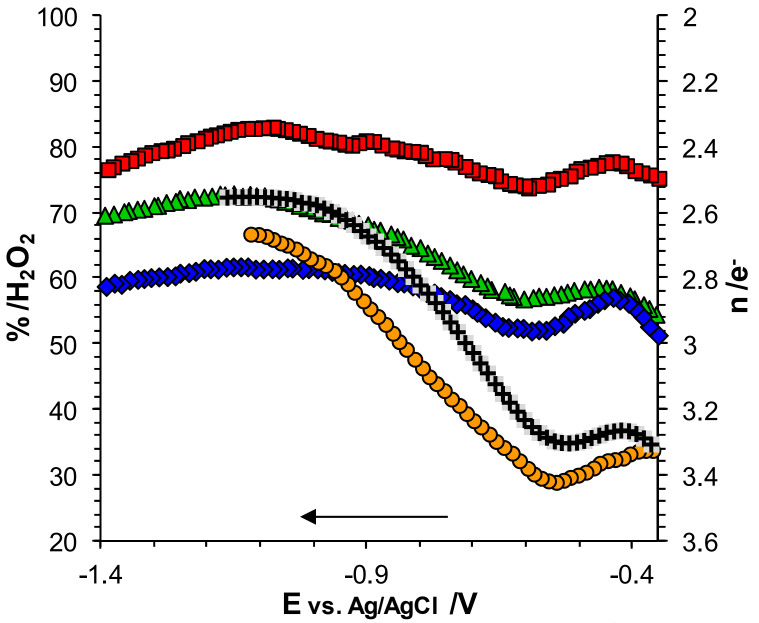

Fig. 6.4 RRDE experiment in O_2 saturated 0.1 M KOH, 10 mVs^{-1}, 1200 rpm: ■ CPE/100%, ▲ CPE/33% NiO, ◆ CPE/67% NiO, + CPE/67% $Ni_{75}Co_{25}O$, ● CPE/67% CoO.

The large potential dependent change in reduction path (for reduction paths se Fig. 2.5) for cobalt containing electrodes differ quite drastically from the pure CPE and the CPE/NiO electrodes and the change is made by as little as 25% Co in the NiCo oxide matrix. Another mixed oxide electrode, CPE/67% $Ni_{50}Co_{50}O$, was run under the same conditions and confirmed the overall results of CPE/67% $Ni_{75}Co_{25}O$. A different electrode geometry was, however, utilized in this experiment but some uncertainty factors prevented a detailed study of the CPE/67% $Ni_{50}Co_{50}O$ results and the results are subsequently not further discussed.

The reduction peak and the reduction wave in Figures 6.2 and 6.3 originate from the carbon and can be seen in virtually any ORR experiment with carbon electrodes in an alkaline electrolyte. The first process is believed to be controlled by quinones that are always present at a carbon surface and similar effects has also been seen for electrodes grafted by different types of quinones [175-178]. The current maximum is followed by a current minimum creating a peak, despite the rotation of the electrode. This phenomena has been suggested to be caused by a change in the activity of the surface sites on the quinones due to the potential changes in the sweep ($Q \rightarrow Q^{-}_{active} \rightarrow Q^{2-}$) [177]. The second wave follows the path of an ordinary activated electron transfer process and approaches a diffusion limited current for oxygen reduction.

It has been shown that mixing dry graphite with any pasting liquid lowers the electron transfer rate as well as the residual current. It can be concluded that the longer chain the liquid consist of the lower the electron transfer rate will be [173]. Mixing the CP with metal oxides may be regarded as dilution of the pasting liquid but also as a dilution of carbon with reduced number of quinones available for the ORR. The reduced area of quinones and the dilution of the carbon paste with different oxides giving different response at the first wave, strongly indicate that the increase of the rate constant is due to the properties of the oxides and is not due to an effect of dilution of the binder.

Figures 6.3 and 6.4 show two different pictures of the ORR efficiency and in Figure 6.3 the overpotential needed for a certain current to pass is presented and in Figure 6.4 the % H_2O_2 from each unit O_2 is viewed. The optimum electrode material from these two properties will depend on the price of the reactant (as e.g. 40% of the reactants in the use of a CPE/67% NiO go to water), the price of energy consumption and the price of the electrode material. The energy consumption will increase with increased overpotential and decrease with increased % H_2O_2 produced (since every $4e^-$ reduction to water is a waste of energy, if not a fuel-cell setup is used). A catalyst must of course be durable and have a reasonable price for long term use in large scales. It is for the reasons above, not possible to claim which catalyst is the best in a practical application but a reduction of the high overpotential on carbon electrodes is apparently of fundamental importance in any application of O_2 reduction.

6.5 Simulation of the ORR and mechanism suggestion

6.5.1 Simulation of experimental data

Since the observed two waves in Figures 6.2 and 6.3 are likely to be caused by two different processes, it would be beneficial to interpret them separately. In order to separate the two processes at least one of them has to be simulated and then subtracted from the experimental data. The second wave has the shape of an ordinary activated electron transfer process and can be simulated by the addition of the kinetic current (Eqn. 3.16) to the limiting current (Eqn. 3.14) arranged as in the Koutecky´-Levich (K-L) equation (Eqn. 3.15) [91]. When a perfectly smooth and homogeneous RDE is used, a K-L plot (i^{-1} vs. $\omega^{-½}$) extrapolated to infinite rotation speed at high overpotentials should give zero value ($i^{-1} = 0$) at origin, if the current is purely diffusion controlled. Deviation from origin in such a plot indicates that other unexpected processes contributes to the current, the contribution may come from potential dependent kinetics and/or a deviation from electrode geometries that the K-L equation does not account for. If the O_2 reduction process is going to be simulated, an irreversible $4e^-$ transfer with the first e^- transfer as the rate determining step has to be assumed. For comparable limiting currents between the experimental and the simulated data a complete $4e^-$ reduction to water by the experimental data has to be used, made possible by taking $i_{(4e-)} = |i_d| + |i_r/N|$ (Eqn. 3.9-10). In this way the O_2 molecules reduced by $2e^-$ only were counted a second time when the H_2O_2 was oxidized by $2e^-$ at the ring.

The liming currents for all the electrodes were, however, quite heavily suppressed compared to the ones predicted by Eqn. 3.14, which are shown in Figure 6.5(a) where the theoretical curves are represented as dotted lines and the experimental curves are shown as coloured dashed lines. The current abnormities were also reflected in the K-L plot (Fig. 6.5(b)) as large deviations from zero at origin for all the electrodes, the largest deviation from zero was shown for CPE100% and the smallest for CPE/67%NiO, and all the others where in between.

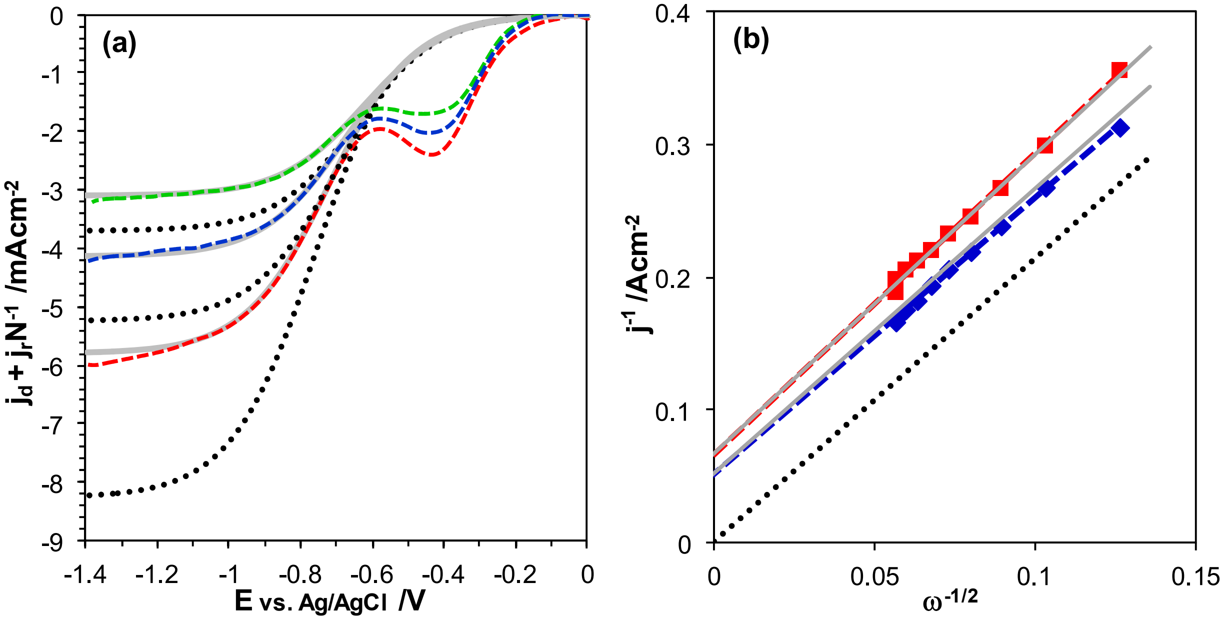

Fig. 6.5 Simulated and experimental voltammogram for the ORR, •••IRET, ▬ Recessed IRET. (a) CPE/67%NiO at --- 600, --- 1200 and --- 3000 rpm. (b) K-L plot 600-3000 rpm, ◆ CPE/67%NiO and ■ CPE/100%.

Similar current issues have previously been encountered in the evaluation of the current effects of Nafion films on Pt electrodes [179-180] and on partially recessed and porous electrodes [147]. In those models an additional current factor was added to the K-L expression for an irreversible electron transfer as shown in Eqn. 6.1 and a similar approach was used in this work.

$$i^{-1} = i_k^{-1} + i_{cp}^{-1} + i_D^{-1} \tag{6.1}$$

The correction factor in here was denoted i_{cp} and was subsequently obtained from the intercept of a K-L plot at the diffusion limiting current plateau (Fig. 6.5(b)). CPEs should not be porous but they do contain a hydrophobic binder that may create some heterogeneity at the surface that resembles a recessed electrode but the physical meaning of i_{cp} in this case has, however, not been further evaluated. Even though the trend is not very strong the intercepts in figure 6.5(b) show that i_{cp} increase with the addition of oxide.

After the correction factor for the limiting currents had been added the simulation proceeded by adjusting α and k in Eqn. 3.14 until an acceptable fit in the mixed kinetic and diffusion limited region (region i_k+i_l in Fig. 3.3) of the second process was reached (grey curve in Fig. 6.5(a) and (b))). The separation of the first and second processes could then be made by subtracting the simulated current from the experimental current (Fig. 6.6) and hence the first peak could be isolated (Fig. 6.6 *inset*).

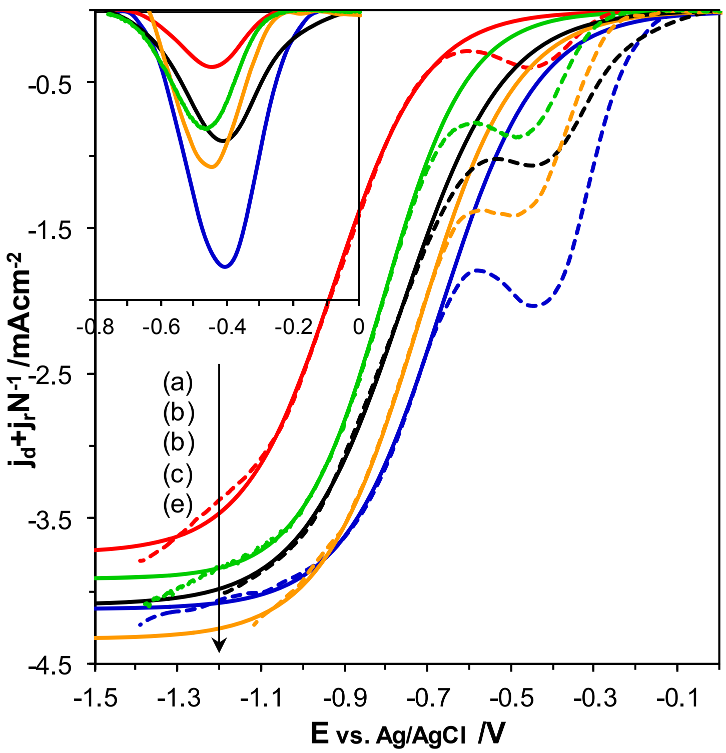

Fig. 6.6 Experimental ORR voltammograms (dashed lines) compared with simulated recessed IRET data (solid lines). (*inset*) The separated first process. 1200 rpm: (a) 🟥 CPE /100% CP, (b) 🟩 CPE/33% NiO, (c) 🟦 CPE/67% NiO, (d) ⬛ CPE/67% Ni$_{75}$Co$_{25}$O, (e) 🟧 CPE/67% CoO.

When the charge of the first process is plotted as a function of rotation it can be realized that rotation dependence only exists for the electrodes with a high content of oxide (Fig. 6.7).

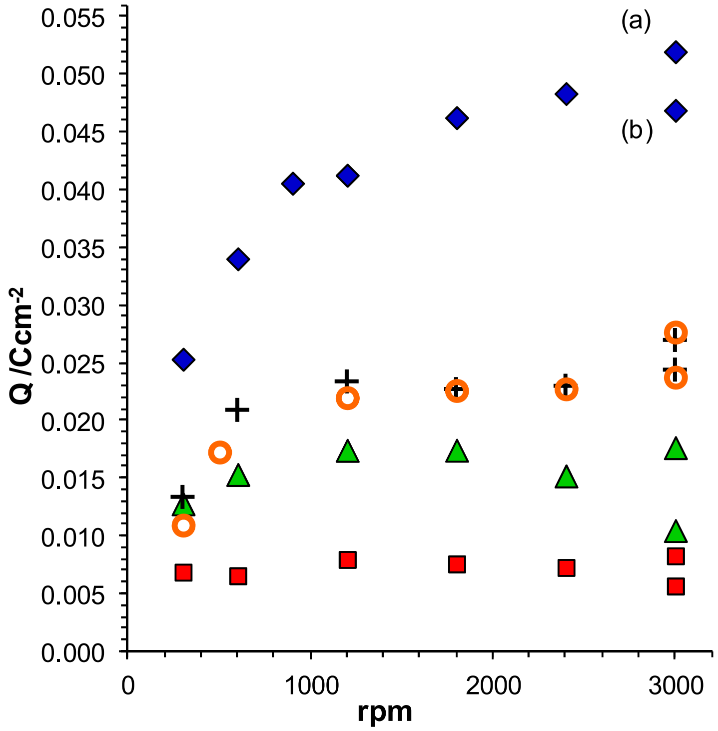

Fig. 6.7 Charge of the separated first peak shown in Fig. 9, 1200 rpm and negative sweep direction shown: ■ 100% CP; ▲ 33% NiO; ◆ 67% NiO; + 67% $Ni_{75}Co_{25}O$; ○ 67% CoO. (a) Last sweep and (b) first sweep.

The rotation dependence appears to be stronger at lower rotation rates but is not very well defined, partly due to the inherent time dependence, which generates a charge increase with the number of experiments undertaken on the electrode (Fig. 6.2). The charge increases from the first to the last 3000 rpm sweep is 16 ±1% for the 67% oxide containing electrodes. With the random experimental procedure of the rotation rates used, it is not possible to show how this time dependent charge increase affects each rotation rate from the first to the last run, the main change is, however, believed to occur between the first and second sweep.

The charge of the separated first peak increased by 5-6 times at 600-3000 rpm when 67% NiO was added to the CP and by 2 times when 33% NiO was added. The addition of Co containing oxides increased the first peak by around 3 times at 3000 rpm (Table 6.2).

Simulations of the ORR at the second process using the recessed model (Eqn. 6.3) gave an average transfer coefficient (α) between 0.210 and 0.255 for the various electrodes. The rate constant (k) increases with increasing amount of oxide mixed in the CP and the largest increase can be seen for the CPE/67%NiO, whose rate constant is 25 times higher than for the CPE/100% (Table 6.2). The following transfer coefficient and rate constant for oxygen reduction at the corresponding conditions have previously been reported on glassy carbon in 0.1 M KOH; $\alpha = 0.20\pm0.01$ and $k = 6\cdot10^{-4}\pm1$ cms^{-1} [175], and for carbon paste electrodes; α between 0.5 and 0.7 and k from $5\cdot10^{-5}$ to $6\cdot10^{-4}$ [171].

Table 6.2 Tabulated values related to Fig. 6.4 and 6.6 and *k* and *α* used in the simulations.

Electrode	% H_2O_2 at two potential regions [a]		Simulated *k* [b]	Simulated α [b]	Q, separated first peak [c]
	-0.43 V	-1.15 V	*k* (cms^{-1}) [b]	α [b]	Q (Ccm^{-2})
CPE/100%	78	83	$4.3\cdot10^{-7}$ ±1.0	0.240±0.006	$8.0\cdot10^{-3}$
CPE/33%NiO	58	72	$7.3\cdot10^{-7}$ ±0.7	0.255±0.001	$1.7\cdot10^{-2}$
CPE/67%NiO	57	62	$1.1\cdot10^{-5}$ ±0.08	0.220±0.003	$4.1\cdot10^{-2}$
CPE/67%$Ni_{0.75}Co_{0.25}O$	37	72	$7.0\cdot10^{-6}$ ±0.07	0.210±0.000	$2.3\cdot10^{-2}$
CPE/67%CoO	33	66	$6.9\cdot10^{-6}$ ±0.5	0.220±0.003	$2.2\cdot10^{-2}$

[a] 1200 rpm, Fig.6.4. [b] Average for 600-3000 rpm. [c] 1200 rpm, Fig. 6.6.

p-factor analysis was made for the values of k and α for all rotations which showed significant differences between all electrodes except between CPE/67%Ni0.75Co0.25O and CPE/67%CoO for k, and between CPE/67%NiO and CPE/67%CoO and between CPE/33%NiO and CPE/100% for α

6.5.2 Mechanism of the quinone mediated ORR enhanced by Ni and Co oxides

Several investigations have previously been made on quinone functionalised GC and OPG electrodes and its catalytic effect on O_2 reduction [83-84, 175, 177]. A common suggestion is that it is the natural quinone groups that increase the O_2 reduction at the first wave. The following reaction mechanism has been proposed [177].

$$Q + e^{-} \rightarrow Q^{\bullet -} \tag{6.4}$$

$$Q^{\bullet -} + O_2 \rightarrow Q{-}O_2^{\bullet -}{}_{(ads)} \tag{6.5}$$

$$Q{-}O_2^{\bullet -}{}_{(ads)} + H_2O + e^{-} \leftrightarrows Q + HO_2^{-} + OH^{-} \tag{6.6}$$

Q would in this case represent the natural quinones on the carbon surface where either (6.4) or (6.5) could be the rate determining step. The presence of quinone radicals ($Q^{\bullet -}$) in the potential range of the first wave is necessary for this mechanism to be valid and calculations [177] indicate that the coverage of $Q^{\bullet -}$ do follow the shape of the first peak.

The increase of the first wave with increasing amount of oxide in a CPE has to our knowledge not been shown previously. The explanation for such an increase may be found in the redox activity of the hydrated oxides since the outer layer of the NiO and CoO will be transformed into $Ni(OH)_2$ and $Co(OH)_2$ in alkaline solution. If the $O_2^{\bullet -}$ is oxidising enough to subtract an electron and a proton from the hydroxide the third step (6.6) in the mechanism proposed by Yeager [177] may then be exchanged by (6.7).

$$Q{-}O_2^{\bullet -}{}_{(ads)} + Ni(OH)_2 \rightarrow Q + NiOOH + HO_2^{-} \tag{6.7}$$

At the potential for HO_2^- formation NiOOH will immediately be reduced

$$NiOOH + e^{-} + H_2O \leftrightarrows Ni(OH)_2 + OH^{-} \tag{6.8}$$

and again be available for the next superoxide ion. Xu et al. [178] propose by their isotope investigation of the ORR on GC in alkaline solution that the protonation of the $O_2^{\bullet-}$ is a crucial step in alkaline solution since the e^- and the H^+ transfer should be similar in rate. The conclusion of Xu fits well with the mechanism proposed here, where the e^- and the H^+ has to be released simultaneously from the $Ni(OH)_2$ in reaction (6.7). The suggested reaction pathways are schematically presented in Figure 6.8.

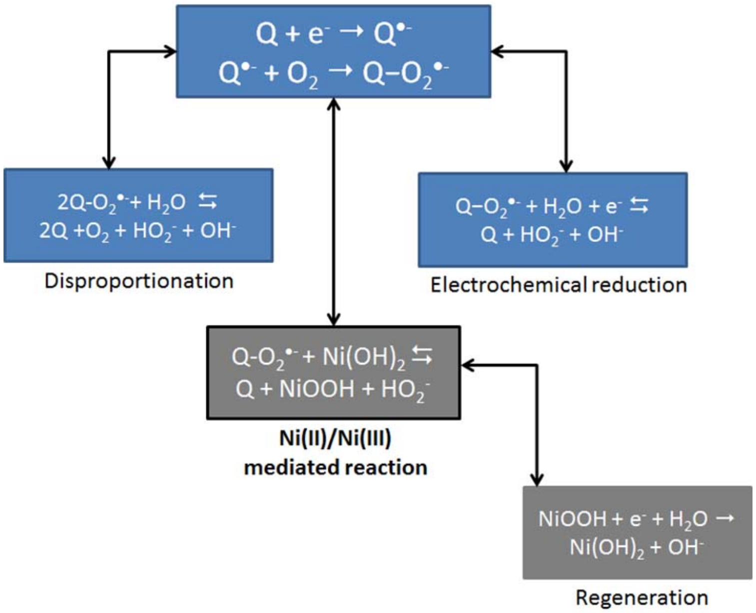

Fig. 6.8 Schematic presentation of the ORR of the first process at -0.4 V.

The corresponding mechanism should be valid also for CoO even though the CoOOH is less prone to be reduced, which may slow the reaction down.

Reaction (6.8) on a metal electrode has a redox potential at -0.4 V in the corresponding setup, but as can be seen in Figure 3 in paper IV there are residual currents from the redox couple below 0 V. The literature concerning electrochemical properties of thicker layer of NiO and CoO without its metal support in alkaline electrolyte is sparse, but a few publications have presented and discussed recorded voltammetry of NiO in other solutions [12, 181-183]. The voltammetry of µm thick NiO SnO_2:F coated glass in the paper by Gibson et al. [12] at pH 5.5 differs quite substantially from the one expected from Ni metal [184]. If the potential from the redox of the NiO layer in [12] is adjusted to 0.1 M KOH (reaction (6.8) is pH dependent by 60 mV/dec), this redox response will overlap with the response seen between 0 and -0.4 V in paper IV (Fig. 3 curve b). By this consideration it appears as the CP environment of NiO facilitates the oxidation of $Ni(OH)_2$, then also making it easier for the superoxide radical to subtract an electron from its neighboring $Ni(OH)_2$.

6.6 Conclusions

- The use of CP-RRDEs for investigation of the ORR on metal oxide powders is possible and even if the results are not as straight forward to interpret as on an ideal RRDE, important insight into the properties of the oxide and the reaction kinetics can still be obtained.
- Mixing Ni and Co oxides in CP reduces the overpotential for the ORR compared to pure CP, however, both oxides induce a higher degree of $4e^-$ reduction to water. Also, even a small amount of Co oxide induces a different potential dependent reduction pathway compared to the pure Ni oxide.
- The ORR in the first and second processes, seen for many carbon electrodes in alkaline solution, was separated by simulation of the second process. In the simulations a third current component (i_{cp}) was added to the K-L equation to account for the non-ideality of the experiments.
- The charge for the peak at the separated first process increased by 5 times when 67% NiO was added to the CP.
- The rate constant k for the ORR at the second process increased by 25 times when 67% NiO was added to the CP, k was, however, still lower than on pure GC, which could be expected due to the binder, α was in the range of 0.2 which is similar as for GC.
- It is suggested that the $Ni(OH)_2$/NiOOH redox couple participates and enhances the ORR though coupling between the this redox couple and inherent quinone groups on the carbon paste surface.

7 Conclusions and further perspective

7.1 Conclusions

The catalytic properties of Ni with foreign metals in the Ni matrix have been investigated for the oxygen reduction reaction (ORR), propenol oxidation in alkaline environment and proton reduction in pH 2.8. The main focus has been on the improvement of Ni based catalysts for O_2 reduction to H_2O_2 in alkaline environment.

A novel type of Ni rich NiZn alloys were produced by pulse plating under anomalous deposition of Ni and Zn in a sulphate electrolyte at pH 2.8. The alloys were seen to grow in isolated 3D clusters with substantial height before the surface became completely covered. SEM images of the fully plated surface showed that the surface was build up by semi-spherical particles in the 100 nm range on which 10 nm particles had started to grow. EDX measurements showed a Ni-rich alloy of Ni_xZn_{1-x} where x is between 0.14 and 0.21 depending on plating conditions. The long range order of these alloys was not possible to determine since only a single diffraction peak, shared by both Ni and Zn, was clearly observed. The possible short range order (e.g. nanocrystallinity) was investigated by XAFS, which showed that the alloy was organised as a multiphase system consisting of fractions of *hcp*- and *ccp*-like environments with non-homogeneous distribution of Zn. The fraction of structural types and Zn content varied differently with the change in pulse times depending on the concentration of Zn^{2+} in the electrolyte. The *hcp*-like structure dominates in most samples and can be as high as 90%. The correlation of the catalytic activity between structure and proton reduction for the NiZn alloy was not unambiguous, but whatever reason, the reaction rate was clearly enhanced compared to solid Ni.

The catalytic activity towards oxygen reduction in alkaline environment was studied on pulse plated Ni and NiZn. Alloying Ni with Zn clearly favoured the reaction path towards H_2O_2 and also lowered the overpotential for the reaction, even though the limiting currents indicated recessed electrode behaviour.

Direct electrochemical oxidation of propen and propenol on the pulse plated Ni and NiZn electrode was investigated in alkaline solution by CV and DEMS. Direct oxidation of propen has been reported in the literature but could not be repeated within the experimental frame used in this work. However, the oxidation of $Ni(OH)_2$, water and propenol showed interesting and complex CV response in the same potential region. The three oxidation reactions were separated in a CV analysis and could be correlated to the product response from the DEMS measurements. It was shown that the water oxidation starts when half of the $Ni(OH)_2$ sites were oxidised to NiOOH which indicates a bi-nuclear water oxidation mechanism. The O_2 evolution was shown to be suppressed by the addition of propenol and the only product detected by DEMS was propenal. A $Ni(OH)_2$/NiOOH mediated reaction mechanism was proposed in analogy with previous studies for other alcohols and amines.

In all the catalytic investigations in this thesis it is the nickel oxy/hydroxide redox couple that is considered to be the active part. To investigate the importance of the underlying Ni metal NiO was synthesised, mixed with carbon paste (CP) and made into a rotating electrode. $Ni_{0.75}Co_{0.25}O$ and CoO were also synthesised for comparison with NiO in the reactivity towards the ORR. 67 wt% NiO in CP increased the rate constant by 25 times compared to pure CP and showed the highest overall efficiency for ORR, for which the reduction to H_2O_2 prevails.

7.2 Future perspectives

This thesis treats the galvanic pulse plating of a novel Ni-rich NiZn alloy with fractional *hcp*/*ccp*-like structure, metal oxide-carbon paste electrodes and the catalytic activity of three important reactions on these electrodes. The width of this thesis and limited number of publications on some of these topics opens for many further questions.

The most obvious task may be to continue to investigate the NiZn alloys with the use of XAFS and try to elucidate what determines the structure composition and if it can be controlled by the plating parameters. Can the catalytic activity of Ni be increased by the induced strain from an *hcp*-like structure and what is the real role of Zn? Further investigation of this matter should be extended by theoretical calculations of different reactions on these strained structures.

The NiZn electrode behaves like a normal electrode in the PRR at pH 2.8 but as a recessed electrode for the ORR at pH 13. This is bound to depend on the hydroxide layer and it was shown that there is a difference between the $NiO/Ni(OH)_2$ layer on pulse plated Ni and NiZn. A detailed description of the oxidised layers of the electrodes at the different conditions would be helpful for understanding the formation of oxide with Zn in the Ni matrix.

There is very little done on electroactive carbon paste electrodes for the purpose of electrocatalytic properties of materials that are otherwise difficult to investigate e.g. poorly conductive, hard and brittle oxides. This investigation shows that the CP electrodes offers a window for these materials and can also be a complement to the use of Nafion emulsions films for similar purpose. For the topic of this thesis pure NiZn oxides would be interesting to examine to see if a correlation to the pulse plated NiZn alloys on e.g. the ORR could be made.

7 Acknowledgments

This work has been performed at Gothenburg University in collaboration with J. Heyrovsky Institute of Physical Chemistry in Czech Republic. The collaboration was supported by the European Union "Clean Technologies for Peroxide Generation" (CLETEPEG, Contract No. G5RD-CT-2001-00463) and "Nanostructures for Energy and Chemicals Production" (NENA, Contract No. NMP3-CT-2004-505906) projects.

Personally I would like to thank Jakub Jirkovský and Petr Krtil at the Heyrovsky Institute for their hospitality during my working visit to the institute in Prague and for being patient during this long drawn-out joint publication.

Thanks to all my co-workers throughout the years for making this workplace alive, with all the giving discussions concerning small and big things in the world, and for keeping the lab nice and clean…well at least some of you (and we all have different qualities).

Peter Reindl, thanks for being there even if I'm not and thanks for the help with the images.

I especially want to thank Zareen Abbas for endless moral support and all the interesting discussions, concerning science as well as all the problems in the world, and at home.

I also want to thank my supervisor Elisabet Ahlberg for supporting me when things has been though, and for providing an endless source of knowledge that you have patiently shared throughout the years.

Most important of all, Jessica, there is no way I could have made this without your support, you have had to put up with a very non-present man during the formation of this thesis. To my lovely daughters Rebecca and Alma, -Yes! I'm now going to try to be less boring and do more things with you, -Promise!

8 References

[1] S. Trasatti, J. Electroanal. Chem. 39 (1972)

[2] F. Calle-Vallejo, M. T. M. Koper A. S. Bandarenka, Chem. Soc. Rev. 42 (2013) 5210.

[3] F. Alcaide, P.-L. Cabot E. Brillas, J. Power Sources 153 (2006) 47.

[4] N. N. Greenwood A. Ernshaw in *Chemistry of the Elements*, Elsevier Ltd., Oxford, UK, **1997**, 1305.

[5] in *The nickel institute*, http://www.nickelinstitute.org/, **2013**.

[6] L. M. Madeira, M. F. Portela C. Mazzocchia, Catalysis reviews 46(1) (2004) 53.

[7] W. J. J. Neill, Materials Performance 40(5) (2001) 50.

[8] J. H. Larsen I. Chorkendorff, Surface Science Reports 35 (1999) 163.

[9] K. Ahmed K. Föger, Ind. Eng. Chem. Res. 49 (2010) 7239.

[10] W. Wang, C. Su, Y. Wu, R. Ran Z. Shao, Chem. Rev. (2013)

[11] W. G. Bessler, M. Vogler, H. Störmer, D. Gerthsen, A. Utz, A. Weber E. Ivers-Tiffée, Phys. Chem. Chem. Phys. 12 (2010) 13888.

[12] E. A. Gibson, M. Awais, D. Dini, D. P. Dowling, M. T. Pryce, J. G. Vos, G. Boschloof A. Hagfeldt, Phys. Chem. Chem. Phys. 15 (2013) 2411.

[13] P. Vanýsek in *CRC Handbook of Chemistry and Physics*, (Ed. T. J. Bruno), **2013**.

[14] A. Bard, R. Parsons J. Jordan in *Standard Potentials in Aqueous Solution*, International Union of Pure and Applied Chemistry, New York, **1985**.

[15] H. Bode, K. Dehmelt J. Witte, Electrochim. Acta 11 (1966) 1079.

[16] P. Oliva, J. Leonardi, J. F. Laurent, C. Delmas, J. J. Braconnier, M. Figlarz, F. Fievet A. de Guibert, J. Power Sources 8 (1982) 229

[17] W. Visscher E. Barendrecht, J. Electroanal. Chem. 154 (1983) 69.

[18] N. Sac-Epée, M. R. Palacín, B. Beaudoin, A. Delahaye-Vidal, T. Jamin, Y. Chabre J.-M. Tarascon, J. Electrochem. Soc. 144(11) (1997) 3896.

[19] N. Sac-Epée, M. R. Palacìn, A. Delahaye-Vidal, Y. Chabre J.-M. Tarâscon, J. Electrochem. Soc. 145(5) (1998) 1434.

[20] D. J. Singh, J. Electrochem. Soc. 145(1) (1998) 116.

[21] D. K. Bediako, B. Lassalle-Kaiser, Y. Surendranath, J. Yano, V. K. Yachandra D. G. Nocera, J. Am. Chem. Soc. 134 (2012) 6801−6809.

[22] M. E. G. Lyons M. P. Brandon, Int. J. Electrochem. Sci. 3 (2008) 1386

[23] W. E. O'Grady, K. I. Pandya, K. E. Swider D. A. Corrigan, J. Electrochem. Soc. 143(5) (1996) 1613.

[24] D. M. MacArthur, J. Electrochem. Soc. 117 (1970) 422.

[25] D. S. Hall, C. Bock B. R. MacDougall, Journal of The Electrochemical Society 160(3) (2013) F235.

[26] B. MacDougall M. Cohen, J. Electrochem. Soc. :Electrochemical Science and Technology 121(9) (1974) 1152.

[27] S. L. Medway, C. A. Lucas, A. Kowal, R. J. Nichols D. Johnson, J. Electroanal. Chem. 587 (2006) 172.

[28] C. A. Melendres M. Pankuch, J. Electroanal. Chem. 333 (1992) 103.

[29] F. Hahn, B. Beden, M. J. Croissant C. Lamy, Elcarochimica Acta 31(3) (1986) 335.

[30] M. Dmochowska A. Czerwinski, J. Solid State Electrochem. 2 (1998) 16.

[31] J.-J. Duprat M. Kelly in *Dedicated Processes for Electroplating on Fasteners*, Conventia, **2009**.

[32] H. Okamoto, Journal of Phase Equilibria 24(3) (2003) 280.

[33] X. Su, N.-Y. Tang J. M. Toguri, Journal of Phase Equilibria 23(2) (2002) 140.

[34] W. Xiong, H. Xu Y. Du, Computer Coupling of Phase Diagrams and Thermochemistry 35 (2011) 276.

[35] M. Chatenet, R. Faure Y. Soldo-Olivier, Journal of Electroanalytical Chemistry 580 (2005)

[36] K. Franaszczuk J. Sobkowski, Surface Science 204 (1988) 530.

[37] A. A. El-Shafei, Journal of Electroanalytical Chemistry 447 (1998) 81.

[38] E. Guerra, G. H. Kelsall, M. Bestetti, D. Dreisinger, b. K. Wong, K. A. R. Mitchell D. Bizzotto, Journal of The Electrochemical Society 151(1) (2004) E1.
[39] A. Aramata, M. A. Quaiyyum, W. A. Balais, T. Atoguchi M. Enyo, J. Electroanal. Chem. 338 (1992) 367.
[40] M. J. Nicol H. I. Philip, J. Electroanal. Chem. 70 (1976) 233.
[41] S. Swathirajan, J. Electroanal. Chem. 221 (1987) 211.
[42] G. Roventi, R. Fratesi, R. A. D. Guardia G. Barucca, J. Appl. Electrochem. 30 (2000) 173.
[43] D. M. Kolb, M. Przasnyski H. Gerischer, Electroanalytical Chemistry and Interfacial Electrochemistry 54 (1974) 25.
[44] M. A. Quaiyyum, A. Aramata, S. Moniwa, S. Taguchi M. Enyo, Journal of Electroanalytical Chemistry 373 (1994) 61.
[45] A. Brenner, *Electrodeposition of Alloys. Principles and Practice. Vol. II* Academic Press, New York and London, **1963**.
[46] H. A. Gasteiger, S. S. Kocha, B. Sompalli F. T. Wagner, Applied Catalysis B: Environmental 56 (2005) 9.
[47] F. Cheng J. Chen, Chem. Soc. Rev. 41 (2012) 2172.
[48] N. A. Anastasijević, V. Vesović R. R. Adžić, J. Electroanal. Chem. 229 (1987) 305.
[49] H. S. Wroblowa, Yen-Chi-Pan G. Razumney, J.Electroanal. Chem. 69 (1976) 195.
[50] S. Štrbac R. R. Adžic, Electrochimica Acta. 41(18) (1996) 2903.
[51] R. Cao, J.-S. Lee, M. Liu J. Cho, Adv. Energy Mater 2 (2012) 816.
[52] A. S. Aricò, S. Siracusano, N. Briguglio, V. Baglio, A. D. Blasi V. Antonucci, J. Appl. Electrochem. 43 (2013) 107.
[53] Y. Liang, Y. Li, H. Wang H. Dai, J. Am. Chem. Soc. 135 (2013) 2013−2036.
[54] M. T. Winkler, C. R. Cox, D. G. Nocera T. Buonassisi, Proc. Natl. Acad. Sci. USA 110(12) (2013) E1076.
[55] D. K. Bediako, Y. Surendranath D. G. Nocera, J. Am. Chem. Soc. 135(9) (2013) 3662−3674.
[56] M. T. M. Koper E. Bouwman, Angew. Chem. Int. Ed. 49 (2010) 3723
[57] Y. Horiuchi, T. Toyao, M. Takeuchi, M. Matsuoka M. Anpo, Phys.Chem. Chem. Phys.
, 15 (2013) 13243.
[58] H. Dagdougui, A. Ouammia R. Sacile, International Journal of hydrogen energy 36 (2011) 14324.
[59] P. Ahmadi, I. Dincer M. A. Rosen, International Journal of Hydrogen Energy 38(1795-1805) (3013) 1795.
[60] M. Fleischmann, K. Korinek D. Pletcher, J. Electroanal. Chem. 31 (1971) 39.
[61] M. Fleischmann, K. Korinek D. Pletcher, J. Chem. Soc. Perkin II 2 (1972) 1396.
[62] G. Vértes G. Horányi, Electroanal. Chem. and Interf. Electrochem. 52 (1974) 47.
[63] P. M. Robertson, J. Electroanal. Chem. 111 (1980) 97.
[64] A. Kowal, S. N. Port R. J. Nichols, Catal. Today 38 (1997) 483.
[65] Q. Yi, J. Zhang, W. Huang X. Liu, Catal. Commun. 8 (2007) 1017.
[66] A. S. Vaze, S. B. Sawant V. G. Pangarkar, J. Appl. Electrochem. 27 (1997) 584.
[67] S. Berchmans, H. Gomathi G. P. Rao, J. Electroanal. Chem. 394 (1995) 267.
[68] M. A. Abdel Rahim, R. M. Abdel Hameed M. W. Khalil, J. Power Sources 134 (2004) 160.
[69] A. A. El-Shafei, J. Electroanal. Chem. 471 (1999) 89.
[70] J. Taraszewska G. Roslonek, J. Electroanal. Chem. 364 (1994) 209.
[71] S. Maximwitch G. Bronoel, Electrochim. Acta 26 (1981) 1331.
[72] J.-W. Kim S.-M. Park, J. Electrochem. Soc. 150(11) (2003) E560.
[73] C. Samanta, Applied Catalysis A: General 350 (2008) 133.
[74] J. Rämö in *Hydrogen peroxide- metals- chelating agents; interactions and analytical techniques*, Department of Process and Environmental Engineering, University of Oulu, Oulu, **2003**.

[75] S.-i. Yamazaki, Z. Siroma, H. Senoh, T. Ioroi, N. Fujiwara K. Yasuda, Journal of Power Sources 178 (2008) 20.
[76] S. Fukuzumi, Y. Yamada K. D. Karlin, Electrochimica Acta 82 (2012) 493.
[77] in *Hydrogen peroxide*, (Ed. U. o. Y. Department of Chemistry, UK), http://www.essentialchemicalindustry.org/chemicals/hydrogen-peroxide.html, **2013**.
[78] in *Global Hydrogen Peroxide Market to Reach 4.67 Million Metric Tons by 2017, According to New Report by Global Industry Analysts, Inc*, www.PRWEB.com, San Jose, CA, **2012**.
[79] in *Solvay commissions the largest hydrogen peroxide plant in the world in Thailand* (Ed. Solvay), http://www.solvay.com/EN/NewsPress/20111005_hydrogenperoxideplant.aspx, **2011**.
[80] J. K. Edwards, S. F. Parker, J. Pritchard, M. Piccinini, S. J. Freakley, Q. He, A. F. Carley, C. J. Kiely G. J. Hutchings, Catal. Sci. Technol. 3 (2013) 812.
[81] G. J. Hutchings C. J. Kiely, Accounts of chemical research (2013) A.
[82] E. Kolehmainen I. Turunen, Russian Journal of General Chemistry 82(12) (2012) 2100.
[83] B. Šljukić, C. E. Banks, S. Mentus R. G. Compton, Phys. Chem. Chem. Phys. 6 (2004) 992.
[84] B. Šljukić, C. E. Banks R. G. Compton, Journal of the Iranian Chemical Society 2(1) (2005) 1.
[85] E. Lobyntseva, T. Kallio, N. Alexeyeva, K. Tammeveski K. o. Kontturi, Electrochimica Acta 52 (2007) 7262.
[86] T.-P. Fellinger, F. d. r. Hasché, P. Strasser M. Antonietti, J. Am. Chem. Soc. 134 (2012) 4072–4075.
[87] J. S. Jirkovský, I. Panas, E. Ahlberg, M. Halasa, S. Romani D. J. Schiffrin, J. Am. Chem. Soc. 133 (2011) 19432.
[88] M. Campos, W. Siriwatcharapiboon, R. J. Potter S. L. Horswell, Catalysis Today 202 (2013) 135.
[89] M. Shamsipur, M. Najafi, M.-R. M. Hosseini H. Sharghic, Electroanalysis 19(16) (2007) 1661.
[90] K. Otsuka I. Yamanaka, Electrochimica Acta 35(2) (1990) 319.
[91] J. A. Bard L. R. Faulkner, *Electrocemical Methods, second edition*, John Wiley & sons, New York, **2001**.
[92] T. J. Kemp in *Instrumental Methods in Elechtrochemistry*, Ellis Horwood Limited, Southampton, **1985**.
[93] J. O. M. Bockris, A. K. N. Reddy M. Gamboa-Aldeco in *Modern Electrochemistry, 2A* Kluwer Academic/Plenum Publishers, New York, **2000**.
[94] U. A. Paulus, T. J. Schmidt, H. A. Gasteiger R. J. Behm, J. Electroanal. Chem. 495 (2001) 134.
[95] A. J. Avila M. J. Brown in *Design factors in pulse plating*, American Electroplaters' Society Inc., Montreal, Canada, **1970**.
[96] D. Landolt A. Marlot, Surface and Coatings Technology 169 -170 (2003) 8.
[97] M. S. Chandrasekar M. Pushpavanam, Electrochimica Acta 53 (2008) 3313.
[98] T. R. R. W. L. Miller, J. Phys. Chem. 14 (1909) 816.
[99] H. Y. Cheh, J. Electrochem. Soc. 118(4) (1971) 551.
[100] K. Viswanathan, M. A. F. Epstein H. Y. Cheh, J. Electrochem. Soc. 125(11) (1976) 1772.
[101] N. Ibl, Surface Technology 10 (1980) 81.
[102] M. Datta D. Landolt, Surface Technology 25 (1985) 97.
[103] A. Marlot, P. Kern D. Landolt, Electrochimica Acta 48 (2002) 29.
[104] J. C. Puippe N. Ibl, AES Pulse Plating Symposium 53 (1981)
[105] H. Baltruschat, J. Am. Soc. Mass Spectrom. 15 (2004) 1693.
[106] H. Wang H. D. Abruña in *Electrocatalysis of Direct Alcohol Fuel Cells: Quantitative DEMS Studies*, Eds.: A. BocarslyD. M. P. Mingos), Springer, Heidelberg Dordrecht London New York, **2011**, 32.
[107] G. Binning, C. F. Quate C. Gerber, Physical review letters 56(9) (1986) 931.
[108] P. Eaton P. West, *Atomic Force Microscopy*, Oxford University Press, New York, **2011**.
[109] K. Shimizu T. Mitani in *New Horizons of Applied Scanning Electron Microscopy*, Eds.: G. Ertl, H. LüthD. L. Mills), Springer, Heidelberg

Dordrecht
London
New York, **2010**.
[110] G. I. Goldstein, D. E. Newbury, P. Echlin, D. C. Joy, C. Fiori E. Lifshin, *Scanning electron microscopy and x-ray microanalysis*, Springer Science + Business Media New York, **2003**.
[111] H. R. Verma, *Atomic and Nuclear Analytical Methods, XRF, Mössbauer, XPS, NAA and B63Ion-Beam Spectroscopic Techniques*, Springer Berlin Heidelberg, **2007**.
[112] M. Newville in *Fundamentals of XAFS*, Consortium for Advanced Radiation Sources University of Chicago, Chicago, **2004**.
[113] B. Lengeler in *Extended x-ray absorption fine structure*, (Ed. F. Hippert), Springer, **2006**, 131.
[114] M. Neville, J. Synchrotron Rad. 8 (2001) 322.
[115] H. Abe in *A Brief Introduction to XAFS*, Jordan, **2011**.
[116] D. Lützenkirchen-Hecht H.-H. Strehblow in *Synchrotron Methods for Corrosion Research*, Eds.: P. MarcusF. B. Mansfeld), CRC press, Boca Raton, **2006**.
[117] I. Ahmed in *Pulse plating of nanocrystalline Nickel, Zinc and Ni-Zn multi-layers on steel substrate*, *Master* Swedish Institute for Metals Research, Stockholm, **2002**, 67.
[118] A. M. Alfantazi, G. Brehaut U. Erb, Surface and Coatings Thechnology 89 (1997) 239.
[119] G. Jerkiewicz, G. Vatankhah, J. Lessard, M. P. Soriaga Y.-S. Park, Electrochim. Acta 49 (2004) 1451.
[120] M. F. Mathias T. W. Chapman, J. Electrochem. Soc. 137(1) (1990) 102.
[121] M. F. Mathias T. W. Chapman, J. Electrochem. Soc.: Electrochem. Sci. Tech. 134(6) (1987) 1408.
[122] D. Kashchiev, Thin Solid Films 29 (1975) 193.
[123] V. A. Isaev O. V. Grishenkova, J. Solid State Electrochem. 17 (2013) 1505.
[124] V. A. Isaev, O. V. Grishenkova O. L. Semerikova, J Solid State Electrochem 17 (2013) 361.
[125] T. Montiel, O. Solorza H. Sanchez, J. Electrochem. Soc. 147 (2000) 1031.
[126] Y.-P. Lin J. R. Selman, J. EIoctrochem. Soc. 140(5) (1993) 1304.
[127] I. K. Marshakov, E. E. Zotova I. V. Protasova, Protection of Metals 40(3) (2004) 220.
[128] F. Vicente, J. Gregori, J. J. García-Jareño D. Giménez-Romero, J. Solid State Electrochem. 9 (2005) 684.
[129] S. S. A. E. Rehim, S. M. A. E. Wahaaband E. A. A. E. Meguid, Surface and Coatings Technology 29 (1986) 325.
[130] T. C. Tan D.-T. Chin, j. Appl. Electrochem. 18 (1988) 831.
[131] A. Petrauskas, L. Grincevičienė, A. Češūnienė R. Juškėnas, Electrochimica Acta 50 (2005) 1189.
[132] J. Scherer, B. M. Ocko O. M. Magnussen, Electrochimica Acta 48 (2003) 1169.
[133] N. Sato G. Okamoto, J. Electrochem. Soc. 110(6) (1963) 605.
[134] N. Sato G. Okamoto, J. Electrochem. Soc. 111(8) (1964) 897.
[135] I. Olefjord L. Wegrelius, Corros. Sci 31 (1990) 89.
[136] L. Zhang D. D. Macdonald, Electrochimica Acta 43(18) (1998) 2661.
[137] M. Lakatos-Varsányi, F. Falkenberg I. Olefjord, Electrochimia Acta. 43(1-2) (1998) 187.
[138] R. Rofagha, S. J. Splinter, U. Erb N. S. Mclntyre, NanoStructured Materials 4(1) (1994) 69.
[139] L. Yang, J. EIoctrochem. Soc. 97(8) (1950) 241.
[140] R. M. A. Tehrani S. A. Ghani, Fuel Cells 9(5) (2009) 579.
[141] M. Ohtake, T. Tanaka, F. Kirino M. Futamoto, Journal of Physics: Conference Series 200 (2010) 072072 (2010)
[142] A. Lahiri, R. Das R. G. Reddy, Journal of Power Sources 195 (2010) 1688.
[143] A. Lahiri Z. Tadisina, Materials Chemistry and Physics 124 (2010) 41.
[144] Y. Mia, D. Yuana, Y. Liua, J. Zhanga Y. Xiaoa, Materials Chemistry and Physics 89 (2005) 359.
[145] A. K. N. Reddy, Acta Cryst. 17 (1964)
[146] M. K. Datta, S. K. Pabi B. S. Murty, J. Mater. Res. 15(7) (2000) 1429.

[147] E. Ahlberg, F. Falkenberg, A. J. Manzanares D. J. Schiffrin, J. Electroanal. Chem. 548 (2003) 85.
[148] L. L. Holebrook H. Wise, J. Catal. 38 (1975) 294.
[149] T.-C. Chou J.-C. Chang, Chem. Eng. Sci. 35 (1980) 1581.
[150] C. F. Oduoza K. Scott, Inst. Chem. Eng. Symp. Series 127 (1992) 37.
[151] K. Otsuka I. Yamanaka, Catal. Today 41 (1998) 311.
[152] Y. P. Sun, O. Qiu, W. L. Xu K. Scott, J. Electroanal. Chem. 503 (2001) 36.
[153] A. Zimmer, D. Mönter W. Reschetilowski, J. App. Electrochem. 33 (2003) 933.
[154] I. Duo, P.-A. Michaud, W. Haenni, A. Perret C. Comninellisa, Electrochem. and Solid-State Lett. 3(7) (2000) 325.
[155] O. Simond, V. Schaller C. Comninellis, Electrochimica Acta 42(13-14) (1997) 2009.
[156] R. Holze, T. Luczak M. Beltowska-Brzezinska, Elearochim. Acta 39(7) (1994) 991.
[157] J. Y. Gui, B. E. Kahn, C.-H. Lin, F. Lu, G. N. Salaita, D. A. Stem, D. C. Zapien A. T. Hubbard, J. Electroanal. Chem. 252(1) (1988) 169.
[158] G. Göransson, A. Johansson E. Ahlberg, Unpublished results
[159] M. Busch, E. Ahlberg I. Panas, PCCP 13 (2011) 15062.
[160] M. Busch, E. Ahlberg I. Panas, PCCP 13 (2011) 15069.
[161] E. Pastor, S. Wasmus T. Iwasita, J. Electroanal. Chem. 353 (1993) 81.
[162] M. C. Arévalo, J. L. Rodríguez E. Pastor, J. Electroanal. Chem. 505(1-2) (2001) 62.
[163] E. Pastor, V. M. Schmidt, T. Iwasita, M. C. Arévalo, S. González A. J. Arvia, Electrochim. Acta 38(10) (1993) 1337.
[164] V. S. Bagotzky, N. A. Shumilova E. I. Khrushceva, Electrochimica Acta 21 (1976) 919.
[165] C.-C. Chang T.-C. Wen, Materials Chemistry and Physics 47 (1997) 203.
[166] A. C. C. Tseung B. S. Hobbs, Electrochimica Acta 17 (1972) 1557.
[167] A. C. C. Tseung, B. S. Hobbs A. D. S. Tantram, Electrochimica Acta 15 (1970) 473.
[168] H. Yoneyama, T. Fujimoto H. Tamura, Electroanalytical Chemistry and lnterfacial Electrochemistry 58 (1975) 422.
[169] R. N. Adams, Anal. Chem. 30 (1958) 1576.
[170] N. Alonso-Vante, H. Tributsch O. Solorza-Feria, Electrochimica Acta 4 0(5) (1995) 567.
[171] M.Březina A.Hofmanová-Matějková, Collection Czechoslov. Chem. Commun. 38 (1973) 3024.
[172] E. Ahlberg, U. Palmqvist, N. Simic R. Sjövall, Journal of Power Sources 85 (2000) 245.
[173] M. E. Rice, Z. Galus R. N. Adams, J. Electroanal. Chem. 143 (1983) 89.
[174] V. S. Holgersson A. Karlson, Z. Anorg. Allg. Chem. 182 (1929) 255.
[175] K. Tammeveski, K. Kontturi, R. J. Nichols, R. J. Potter D. J. Shiffrin, J. Electroanalytical Chemistry 515 (2001) 101.
[176] R. J. Taylor A. A. Humffray, J. Electroanal. Chem. 64 (1975) 63.
[177] M. S. Hossain, D. Tryk E. Yeager, Elcarochimica Acta 34(12) (1989) 1733.
[178] J. Xu, W. Huang R. L. McCreery, J. Electroanal. Chem. 410 (1996) 235.
[179] D. R. Lawson, L. D. Whiteley, C. R. Martin, M. N. Szentimay J. I. Song, J. Electrochem. Soc. 135(9) (1988) 2247.
[180] T. J. Schmidt, H. A. Gasteiger R. J. Behm, Journal of The Electrochemical Society 146(4) (1999) 1296.
[181] D. Yohe, A. Riga, R. Greef E. Yeager, Electrochim. Acta 13 (1968) 1351.
[182] J. Scarminio, W. Estrada, A. Andersson, A. Gerenstein F. Decker, J. Electrochem. Soc. 139(5) (1992) 1236.
[183] G. Boschloo A. Hagfeldt, J. Phys. Chem. B 105 (2001) 3039.
[184] K. Juodkazis, J. Juodkazytė, R. Vilkauskaitė V. Jasulaitienė, J. Solid State Electrochem. 12 (2008) 1469.